USGS
science for a changing world

Prepared in cooperation with the Bureau of Reclamation

Modeling Hydrodynamics and Heat Transport in Upper Klamath Lake, Oregon, and Implications for Water Quality

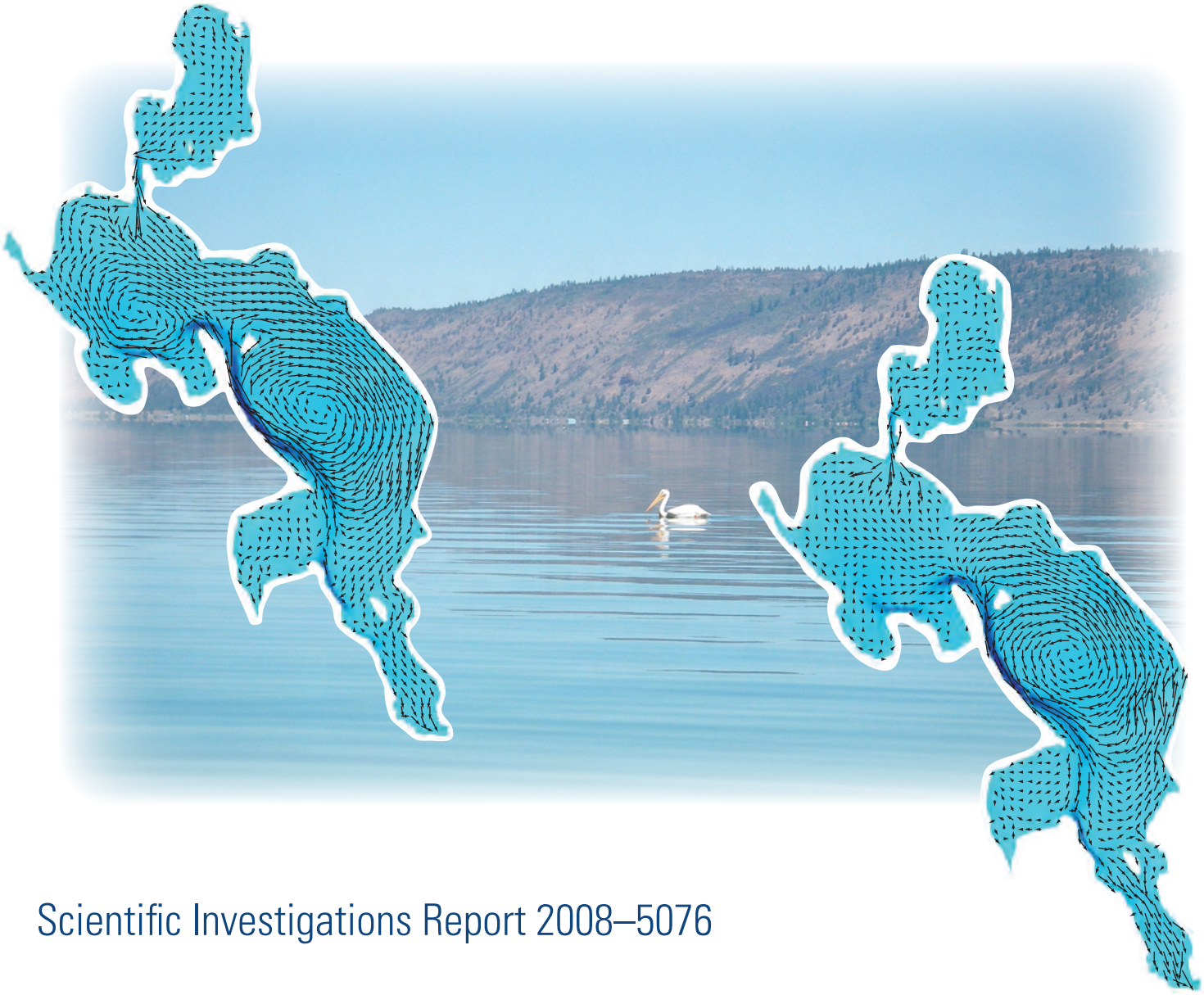

Scientific Investigations Report 2008–5076

U.S. Department of the Interior
U.S. Geological Survey

Cover: Photograph of Upper Klamath Lake, Oregon, with pelican.
(Photograph taken by Lee Simons, U.S. Geological Survey, 2007.)

Modeling Hydrodynamics and Heat Transport in Upper Klamath Lake, Oregon, and Implications for Water Quality

By Tamara M. Wood, Ralph T. Cheng, Jeffrey W. Gartner, Gene R. Hoilman, Mary K. Lindenberg, and Roy E. Wellman

Prepared in cooperation with the Bureau of Reclamation

Scientific Investigations Report 2008–5076

U.S. Department of the Interior
U.S. Geological Survey

U.S. Department of the Interior
DIRK KEMPTHORNE, Secretary

U.S. Geological Survey
Mark D. Myers, Director

U.S. Geological Survey, Reston, Virginia: 2008

For product and ordering information:
World Wide Web: http://www.usgs.gov/pubprod
Telephone: 1-888-ASK-USGS

For more information on the USGS--the Federal source for science about the Earth, its natural and living resources, natural hazards, and the environment:
World Wide Web: http://www.usgs.gov
Telephone: 1-888-ASK-USGS

Suggested citation:
Wood, T.M., Cheng, R.T., Gartner, J.W., Hoilman, G.R., Lindenberg, M.K., and Wellman, R.E., 2008, Modeling hydrodynamics and heat transport in Upper Klamath Lake, Oregon, and implications for water quality: U.S. Geological Survey Scientific Investigations Report 2008–5076, 48 p.

Contents

Figures

Figures—Continued

Tables

Conversion Factors and Datums

Conversion Factors

Multiply	By	To obtain
centimeter (cm)	0.3937	inch (in.)
cubic meter (m^3)	1.308	cubic yard (yd^3)
cubic meter per second (m^3/s)	70.07	acre-foot per day (acre-ft/d)
cubic meter per second (m^3/s)	35.31	cubic foot per second (ft^3/s)
cubic meter per second (m^3/s)	22.83	million gallons per day (Mgal/d)
gram (g)	0.03527	ounce, avoirdupois (oz)
joule (J)	0.0000002	kilowatthour (kWh)
kilogram (kg)	2.205	pound avoirdupois (lb)
kilogram per cubic meter (kg/m^3)	0.06242	pound per cubic foot (lb/ft^3)
kilometer (km)	0.6214	mile (mi)
liter (L)	1.057	quart (qt)
meter (m)	3.2808	feet (ft)
millibar (mb)	0.02953	inches of mercury at 0°C
square kilometer (km^2)	0.3861	square mile (mi^2)
square meter (m^2)	10.76	square foot (ft^2)

Temperature in degrees Celsius (°C) may be converted to degrees Fahrenheit (°F) as follows:

$$°F=(1.8\times°C)+32.$$

Temperature in degrees Fahrenheit (°F) may be converted to degrees Celsius (°C) as follows:

$$°C=(°F-32)/1.8.$$

Concentrations of chemical constituents in water are reported in milligrams per liter (mg/L).

Datums

Vertical coordinate information is referenced to the National Geodetic Vertical Datum of 1929 (NGVD 29). "Elevation," as used in this report, refers to distance above the vertical datum.

Horizontal coordinate information is referenced to the North American Datum of 1927 (NAD 27).

Modeling Hydrodynamics and Heat Transport in Upper Klamath Lake, Oregon, and Implications for Water Quality

By Tamara M. Wood, Ralph T. Cheng, Jeffrey W. Gartner, Gene R. Hoilman, Mary K. Lindenberg, and Roy E. Wellman

Abstract

The three-dimensional numerical model UnTRIM was used to model hydrodynamics and heat transport in Upper Klamath Lake, Oregon, between mid-June and mid-September in 2005 and between mid-May and mid-October in 2006. Data from as many as six meteorological stations were used to generate a spatially interpolated wind field to use as a forcing function. Solar radiation, air temperature, and relative humidity data all were available at one or more sites. In general, because the available data for all inflows and outflows did not adequately close the water budget as calculated from lake elevation and stage-capacity information, a residual inflow or outflow was used to assure closure of the water budget.

Data used for calibration in 2005 included lake elevation at 3 water-level gages around the lake, water currents at 5 Acoustic Doppler Current Profiler (ADCP) sites, and temperature at 16 water-quality monitoring locations. The calibrated model accurately simulated the fluctuations of the surface of the lake caused by daily wind patterns. The use of a spatially variable surface wind interpolated from two sites on the lake and four sites on the shoreline generally resulted in more accurate simulation of the currents than the use of a spatially invariant surface wind as observed at only one site on the lake. The simulation of currents was most accurate at the deepest site (ADCP1, where the velocities were highest) using a spatially variable surface wind; the mean error (ME) and root mean square error (RMSE) for the depth-averaged speed over a 37-day simulation from July 26 to August 31, 2005, were 0.50 centimeter per second (cm/s) and 3.08 cm/s, respectively. Simulated currents at the remaining sites were less accurate and, in general, underestimated the measured currents. The maximum errors in simulated currents were at a site near the southern end of the trench at the mouth of Howard Bay (ADCP7), where the ME and RMSE in the depth-averaged speed were 3.02 and 4.38 cm/s, respectively. The range in ME of the temperature simulations over the same period was –0.94 to 0.73 degrees Celsius (°C), and the RMSE ranged from 0.43 to 1.12°C. The model adequately simulated periods of stratification in the deep trench when complete mixing did not occur for several days at a time.

The model was validated using boundary conditions and forcing functions from 2006 without changing any calibration parameters. A spatially variable wind was used. Data for the model validation periods in 2006 included lake elevation at 4 gages around the lake, currents collected at 2 ADCP sites, and temperature collected at 21 water-quality monitoring locations. Errors generally were larger than in 2005. ME and RMSE in the simulated velocity at ADCP1 were 2.30 cm/s and 3.88 cm/s, respectively, for the same 37-day simulation over which errors were computed for 2005. The ME in temperature over the same period ranged from –0.56 to 1.5°C and the RMSE ranged from 0.41 to 1.86°C.

Numerical experiments with conservative tracers were used to demonstrate the prevailing clockwise circulation patterns in the lake, and to show the influence of water from the deep trench located along the western shoreline of the lake on fish habitat in the northern part of the lake. Because water exiting the trench is split into two pathways, the numerical experiments indicate that bottom water from the trench has a stronger influence on water quality in the northern part of the lake, and surface water from the trench has a stronger influence on the southern part of the lake. This may be part of the explanation for why episodes of low dissolved oxygen tend to be more severe in the northern than in the southern part of the lake.

Introduction

Upper Klamath Lake (UKL) is a large (surface area 232 km^2) and shallow (mean depth 2.8 m at full pool) lake located in southern Oregon, in the semiarid landscape in the rain shadow east of the Cascade Range, at a full-pool elevation of 1,262.9 m above the National Geodetic Vertical Datum of 1929 (fig. 1). Agency Lake is connected to the northern end of Upper Klamath Lake through a narrow channel (Agency Straits), and adds about 38 km^2 of surface area.

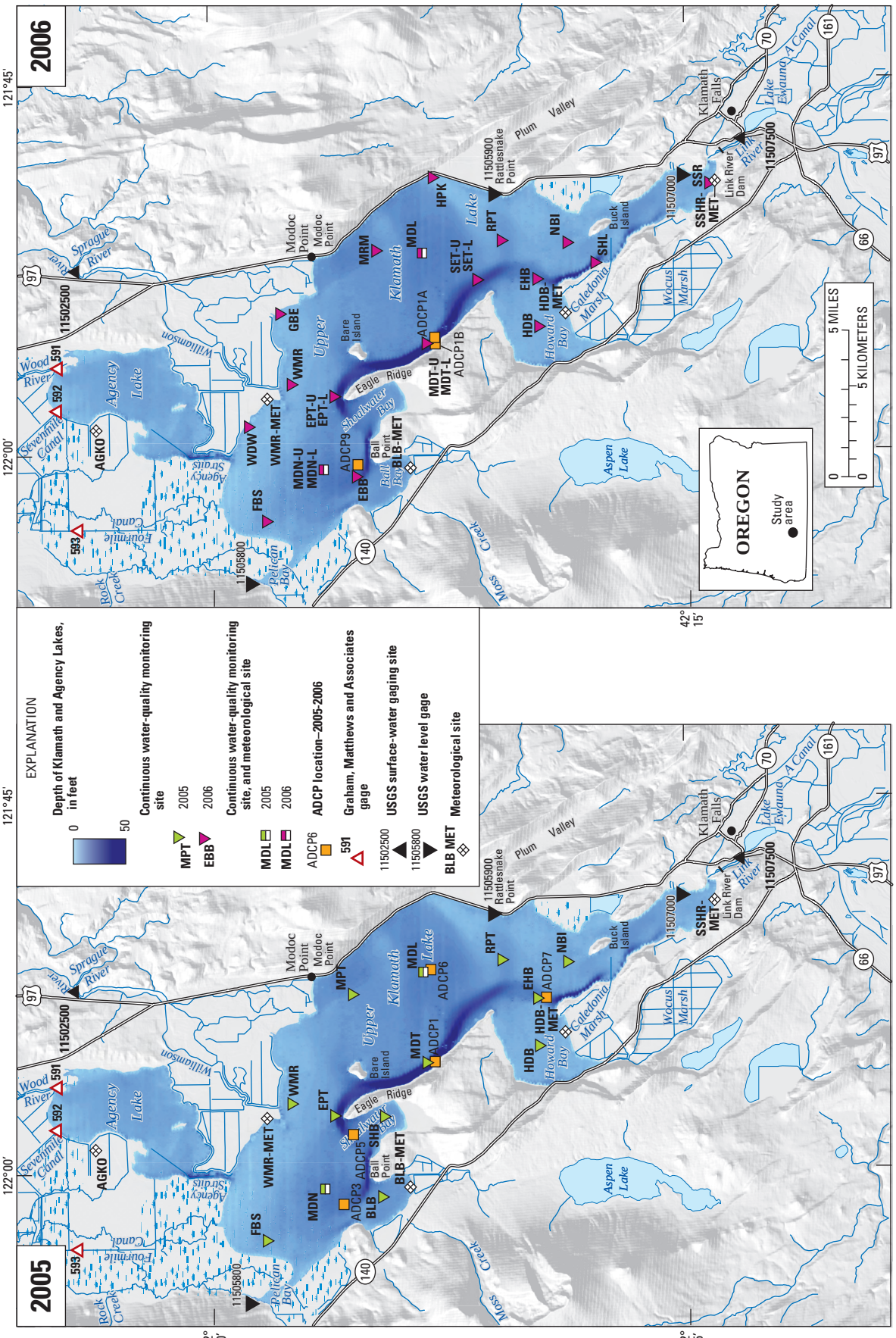

Figure 1. Location of monitoring sites in Upper Klamath Lake, Oregon.

Paleolimnological evidence indicates that the lake has been highly productive for at least the last 1,000 years (Eilers and others 2004). This can be attributed to, among other things, the fact that much of the basin drains volcanic soils with high phosphorus content, and, because most of the lake is shallow, photosynthetically active radiation penetrates most of its volume on a daily basis, providing energy that is converted to biomass through the photosynthesis performed by algae and cyanobacteria.

Starting about 150 years ago, changes in land use in the UKL basin led to increased sedimentation rates and nutrient loads, and to a decrease in the nitrogen to phosphorus ratio in the nutrient loads to the lake. Simultaneous with these changes, the diverse taxa that characterized the assemblage of phytoplankton prior to 150 years ago gradually came to be dominated by a single species of buoyant cyanobacterium, *Aphanizomenon flos aquae* (AFA) (Phinney and Peek, 1960; Miller and Tash, 1967; Kann, 1998; Eilers and others, 2004; Eilers and others, 2001; Bradbury, Colman, and Dean, 2004; Bradbury, Colman, and Reynolds, 2004; Colman and others, 2004; Colman, Bradbury, and Rosenbaum, 2004). The shallowness of the lake also makes the transfer of nutrients from the sediments to the water column and back again to the sediments particularly efficient, although the specific mechanism for the transfer is still debated (Kann, 1998; Walker, 2001; Fisher and Wood, 2004). Annual blooms of AFA are perpetuated primarily by this internal recycling of nutrients stored in the sediments, rather than by external sources (Kann and Walker, 1999; Walker, 2001; Kann, 1998).

The annual cyanobacterial blooms have important implications for water quality. Highly supersaturated dissolved oxygen concentrations with large diel swings, and high pH values caused by the photosynthetic removal of carbon dioxide from the water column, are associated with the rapidly expanding phase of the bloom. A rapid bloom decline is accompanied by undersaturated dissolved oxygen concentrations as photosynthetic production of oxygen slows dramatically and ongoing respiratory demands continue, and decay processes associated with cell senescence consume oxygen rapidly. Severe low dissolved oxygen events (LDOEs) associated with bloom declines are detrimental to the survival of the shortnose and Lost River suckers, which are listed as endangered under the Endangered Species Act by the U.S. Fish and Wildlife Service (2001). As determined from an analysis of three large fish die-offs during 1995–97 (Perkins and others, 2000), severe LDOEs in which dissolved oxygen concentrations of less than 4 mg/L occur throughout the water column for a large part of the day and persist for several days at a time may cause fish death. These conditions may also cause fish death indirectly by forcing fish into crowded conditions and facilitating the spread of disease among animals already weakened by exposure to hypoxia, high pH, and the high un-ionized ammonia concentrations that sometimes accompany conditions of high pH.

Continuous water-quality monitors with well-documented data quality were first installed by the U.S. Geological Survey (USGS) for long-term deployment in 2002. Thus, reconstructing the details of the LDOEs of 1995–97 on time scales of a few days to a week is not possible, but information gathered since 2002 indicates that there is a rapid decline in the AFA bloom in most years around the end of July or beginning of August (Wood and others, 2006; Hoilman and others, 2008). The longest dataset of water-quality measurements in UKL is a 17-year record of biweekly profiles of conventional water-quality variables, as well as depth-averaged chlorophyll *a* and nutrient concentrations (Kris Fisher, Klamath Tribes, oral commun., 2007). This dataset does not provide enough temporal resolution to determine precise dates of bloom peaks and troughs, but the general pattern appears consistent over this long record. The effect of the late July to early August decline on dissolved oxygen concentrations over a large area in the northern part of the lake, which is the preferred habitat for adult suckers, varies in severity from year to year. In 2003, for example, dissolved oxygen concentrations at a centrally located site in the northern part of the lake were less than 3 mg/L continuously for 8 days, and the spatial extent of the LDOE was nearly 40 km^2 (Wood and others, 2006). This event culminated in a smaller fish die-off than those of the mid-1990s (Adams and others, 2003). A die-off of the severity of the mid-1990s has not occurred since the water-quality monitors were installed in 2002; therefore, it is not an annual occurrence. The impact of large fish die-offs on the endangered sucker populations is, nonetheless, devastating; thus, it is important to understand what combination of conditions results in the most severe events before a management strategy can be devised to modulate the algal bloom-decline cycle. Understanding the causes of the precipitous bloom decline is critical in this regard because the loss of photosynthetic production in addition to the added oxygen demand generated by senescing cells is the root cause of LDOEs. It also has been observed that the events are more severe in the northern sucker habitat area of the lake than in areas of similar depth in the rest of the lake, and observations of currents have indicated that circulation patterns play an important role.

The surface area to volume ratio of a shallow lake contributes to greater primary production per volume and enhanced nutrient cycling between the water column and sediments in comparison to a deep lake (Scheffer, 1998). Thus, the hypereutrophication of UKL has similarities to processes observed in other shallow lakes that experience massive cyanobacterial blooms. At the same time, each lake is unique in some way, and UKL is no exception. A particularly important feature of UKL that has implications for both the hydrodynamics and water quality of the lake is its bathymetry. Although most of the lake is shallow, a relatively deep trench runs along the western shoreline (fig. 1). This trench is apparent in the bathymetry as far south as Buck Island.

It runs across the mouth of Howard Bay, along the western shoreline and to the west of Bare Island, and then turns west around Eagle Point, runs across the entrance to Shoalwater Bay and along Ball Point, before turning north at the entrance to Ball Bay and fading away. The currents in the trench are the strongest in the lake and are aligned with the bathymetry; under prevailing wind conditions, water flows northward through the trench (Gartner and others, 2007).

Recognizing that a detailed understanding of the movement of water around the lake was essential to a complete understanding of the water quality of the lake, the Bureau of Reclamation and the U.S. Geological Survey (USGS) entered into a cooperative agreement in 2005 to develop a hydrodynamic model of the lake. This report is the first comprehensive documentation of the UKL model and its application, although singular aspects of the model have appeared in proceedings papers (Cheng and others, 2005; Wood and Cheng, 2006).

Purpose and Scope

The purpose of this report is to provide a comprehensive accounting of the boundary, forcing, and calibration data available during the summer field season in 2005 (approximately mid-June through mid-September) and 2006 (approximately mid-May through mid-October), to provide a detailed description of the source and boundary terms that have been added to the model in order to accurately simulate heat transport, and to document the calibration and validation of the numerical model. The report also discusses the implications of lake circulation for water quality, with particular emphasis on how circulation might affect dissolved oxygen concentrations in the northern part of the lake. The most important numerical features of the model are briefly summarized below, but the reader is referred to the references cited in this report for the details of the numerical methods used in the computational core of the UnTRIM model.

Model Description

Governing Equations

The governing equations for three-dimensional, baroclinic circulation and the transport of scalar variables in a lake include the conservation equations of mass and momentum, a kinematic free-surface equation (derived from mass conservation), an equation of state relating density to temperature, and a conservation equation for each scalar variable. The lake is assumed to be sufficiently large for a Coriolis acceleration term to be included in the momentum equations. To simplify the governing equations, the water is assumed to be incompressible and it is assumed that the Boussinesq approximation applies. In Cartesian coordinates, the mass conservation equation is

$$\frac{\partial u}{\partial x}+u\frac{\partial v}{\partial y}+v\frac{\partial u}{\partial z}=0 \ , \tag{1}$$

where

u and v are components of velocity in the horizontal directions x and y, respectively, and

w is the component of velocity in the vertical direction, z.

After integrating over depth and applying the kinematic condition at the free surface, the mass conservation equation becomes

$$\frac{\partial \eta}{\partial t}+u\frac{\partial U}{\partial x}+v\frac{\partial V}{\partial y}=0 \ , \tag{2}$$

where

$\eta(x,y,t)$ is the free surface, and

U and V are the horizontal components of, velocity integrated over the depth of the water column from the bottom $z = -h$ to the free surface at $z = \eta$.

$$U=\int_{-h}^{\eta} u dz \text{ and } V=\int_{-h}^{\eta} v dz \ . \tag{3}$$

The momentum conservation equations in three spatial dimensions are

$$\frac{\partial u}{\partial t}+u\frac{\partial u}{\partial x}+v\frac{\partial u}{\partial y}+w\frac{\partial u}{\partial z}-fv=-\frac{1}{\rho_0}\frac{\partial p_a}{\partial x}-g\frac{\partial \eta}{\partial x} -g\frac{\partial \rho'}{\partial x}-\frac{\partial q}{\partial x}+K_h\left(\frac{\partial^2 u}{\partial x^2}+\frac{\partial^2 u}{\partial y^2}\right)+\frac{\partial}{\partial z}\left(K_z\frac{\partial u}{\partial z}\right) \ , \tag{4}$$

$$\frac{\partial v}{\partial t}+u\frac{\partial v}{\partial x}+v\frac{\partial v}{\partial y}+w\frac{\partial v}{\partial z}+fu=-\frac{1}{\rho_0}\frac{\partial p_a}{\partial y}-g\frac{\partial \eta}{\partial y} -g\frac{\partial \rho'}{\partial y}-\frac{\partial q}{\partial y}+K_h\left(\frac{\partial^2 v}{\partial x^2}+\frac{\partial^2 v}{\partial y^2}\right)+\frac{\partial}{\partial z}\left(K_z\frac{\partial v}{\partial z}\right) \ , \tag{5}$$

and

$$\frac{\partial w}{\partial t}+u\frac{\partial w}{\partial x}+v\frac{\partial w}{\partial y}+w\frac{\partial w}{\partial z}=-\frac{\partial q}{\partial z}+K_h\left(\frac{\partial^2 w}{\partial x^2}+\frac{\partial^2 w}{\partial y^2}\right) +\frac{\partial}{\partial z}\left(K_z\frac{\partial w}{\partial z}\right) \ . \tag{6}$$

The Coriolis parameter f is assumed constant over the domain. K_z and K_h and are the vertical and horizontal viscosity coefficients, respectively, ρ_0 is a constant reference density of water (1,000 kg/m^3), g is gravitational acceleration (9.81 m s^{-2}), and ρ' is the vertically integrated and normalized deviation from reference density. The above equations have been derived by decomposing the pressure P into a hydrostatic component, dependent on the free-surface elevation η and the spatially varying density ρ, and a nonhydrostatic component q as:

$$p(x,y,z,t) = p_a(x,y,t) + \rho_0\left(g\left[\eta(x,y,t)-z\right] + g\rho'(x,y,t) + q(x,y,z,t)\right), \quad (7)$$

where

$$\rho' = \int_z^{\eta} \frac{\rho-\rho_0}{\rho_0} d\zeta \quad , \quad (8)$$

where
ζ is the variable of integration, and
p_a is atmospheric pressure.

The equation for conservative transport of a scalar variable (including heat and solute) with concentration C is:

$$\frac{\partial C}{\partial t} + \frac{\partial (uC)}{\partial x} + \frac{\partial (vC)}{\partial y} + \frac{\partial\left[(w-w_s)C\right]}{\partial z} = \frac{\partial}{\partial x}\left(D_h \frac{\partial C}{\partial x}\right) + \frac{\partial}{\partial y}\left(D_h \frac{\partial C}{\partial y}\right) + \frac{\partial}{\partial z}\left(D_z \frac{\partial C}{\partial z}\right) \quad , \quad (9)$$

where
w_s is a settling velocity for the scalar, and
D_z and D_h are the vertical and horizontal diffusivity coefficients, respectfully.

The final equation is the equation of state, which in the general case relates density to temperature and salinity. In this freshwater application the equation of state is an empirical relation that relates density in kg m^{-3} only to water temperature T_w in °C (Gill, 1982):

$$\rho = 999.842594 + 6.793952\times10^{-2}T_w - 9.095290\times10^{-3}T_w^2 + 1.001685\times10^{-4}T_w^3 - 1.120083\times10^{-6}T_w^4 + 6.536332\times10^{-9}T_w^5 \quad . \quad (10)$$

Equations (2) through (10) are the governing equations solved within the computational core of the UnTRIM model. If the water density can be approximated as constant (barotropic flows), the scalar transport equation (9) is uncoupled from the momentum equations (4), (5), and (6). When the hydrostatic approximation is made, the horizontal gradients of q drop out of equations (4) and (5), and equation (6) is replaced by the hydrostatic approximation.

The governing system of equations can be solved efficiently by a semi-implicit finite-difference method that is computationally fast, accurate, and stable over a regular computational mesh as discussed by Casulli and Cheng (1992) and Casulli and Cattani (1994). A weak Courant-Friedrich-Lewy (CFL) stability condition is imposed on the computational time step due to the explicit treatment of the horizontal diffusion in the momentum equations. If density stratification in the lake is considered, the transport equations are coupled with the momentum equations through the density gradient terms. In this case, the density gradients in the momentum equations and the mass conservation of the scalar variables (including heat and solute) are solved explicitly. The resulting numerical scheme is subject to an additional weak CFL stability condition on the computational time step due to the explicit treatment of the transport equation and the baroclinic pressure terms in the momentum equations.

Orthogonal Unstructured Grids

The governing equations are solved in physical space without invoking any coordinate transformation in the horizontal or vertical directions. The stability properties of the governing partial differential equations are controlled by using a semi-implicit finite-difference scheme (Casulli, 1990; Casulli and Cheng, 1992); the resulting numerical algorithm is robust and computationally efficient. Traditional finite-difference schemes resort to refining the rectangular finite-difference mesh when a complicated domain is encountered in order to resolve the flow distributions in narrow and confined regions. The resulting fine-resolution grids in broad and open regions are unnecessary, and the computational mesh consumes a large portion of computing resources, which is not computationally efficient. In the UnTRIM model, the semi-implicit finite-difference method is applied over an unstructured grid (Casulli and Zanolli, 1998; Casulli and Walters 2000) in which fine grid resolutions are used in complex regions, and relatively coarse grids are used in broad and open areas.

When a computational mesh is created, the horizontal domain is covered by a set of nonoverlapping convex polygons. Each side of a polygon is either a boundary line or a side of an adjacent polygon. The center of each polygon is defined such that the segment joining the centers of two adjacent polygons intersects the side shared by the two polygons and is orthogonal to it (fig. 2). The center of a

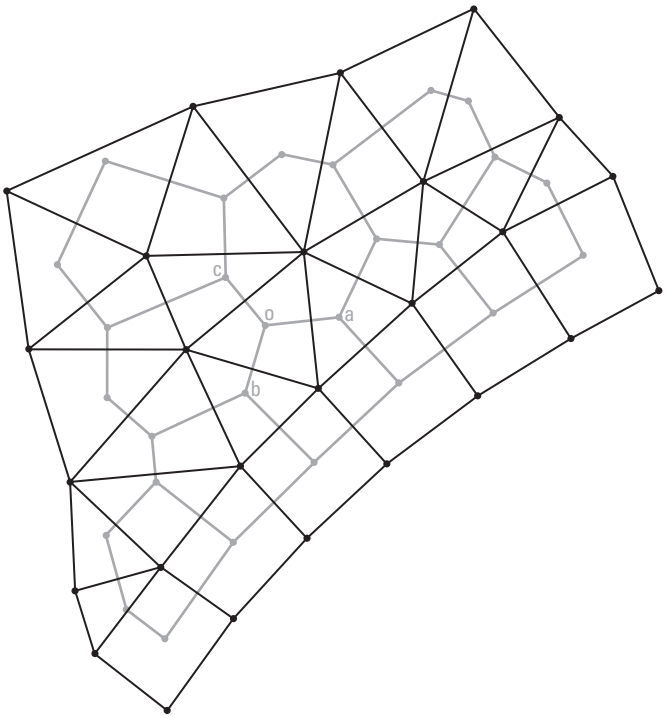

Figure 2. An example of an unstructured orthogonal grid.

polygon does not necessarily coincide with its geometrical center, except in special cases such as rectangular finite-difference grids and grids of uniform equilateral triangles. This type of computational mesh is called an unstructured orthogonal grid (Casulli and Zanolli, 1998; Casulli and Walters, 2000). In an unstructured grid representation within the UnTRIM model, each polygon has either three or four sides. Each polygon, side, and vertex in the grid is assigned a unique number. The x–y coordinates of the vertices of each polygon must be specified, as well as the information that relates each polygon to its vertices and sides.

In the vertical direction, the water body to be modeled is divided into layers by horizontal planes. The polygons between the horizontal planes become a stack of prisms whose thickness is the prescribed layer thickness. The water-surface elevation is assumed to be uniform within each polygon and is defined at the center of the polygon. The velocity component normal to each face of a prism is assumed to be uniform over the face. The velocity is defined at each vertex in the middle of each layer, and the spatial distribution of velocity through the prism is obtained by interpolating between the velocities at the vertices. Finally, the water depth below each polygon is specified and assumed uniform on each side.

The unstructured orthogonal grid for UKL (fig. 3) was created and optimized with the JANET software (Lippert and Sellerhoff, 2006). This software enables semiautomated creation of an initial grid, followed by manual fine-tuning of individual polygons that are identified by tests within the software to be outside of a prescribed tolerance for orthogonality. The resulting grid for UKL has 8,389 polygons, 4,555 vertices, and 28 layers of 0.5 m thickness. Because most of the lake is shallow, however, the number of active prisms in each layer varies from more than 8,000 in each of the top 3 layers to less than 100 in each of the 11 deepest layers of the grid. The length of the sides of the polygons varies from approximately 100 m in areas along the trench where the bathymetry changes rapidly to approximately 400 m in the open areas of the lake.

Numerical Approximation

A semi-implicit finite-difference scheme is used to obtain an efficient numerical algorithm for which stability is independent of free-surface gravity waves, wind stress, vertical viscosity and bottom friction, for both the hydrostatic (Casulli and Walters, 2000; Casulli, 1990) and nonhydrostatic case (Casulli and Zanolli, 2002; Casulli, 1999a, Casulli, 1999b). The momentum equations (4)–(6) are finite-differenced in the direction normal to each vertical face of each computational prism (along *oa*, *ob*, and *oc* in fig. 2). The momentum equations relate the gradient of water-surface elevation between adjoining prisms to the face velocity on the common face between these prisms. The vertical mixing and the bottom friction are discretized implicitly in time for numerical stability, whereas an explicit finite-difference operator is used to solve the wind stress and the advection and horizontal dispersion terms. This operator can take several particular forms; an Eulerian–Lagrangian scheme is used in UnTRIM (Casulli and Cheng, 1992). For stability, the implicitness factor θ must be in the range $1/2 \leq \theta \leq 1$ (Casulli and Cattani, 1994). In the vertical direction, a simple finite-difference discretization that does not require uniform layers is adopted. The vertical thickness of the top and bottom layers can vary spatially and the thickness of the top layer also can vary with time. The vertical thickness of the top layer is allowed to become zero, in order to accommodate the drying of cells.

The free-surface equation (2) is discretized semi-implicitly (Casulli and Cattani, 1994; Casulli and Walters, 2000), and only the face velocities are needed to complete the finite volume balance of total volume below each polygon. The surface elevation at the center of each polygon is determined by substituting the finite-differenced momentum equations on all faces of the polygon into the continuity equation. The resulting matrix equation governs the water-surface elevation over the entire domain. This matrix equation is strongly diagonally dominant, symmetric, and positive definite; thus its unique solution can be efficiently determined by preconditioned conjugate gradient iterations until the residual norm becomes smaller than a given tolerance (Golub and van Loan, 1996). Once the free surface of the entire domain for the next time level has been calculated, the normal velocities on the faces of the prisms are calculated by back

substitution. The details of the finite-difference equations are not reproduced here and readers are referred to Casulli and Walters (2000).

The transport equation (9) for scalar variables is solved explicitly by using the velocity field obtained from the previous time step. An explicit finite-volume discretization that both conserves mass and guarantees that the solution will be bounded by the maximum and minimum of the initial and boundary values is used. In addition, a "flux limiter" is used in the discretization of the equation in order to limit numerical diffusion and preserve high accuracy at grid resolutions that are well-matched to the domain (Casulli and Zanolli, 2005). The flux limiter used in the simulations discussed here is the Superbee function (Roe, 1986).

In summary, the numerical solution scheme used in the computational core of UnTRIM to solve the governing equations is designed to achieve computational efficiency while retaining the accuracy of the solution. For the UKL simulations discussed in this report, the hydrostatic approximation was made. The simulations included the transport of three scalar quantities: turbulent kinetic energy, the rate of dissipation of turbulent kinetic energy, and heat. The equations describing the transport of each of these scalars are discussed below. Using the numerical solution scheme described above, the UnTRIM model required an average of 1.3 seconds of computational time per 2-minute simulation time step to solve the governing equations on the UKL grid, using a Dell 620 Latitude 1.66 GHz notebook computer with an Intel T2300 dual processor. A list of symbols used in this report is provided in table 1.

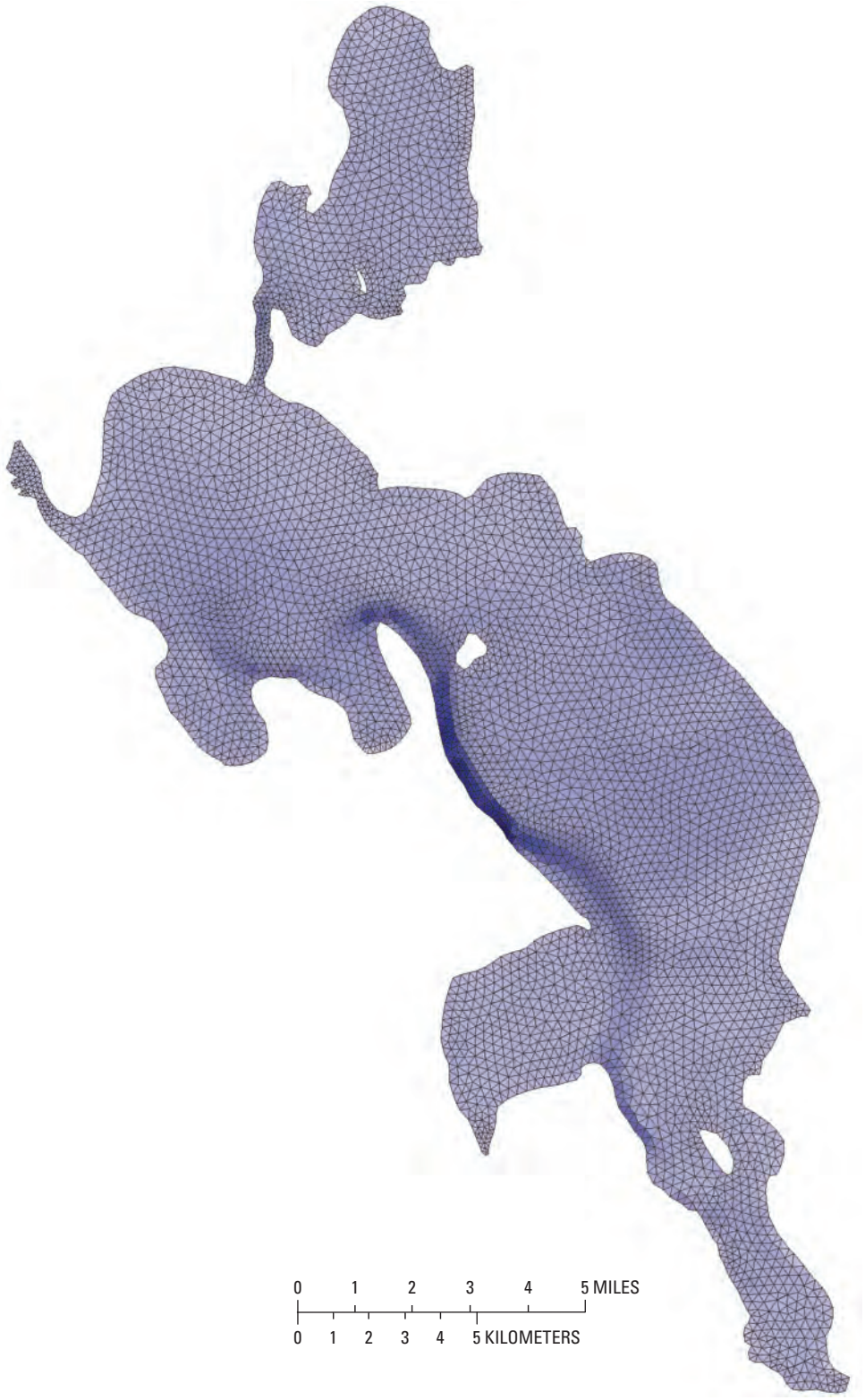

Figure 3. Unstructured orthogonal grid used in model simulations of Upper Klamath Lake, Oregon.

Table 1. List of symbols used in this report.

[**Abbreviations:** m, meter; s, second; J, joules; g, gram; °C, degrees Celsius; mb, millibar; W, Watt; kg, kilogram; N, Newton; °K, degrees Kelvin; –, no units]

Symbol	Name	Units
a	Constant in equation for surface drag coefficient	$(m\ s^{-1})^{-0.5}$
B	Production of turbulent kinetic energy by buoyancy	$m^2\ s^{-3}$
C	Concentration of scalar variable	arbitrary
C_{10}	10 m wind surface drag coefficient	–
C_B	Empirical coefficient	$mb\ °C^{-1}$
c_p	Specific heat capacity of water at 20°C	$J\ g^{-1}\ °C^{-1}$
c_μ^0	Constant used to relate turbulent kinetic energy to rate of turbulent kinetic energy dissipation	–
D_z	Vertical turbulent diffusivity coefficient	$m^2\ s^{-1}$
D_h	Horizontal turbulent diffusivity coefficient	$m^2\ s^{-1}$
e_s	Saturation vapor pressure of air at water surface temperature	mb
e_a	Vapor pressure of air	mb
f	Coriolis parameter	s^{-1}
g	Gravitational acceleration	$m\ s^{-2}$
H_B	Back radiation from water surface	$W\ m^{-2}$
H_E	Evaporative cooling	$W\ m^{-2}$
H_{LW}	Incoming longwave radiation	$W\ m^{-2}$
H_S	Sensible heat loss	$W\ m^{-2}$
H_{SW}	Incoming shortwave radiation	$W\ m\text{-}^{-2}$
h	Depth of the water column	m
K_z	Vertical turbulent viscosity coefficient	$m^2\ s^{-1}$
K_h	Horizontal turbulent viscosity coefficient	$m^2\ s^{-1}$
k	Turbulent kinetic energy	$m^2\ s^{-2}$
k_e	Extinction coefficient	m^{-1}
L_w	Latent heat of evaporation	$J\ kg^{-1}$
l	Length scale of turbulent eddies	–
M	Fraction of the sky covered by clouds	–
P	Production of turbulent kinetic energy by mean shear	$m^2\ s^{-3}$
p	Pressure	$kg\ m^{-1}\ s^{-2}$
p_a	Atmospheric pressure	$kg\ m^{-1}\ s^{-2}$
p_{sl}	Atmospheric pressure at sea level	$kg\ m^{-1}\ s^{-2}$
q	Non-hydrostatic component of pressure	$m^2\ s^{-2}$
R_{SW}	Shortwave radiation	$W\ m^{-2}$
r_B	Bottom friction coefficient	–
rh	Relative humidity	–
r_{LW}	Fraction of incident longwave radiation reflected at the water surface	–
r_{SW}	Fraction of incident shortwave radiation reflected at the water surface	–
S_D	Stability function used in calculation of turbulent diffusivity for constituent transport	–
S_K	Stability function used in calculation of turbulent diffusivity for momentum transport	–
T_a	Air temperature	°C
T_w	Water temperature	°C
t	Time	s
U,V	Depth-integrated components of velocity in the horizontal plane	$m\ s^{-1}$
u,v	Components of velocity in the horizontal plane	$m\ s^{-1}$
$\vec{u}_B$	Near-bottom velocity	$m\ s^{-1}$
$\vec{u}_i$	Wind vector at i m above the surface	$m\ s^{-1}$
$\vec{u}_T$	Current vector at the surface of the water column	$m\ s^{-1}$
$\vec{u}_*$	Friction velocity	$m\ s^{-1}$
w	Veritical component of velocity	$m\ s^{-1}$
w_s	Settling velocity	$m\ s^{-1}$
x,y	Cartesian coordinates in the horizontal plane	m
z	Vertical cartesian coordinate	m
z_B	Location of bottom computational grid point	m
z_0	Bottom roughness height	m
α_0	Proportionality constant	$°K^{-2}$
η	Free surface elevation	m
ε	Rate of dissipation of turbulent kinetic energy	$m^2\ s^{-3}$
ε_a	Emmisivity of air	–
ε_w	Emmisivity of water	–
κ	von Karman constant	–
ρ	Density of water	$kg\ m^{-3}$
ρ'	Depth-integrated deviation of water density from reference density, normalized by reference density	m
ρ_0	Reference density of water; density at 20°C	$kg\ m^{-3}$
ρ_a	Density of air	$kg\ m^{-3}$
σ	Stefan-Boltzmann constant	$W\ m^{-2}\ °K^{-4}$
σ_k	Turbulent Schmidt number for turbulent kinetic energy	–
σ_ε	Turbulent Schmidt number for dissipation of turbulent kinetic energy	–
$\vec{\tau}_B$	Stress vector at the sediment/water interface	$N\ m^{-2}$
$\vec{\tau}_T$	Stress vector at the water surface	$N\ m^{-2}$
ζ	Variable of integration	–

Turbulence Closure

The vertical turbulent dispersion of momentum and diffusion of heat are calculated within the model as spatial and temporal functions of two localized flow characteristics—turbulent kinetic energy k and the rate of dissipation of turbulent kinetic energy ε. Equations for the transport of these two turbulence characteristics can be written as:

$$\frac{\partial k}{\partial t}+\frac{\partial (uk)}{\partial x}+\frac{\partial (vk)}{\partial y}+\frac{\partial \left(wk\right)}{\partial z}=\frac{\partial}{\partial x}\left(D_h\frac{\partial k}{\partial x}\right)+\frac{\partial}{\partial y}\left(D_h\frac{\partial k}{\partial y}\right)+\frac{\partial}{\partial z}\left(\frac{K_z}{\sigma_k}\frac{\partial k}{\partial z}\right)+P+B-\varepsilon \quad , \tag{11}$$

$$\frac{\partial \varepsilon}{\partial t}+\frac{\partial (u\varepsilon)}{\partial x}+\frac{\partial (v\varepsilon)}{\partial y}+\frac{\partial \left(w\varepsilon\right)}{\partial z}=\frac{\partial}{\partial x}\left(D_h\frac{\partial \varepsilon}{\partial x}\right)+\frac{\partial}{\partial y}\left(D_h\frac{\partial \varepsilon}{\partial y}\right)+\frac{\partial}{\partial z}\left(\frac{K_z}{\sigma_\varepsilon}\frac{\partial \varepsilon}{\partial z}\right)+\frac{\varepsilon}{k}\left(c_1P+c_3B-c_2\varepsilon\right) \quad , \tag{12}$$

where

P and B are the production of turbulent kinetic energy by velocity shear and buoyancy, respectively, and

σ_k and σ_ε are the turbulance Schmidt numbers for k and ε, respectively.

The implementation of this two-equation turbulence closure model within UnTRIM is accomplished by using the generic length-scale approach of Umlauf and Burchard (2003) and Warner and others (2005), which provides a convenient and flexible means for implementing a wide variety of two-equation turbulence closure models. The choice of the generic coefficients—c_1, c_2, and c_3—that apply to the source and dissipation terms for the length-scale parameter ε determines which turbulence closure model is implemented. The $k-\varepsilon$ model (Rodi, 1993) was used in the simulations presented in this report. In accordance with Warner and others (2005), the choice of $c_1 = 1.44$, $c_2 = 1.92$, and $c_3 = -0.52$ was used to implement the $k-\varepsilon$ model in the case of stable stratification ($B < 0$). In the case of unstable stratification ($B > 0$), the weak thermal stratification in UKL generally resulted in too much mixing when buoyancy was considered to be a source of k and ε, so the buoyancy term B was set to zero in equations (11) and (12) when unstable stratification occurred. Equations (11) and (12) are solved within the model and the turbulent diffusivities, K_z and D_z for momentum and constituent transport, respectively, are calculated at each time step as:

$$K_z = (2k)^{1/2} l S_K \tag{13}$$

and

$$D_z = (2k)^{1/2} l S_D \quad . \tag{14}$$

The length scale of the turbulent eddies, l, is related to ε by $l = (c_\mu^0)^3 k^{3/2} \varepsilon^{-1}$, where c_μ^0 is a constant that depends on the stability functions used. The stability functions S_K and S_D are algebraic functions of k and ε that are derived by converting the system of differential equations for the second-order moments of turbulent quantities to a system of algebraic equations, thus eliminating a great deal of computational effort. The stability functions used in this application were those derived by Kantha and Clayson (1994). The solution of the equations (11) and (12) for k and ε is accomplished sequentially at each time step. The advective and diffusive transport is solved as described above for a scalar quantity. Then P, B, and ε are calculated from the velocity and density gradients, and then the source and sink terms of equations (11) and (12) are used to update k and ε. The implementation of this turbulence closure in UnTRIM is described by Celebioglu and Piasecki (2006a and 2006b).

Surface and Bottom Boundary Conditions

The shear stress at the surface of the water column, $\vec{\tau}_T$, is specified in terms of a surface drag coefficient C_{10}:

$$\vec{\tau}_T = C_{10}\rho_a \left|\vec{u}_{10}-\vec{u}_T\right|(\vec{u}_{10}-\vec{u}_T) \quad , \tag{15}$$

where

ρ_a is the density of the air,

$\vec{u}_{10}$ is the wind vector at 10 m above the water surface, and

$\vec{u}_T$ is the current vector at the surface of the water column.

The surface drag coefficient is in general an increasing function of the wind speed, and various formulations have been proposed and evaluated (Garratt, 1977; Smith and Banke, 1975). At very low wind speeds (less than about 3 m s^{-1}) experimental evidence shows that the wind surface drag coefficient increases with decreasing wind speed (Wuest and Lorke, 2003). In this application, an increasing C_{10} at low wind speeds did not bring the simulated currents closer to observed currents, and the following function for C_{10} was used:
$C_{10} = a\sqrt{\left|\vec{u}_{10}\right|}$ for 10-m wind speeds less than 15 m s^{-1}
and $C_{10} = a\sqrt{15}$ for greater wind speeds. The value of a was treated as a calibration parameter, although the final choice of $a = 0.0005$ was the value proposed by Wu (1969).

The shear stress at the sediment/water interface $\vec{\tau}_B$ is defined in terms of a bottom friction coefficient r_B and the near-bottom current speed $\left|\vec{u}_B\right|$ as:

$$\frac{\vec{\tau}_B}{\rho_0} = r_B \left|\vec{u}_B\right| \vec{u}_B = \left|\vec{u}_*\right| \vec{u}_* \quad , \tag{16}$$

where

$\vec{u}_*$ is the friction velocity.

Within the bottom logarithmic profile layer, the speed of the currents at distance z' away from the interface is given by (Schlichting, 1955):

$$\vec{u}(z') = \frac{\vec{u}_*}{\kappa} \ln\left(\frac{z'}{z_0}\right) \quad , \tag{17}$$

where

κ is the von Karmen constant (0.41) and
z_0 is the roughness height of the bed.

Combining these two expressions allows the solution of r_B in terms of the distance z_B of the lowest computational grid point away from the bottom, where $\vec{u}_B$ is defined:

$$r_B = \kappa^2 \left[\ln\left(\frac{z_B}{z_0}\right)\right]^{-2} \quad . \tag{18}$$

Wind Interpolation

The effort to develop an UnTRIM model of UKL began in 2003, and these efforts were reasonably successful at reproducing the hydrodynamics of the lake (Cheng and others, 2005). The early simulations showed that the currents in the lake were highly responsive to wind forcing at the surface, and it was determined that the biggest improvement in model performance would be obtained by generating a spatially accurate surface wind, rather than using a uniform surface wind over the entire lake. By 2005, additional monitoring sites had been established around the lake, as described below. Observations from these monitoring sites showed that the surrounding land topography influences the wind field over the lake, as evidenced, for example, by the fact that the prevailing wind direction over the northern part of the lake is westerly, but is northwesterly over the southern part of the lake (Hoilman and others, 2008).

An objective analysis model of the atmospheric boundary layer was used to interpolate the observations from the various wind-monitoring locations to a uniform grid (500-m spacing, both east-west and north-south) over the lake (Ludwig and others, 1991). The procedure for doing this involves starting with an initial "guess" interpolation and then modifying the initial guess iteratively to satisfy mass continuity. When temperature profiles in the lower atmosphere are available, the thickness of the surface flow is adjusted to the height at which the kinetic energy in the wind is equal to the work done against buoyant restoring forces. Surface winds flow over features of the terrain that are lower than this thickness, and around features that are higher than this thickness. Because temperature soundings in the near-surface around UKL are not part of the routine data collection around the lake, the full functionality of this model was not used. Instead, a stable and invariant adiabatic temperature profile in the atmospheric boundary layer was assumed.

Heat Transport

Source/sink terms that describe the transfer of heat across the air/water interface were added to the equation for conservative transport of a scalar variable (eq. 9). Surface terms include incoming shortwave and longwave radiation, outgoing longwave radiation, evaporative cooling, and conduction/convection. Computationally, all of these terms except for incoming shortwave radiation are included in the surface boundary condition. Incoming shortwave radiation is treated as an internal source/sink term that allows the radiation to be absorbed through a finite distance in the upper layers of the model water column rather than only at the air/water interface. The three-dimensional equation describing the transport of heat is:

$$\frac{\partial T_w}{\partial t} + \frac{\partial (uT_w)}{\partial x} + \frac{\partial (vT_w)}{\partial y} + \frac{\partial \left(wT_w\right)}{\partial z} = \frac{\partial}{\partial x}\left(D_h \frac{\partial T_w}{\partial x}\right) + \frac{\partial}{\partial y}\left(D_h \frac{\partial T_w}{\partial y}\right) + \frac{\partial}{\partial z}\left(D_z \frac{\partial T_w}{\partial z}\right) + \frac{1}{\rho_0 c_p}\frac{\partial R_{SW}}{\partial z} \quad , \tag{19}$$

where T_w is the water temperature, and

$$\frac{1}{\rho_0 c_p}\frac{\partial R_{SW}}{\partial z} \tag{20}$$

is the rate of temperature change at any depth z due to local absorption of shortwave radiation. The shortwave radiation at any depth z in the water column is given by:

$$R_{SW}(z) = H_{SW}(1 - r_{SW})e^{-k_e z} \quad , \tag{21}$$

where

H_{SW} is the shortwave radiation incident at the water surface in units of Watts/m^2,
r_{SW} is the fraction of H_{SW} that is reflected at the water surface (the albedo),
k_e is the extinction coefficient, and
c_p is the specific heat of water at 20°C.

The internal source/sink term is applied to the water temperature outside of the computational core of the model, with the result that at each time step, temperature over the entire domain is first updated to an intermediate value by physical transport; then, the change in heat resulting from the absorption of shortwave radiation is applied to the intermediate temperature.

The rest of the surface heat transfer terms are treated computationally as a boundary condition because they apply directly at the water surface. The boundary condition at the water surface is:

$$D_z \frac{\partial T_w}{\partial z} = -\frac{(H_{LW} - H_B - H_E - H_S)}{\rho_0 c_p} \quad , \tag{22}$$

where H_{LW}, H_B, H_E, and H_S are the incoming longwave radiation, reflected longwave radiation, evaporative heat flux, and sensible heat flux, respectively, all with units of Watts/m^2. This boundary condition is updated at every time step and the new value is supplied to the computational core of UnTRIM.

Of the surface heat transfer terms, only the incoming shortwave radiation H_{SW} is directly measured. The rest of the surface terms are calculated within the model at each time step by using standard formulations (McCutcheon, 1989; Martin and McCutcheon, 1999). Atmospheric long wave radiation is calculated from the Stefan-Boltzmann law, modified for the emissivity of the air:

$$H_{LW} = \varepsilon_a \sigma (1 - r_{LW})(T_a + 273.16)^4 \quad , \tag{23}$$

where

ε_a is the emissivity of the air,
σ is the Stefan-Boltzmann constant,
r_{LW} is the fraction of longwave radiation that is reflected at the water surface, and
T_a is air temperature in °C.

The emissivity of the air is calculated as:

$$\varepsilon_a = \alpha_0 (1 + 0.17 M^2)(T_a + 273.16)^2 \quad , \tag{24}$$

where

α_0 is a proportionality constant, and
M is the fraction of the sky covered by clouds.

Back radiation from the water surface also is calculated from the Stefan-Boltzmann law:

$$H_B = \varepsilon_w \sigma (T_w + 273.16)^4 \quad , \tag{25}$$

where

ε_w is the emissivity of the water, taken to be a constant.

Evaporative heat loss is calculated as:

$$H_E = \rho_0 L_w F (e_s - e_a) \quad , \tag{26}$$

where

$$F = 0.26(0.5 + 0.54|\vec{u}_2|) \quad , \tag{27}$$

where

F as the function of wind speed measured at height 2 m ($|\vec{u}_2|$) is a modified version of the original Penman equation (Janssen, 2006),
L_w is the latent heat of evaporation and is taken to be constant, and
e_s is the vapor pressure in the air, both in millibars.

The saturation vapor pressure at the water-surface temperature is given by (Dingman, 2002):

$$e_s = 6.11 \exp\left(\frac{17.3 T_w}{T_w + 237.3}\right) \quad , \tag{28}$$

and the vapor pressure in the air is calculated from relative humidity *rh* as:

$$e_a = 6.11 \exp\left(\frac{17.3 T_a}{T_a + 237.3}\right)\left(\frac{rh}{100}\right) \quad . \tag{29}$$

Sensible heat loss is often calculated from evaporative heat loss using the Bowen ratio:

$$H_S = H_E C_B \frac{p_a}{p_{sl}}\left(\frac{T_w - T_a}{e_s - e_a}\right) \quad , \tag{30}$$

where

C_B is an empirical coefficient,
p_a is local atmospheric pressure, and
p_{sl} is atmospheric pressure at sea level.

The sensible heat loss term is small compared to the other terms in eq. (22). In the UKL model the inclusion of this term tended to reduce the accuracy of the simulation, particularly during periods of atmospheric cooling when H_S was negative, so sensible heat loss was not included in the model simulations presented in this report.

Datasets

Tributary Inflows and Outflows

Inflows

The inflows to the UKL/Agency Lake hydrologic system include the Williamson River, the Wood River, the Fourmile and Sevenmile Canals, precipitation, and ground water. The biggest tributary is the Williamson River, which flows into UKL north of Eagle Ridge on the opposite shore (fig. 1). The Williamson River streamflow gage is located at river mile 10.3; daily values from the gage were used as input to the model (USGS site 11502500, fig. 1; Herrett and others, 2006; U.S. Geological Survey, 2007). Daily values of inflow from the next three largest tributaries—the Wood River, Sevenmile Canal, and Fourmile Canal—were provided by Graham Matthews and Associates (GMA) for 2005 (Cort Pryor, Graham Matthews and Associates, oral commun., 2006). These three tributaries empty into Agency Lake from the Wood River Valley (fig. 1). In 2005, the discharge at Fourmile Canal was estimated from August 13 through the end of the water year because equipment at the site failed. In 2006, daily values of inflow at Sevenmile Canal were provided by GMA (Cort Pryor, Graham Matthews and Associates, oral commun., 2006), but daily values were unavailable at either the Wood River or the Fourmile Canal. The discharge from these two sites was set to 3 m^3/s and 5 m^3/s, respectively, which was the approximate base flow based on the 2005 data. The remainder of the discharge from those two tributaries, which probably was substantial only during the early part of the summer, became part of the calculation of ungaged inputs during 2006 (fig. 4).

Daily precipitation data were collected at the Bureau of Reclamation (2008) Pacific Northwest Cooperative Agricultural Weather Network (AgriMet) site located near Agency Lake (AGKO, fig. 1). Because the UnTRIM model of UKL does not accommodate precipitation as a distributed input, one-third of the daily precipitation was added to the Wood River inflow, and two-thirds was added to the Williamson River inflow.

The ungaged inflows to the lake, including ground-water inflows, were calculated by using the daily lake stage (USGS site 11507001), which is a weighted average of the stage measured at three sites around the lake at Rattlesnake Point, Rocky Point, and Klamath Falls (fig. 1), and the volume of the lake as a function of lake stage, which was calculated from the same bathymetry used to create the model grid.

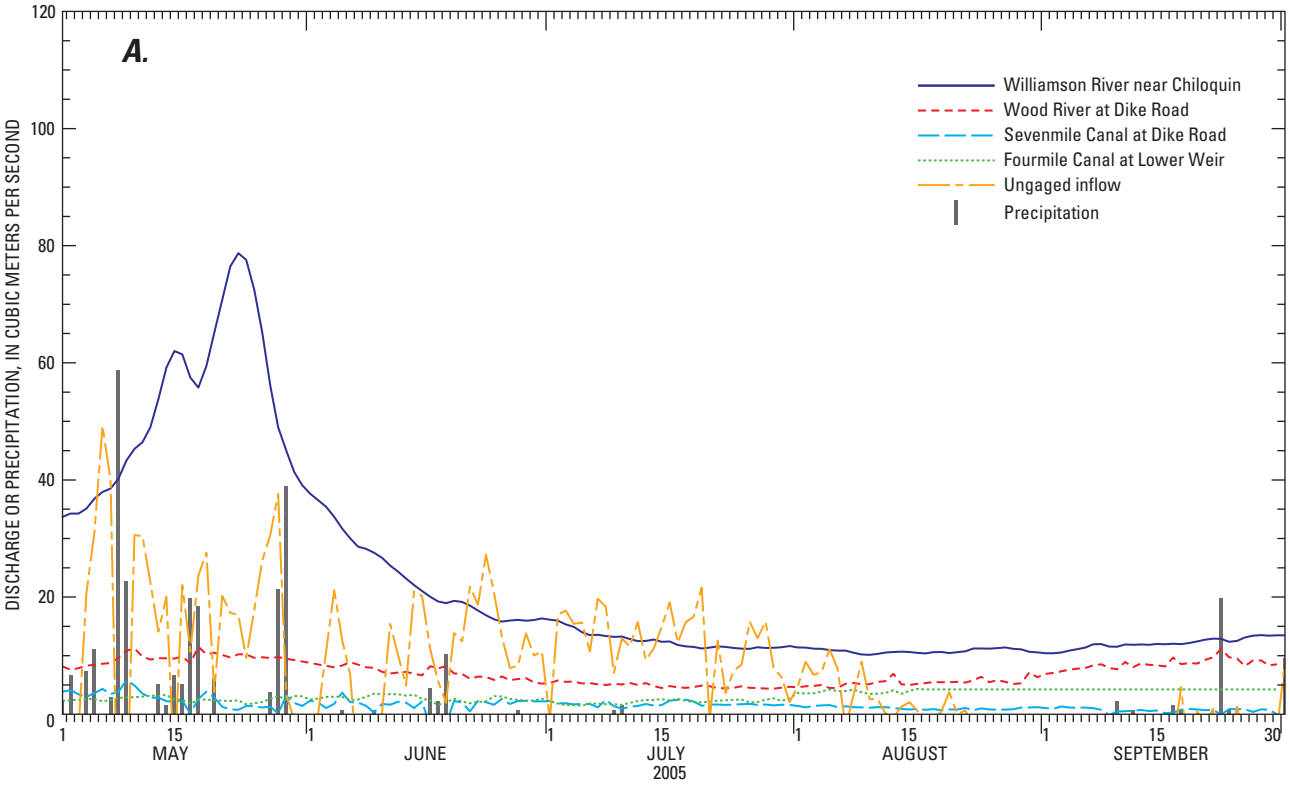

Figure 4. Inflows to the Upper Klamath Lake/Agency Lake hydrologic system in Oregon in (*A*) 2005 and (*B*) 2006.

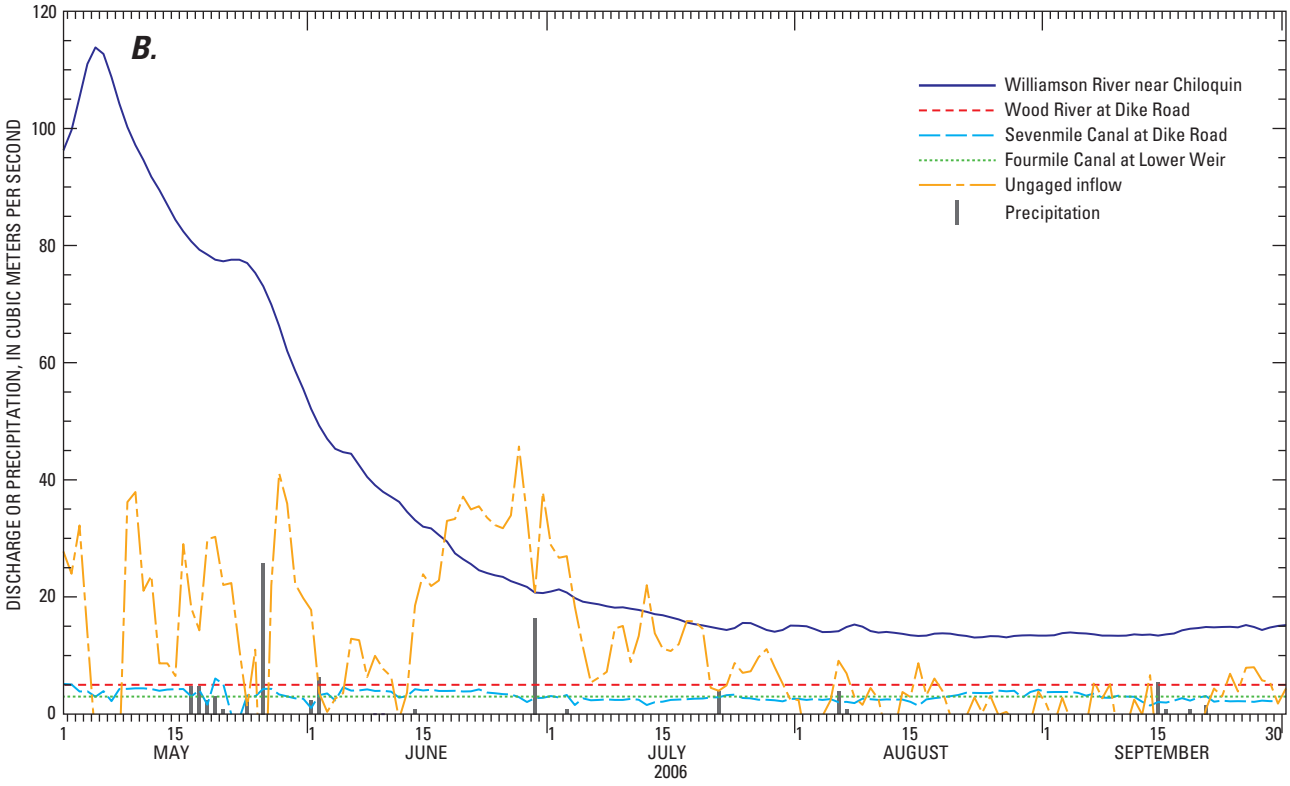

Figure 4.—Continued.

This bathymetry is based on a survey of approximately 94,200 soundings done in May and June of 1996. These soundings were oriented in east/west transects, providing a 200-m north/south spacing between the transects, and were thinned to a minimum of 50-m spacing along the transects (M. Neuman, Bureau of Reclamation, oral commun., 2007). If the change in volume of the lake at each time step is denoted ΔV, then the ungaged inflow, R, at each time step is calculated as:

$$R = \sum outflows - \sum inflows + \Delta V \quad . \qquad (31)$$

The ungaged inflow is sometimes large compared to inflow from tributaries to the lake, particularly in the spring and early summer, and at other times is negative, indicating ungaged outflow rather than inflow (fig. 5). It is also, at times, large when compared to the estimate of 8.5 m^3/s of groundwater inflow to the lake (Hubbard, 1970). Within the model, when the ungaged inflow is positive it is added to the Wood River Valley inflows. When the ungaged inflow is negative (indicating ungaged outflow) it is added to the Link River discharge at the outlet of the lake. It is apparent that the gaged inflows to and outflows from the lake are not sufficient to close the water balance with high accuracy. The method used for calculating the ungaged inflow and applying it to the model assures, however, that a mass balance of water in the model is achieved.

The outflow from the lake at the Link River is gaged by the USGS (site ID 11507500; fig. 1). Daily values were used as input to the model. This gaged discharge does not include the portion of the flow that, prior to 2005, was diverted for power generation through a canal that ultimately discharges back into the Link River downstream of the gage. In 2005, no water was diverted through the power canal, so the discharge at the gage is an accurate measure of the total flow over the Link River Dam. In 2006, there may have been diversions through the power canal, but the discharge measurements through the canal were unavailable and, therefore, were incorporated into the model as an ungaged outflow (fig. 5).

The A canal (fig. 1) diverts water for irrigation from the southern end of the lake above the Link River dam. The flow through the A canal is gaged by the Klamath Irrigation District and the daily values were obtained from the Bureau of Reclamation (Paul Gregory, Bureau of Reclamation, oral commun., 2007).

Daily evaporation data were collected at the AgriMet site located near Agency Lake (AGKO, fig. 1) (Bureau of Reclamation, 2008). Because the UnTRIM model of UKL does not accommodate evaporation as a distributed outflow, the daily evaporation was added to the Link River outflow.

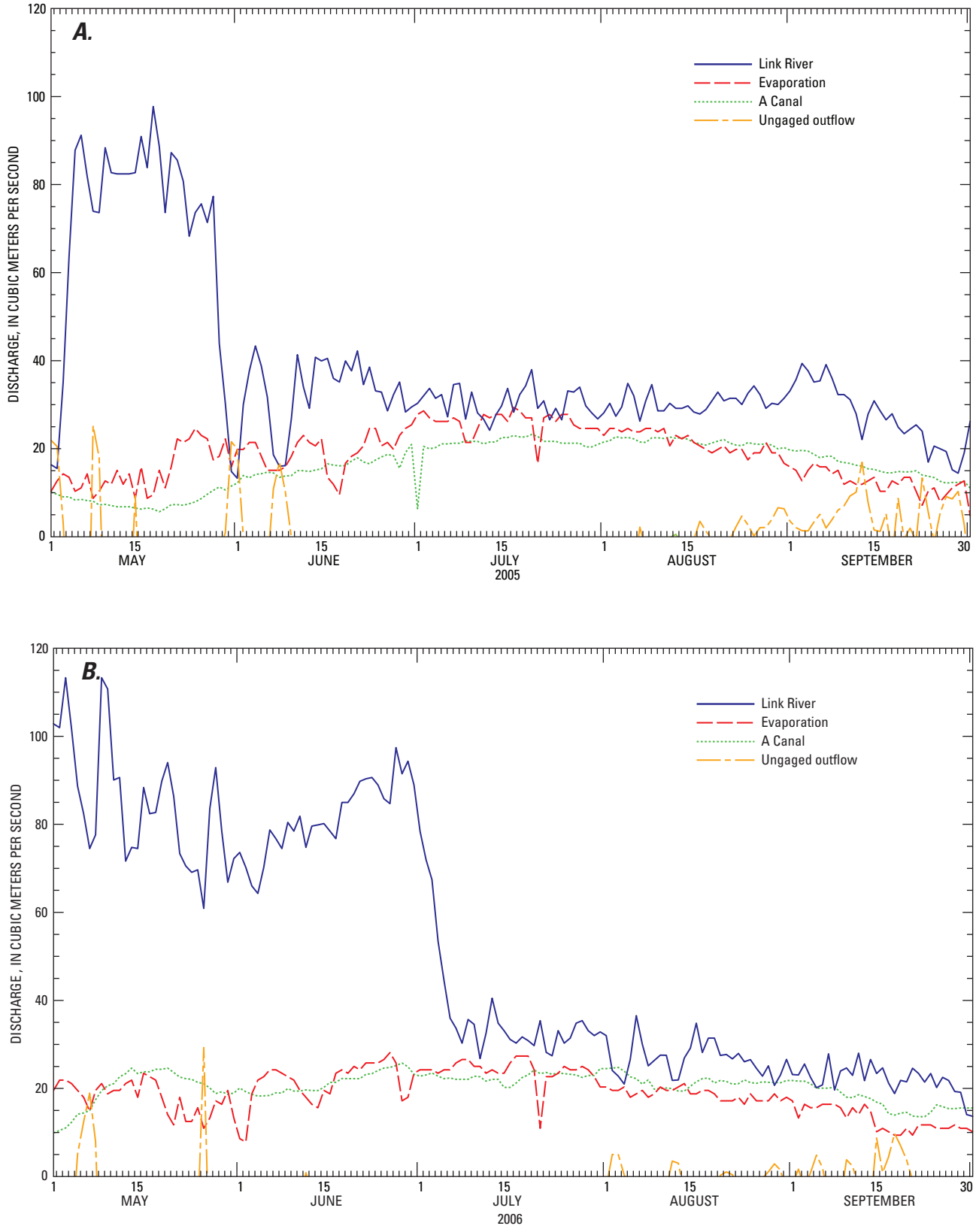

Figure 5. Outflows from the Upper Klamath Lake/Agency Lake hydrologic system in Oregon in (*A*) 2005 and (*B*) 2006.

Meteorological Data

Wind data were collected during 2005 and 2006 at two sites located on the lake and four sites located around the shoreline (fig. 1). After July 26, 2005, reliable data were available from at least five of the six sites (Hoilman and others, 2008). Prior to July 26, however, wind data were available from fewer sites. For this reason, three types of wind forcing covering different periods were used to run model simulations in 2005 (table 2). From June 8 (when the raft-mounted wind sensor at MDL was deployed in the lake at the beginning of the field season) to August 31 (when the wind sensors at MDL failed), the model was forced with a spatially uniform wind as measured at site MDL (denoted the UW-MDL simulation). From July 26 to October 12 (when the rafts on the lake were removed at the end of the field season), the model was forced with a spatially variable wind, interpolated as described above between sites on and around the lake (denoted the VW simulation). This resulted in an overlap period in midsummer between July 26 and August 31 for which these two simulations could be compared. To provide an additional comparison, during the same overlap period the model was forced with a spatially uniform wind as measured at site MDN (denoted the UW-MDN simulation). During 2006, wind data were available from six sites and a spatially variable wind forcing was used between May 20 and October 17. All meteorological data were collected as 15-minute averages in 2005 and 10-minute averages in 2006.

Air temperature and relative humidity were measured at five sites—WMR-MET, BLB-MET, HDB-MET, SSHR-MET, and MDL. Shortwave solar radiation was measured at sites WMR-MET and SSHR-MET. The measurements of air temperature and relative humidity at site MDL were used in these simulations with the exception of the period following September 4, 2005, when the sensors at site MDL failed. After September 4, 2005, the air-temperature data measured at the land-based station WMR-MET were used. The measurements of solar radiation from site WMR-MET were used in the simulations, with the exception of a few days prior to June 15, 2005, when the data from site WMR-MET were not yet available; solar data from the AgriMet site at Agency Lake (Bureau of Reclamation, 2008) were used for those days.

Calibration Data

Surface Elevation

USGS water-level gage data collected at three sites around the lake were used for water-level calibration. The sites were Upper Klamath Lake at Rocky Point (site ID 11505800), Upper Klamath Lake at Rattlesnake Point (site ID 11505900), and Upper Klamath Lake at Klamath Falls (site ID 11507000, fig. 1).

Velocity

Data used for calibration of water velocity came from five acoustic Doppler current profilers (ADCPs) deployed in the lake in 2005 and two ADCPs deployed in 2006 (fig. 1). These instruments and the velocity measurements collected have been described elsewhere (Gartner and others, 2007). Half-hourly velocity data were collected from the ADCPs between June 21 and September 12 in 2005, and between May 24 and September 25 in 2006. On July 5, 2006, the ADCP located at site ADCP1 was dragged by a barge from its initial deployment location to a location approximately 280 m away, where the meter continued to collect data.

Water Temperature

The data used for water temperature calibration in this report have been described elsewhere (Hoilman and others, 2008). These data were measured at 13 sites (1 m from the top and 1 m from the bottom at 3 sites) in 2005 and 12 sites (1 m from the top and 1 m from the bottom at 4 sites) in 2006 (fig. 1). At 3 of these sites in 2005 and 4 of these sites in 2006, a water-quality monitor was placed at 1 m from the surface and 1 m from the bottom, resulting in a total of 16 water-quality monitors in both years. At sites where only one monitor was used, it was placed at 1 m from the bottom or at the middle of the water column if the total depth was 2 m or less. Hourly data were collected from the 16 water-quality monitors between June 3 and October 11, 2005, and between May 15 and October 16, 2006. Five additional sites were added within 100 m of the shoreline in 2006, starting on June 14 (fig. 1, table 2).

Other Datasets

The extinction coefficient used in the model was determined from weekly vertical profiles of photosynthetically active radiation (PAR) at six water-quality monitoring sites. Light intensity was measured from the water surface to 2.5 m depth (or the lake bottom) in 0.5 m increments with a LiCor LI-193 spherical quantum sensor. These measurements were used to estimate the extinction coefficient by fitting an exponential relation based on Beer's Law to the vertical profile of the light meter readings. The methods are described in more detail by Hoilman and others (2008). A mean value of the extinction coefficient was used in the simulations presented in this report, which was obtained as a spatial and temporal average of the measured values for July and August of 2005 at all six sites.

The vertical profiles of light intensity were collected to support a weekly program of light and dark bottle incubations in 2005 and 2006. Calculations based on some of these

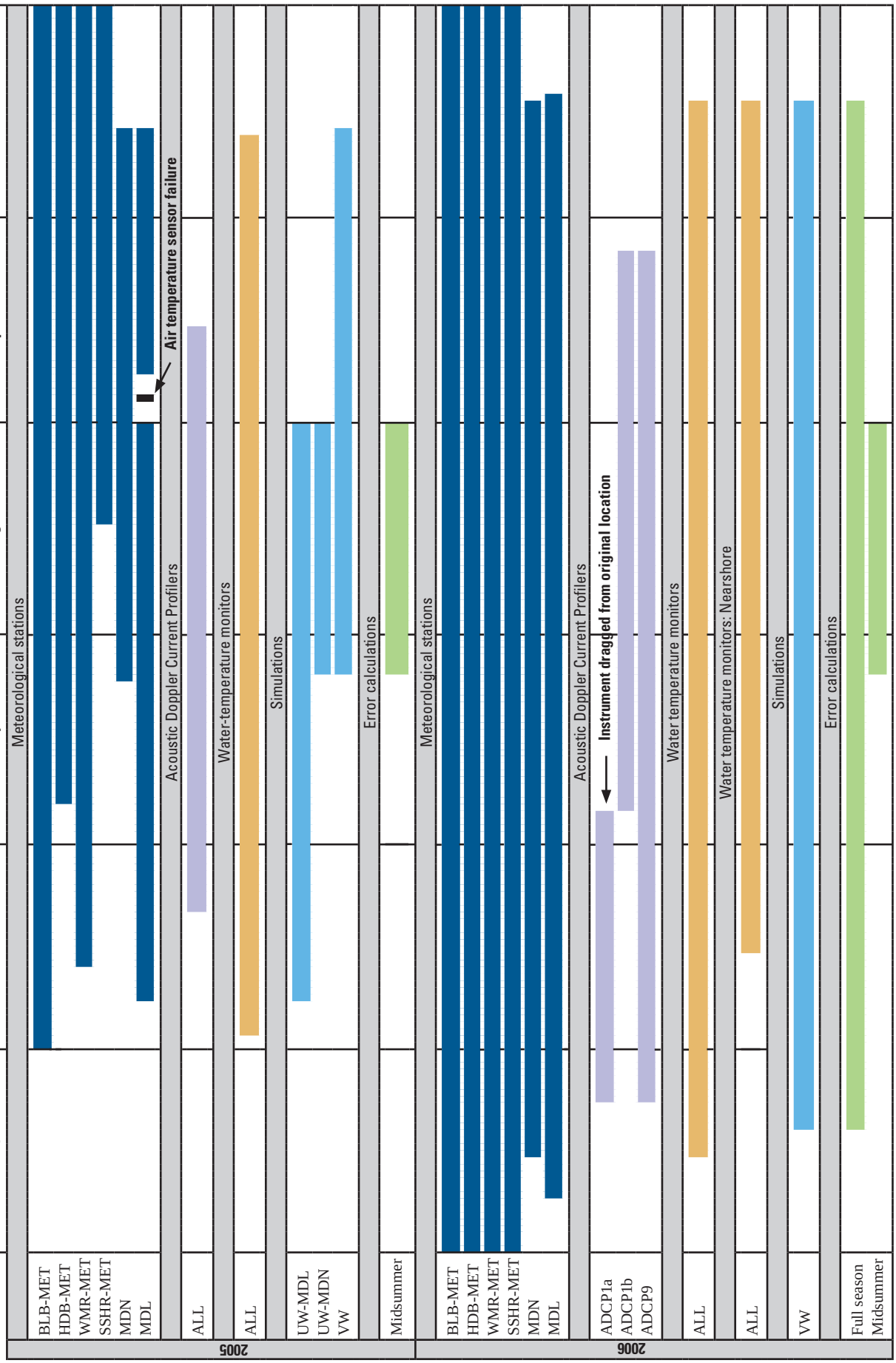

Table 2. Summary of the dates of availability of meteorological, velocity and water temperature data in Upper Klamath Lake between May and October of 2005 and 2006; summary of the simulation periods in 2005 and 2006, and the dates over which error statistics were calculated in 2005 and 2006.

data that were collected in 2006 are presented below in the discussion of the role of currents in determining water quality in the lake. The values of production and consumption obtained from the bottle incubations were converted to a change in dissolved oxygen concentration over a 24-hour period as detailed in Appendix A. Further details of data-collection methods are provided by Hoilman and others (2008).

The single value for the fraction of the sky covered by clouds that was used in the model simulations is the long term July-August average at the Medford, Oregon, airport (Oregon Climate Service, 2008). Because Medford is located about 130 km to the west of Klamath Falls and at about 830 m lower elevation, the daily values of cloud cover collected there are not expected to be accurate for Klamath Falls. The months of July and August in Klamath Falls are generally quite clear, but weather patterns in the spring and fall can result in periods of several cloudy days at a time. However, cloud cover is used only in the calculation of incoming longwave radiation (eq. 24), and the errors associated with using a constant value are expected to be small.

Simulation Results

Hydrodynamics

The hydrodynamic model was calibrated for 2005 by adjusting parameters a and z_0, which determine the surface and bottom friction coefficient, respectively (table 3). The same values for a and z_0 were used to run the model with the three different types of wind (UW-MDL, UW-MDN, and VW). In the UW-MDL simulation, a spatially uniform wind as measured at site MDL, a raft site in the southern part of the lake, was used. In the UW-MDN simulation, a spatially uniform wind as measured at site MDN, a raft site in the northern part of the lake, was used. In the VW simulation, a spatially variable wind was used. The spatially variable wind was determined from an interpolation of six sites, including the two raft sites and four others—WMR-MET, BLB-MET, HDB-MET, and SSHR-MET—located on the shoreline (fig. 1), with the exception that the data from site SSHR-MET were not included in the interpolation until August 18 when the sensors at that site started collecting data, and the data from site MDL were not included in the interpolation between September 1 and September 8 because the sensors at that site failed. The availability of data from the various meteorological sites and the periods covered by the three simulations were discussed previously and are summarized in table 2. In all cases the model was run for 5 days or more prior to the start of any error calculations in order to allow oscillations resulting from the startup of the model to dissipate.

The gaged and simulated lake elevation at two sites, UKL at Rocky Point, near the northern end of the lake, and UKL at Klamath Falls, near the southern end, are shown in fig. 6. These two gages show that the lake surface rises at the southern end and falls at the northern end on a daily basis, in response to the diel wind fluctuation. The model reproduces the timing of the oscillations well, although the simulated amplitude is larger than observed at the gages, particularly at the Klamath Falls gage, as can be seen in detail from July 15 to July 30. The VW simulation results in simulated oscillations closer to the observed amplitude than the UW-MDL simulation (fig. 6).

Prevailing winds over UKL blow over the northern part of the lake from the west to slightly northwest and are constrained by the surrounding topography to a northwest wind over the southern two-thirds of the lake, where the wind sensor at site MDL was located (Hoilman and others, 2008, fig. 7). On a typical day, wind speed picks up in the early to midafternoon and then dies down in the late evening or early morning. Typically, early morning is the calmest time of day. The response of the currents to moderate, prevailing winds is a relatively well-defined clockwise circulation consisting of broad, shallow flow in the direction of the wind on the eastern side of the lake and passing to the east of Bare Island, and a narrow, deep flow opposing the wind through the trench along the western shoreline and passing to the west of Bare Island. Usually, a large fraction of the northward flow in the trench veers eastward both south and north of Bare Island, forming a gyre that circulates water between Bare Island and Rattlesnake Point. The rest of the northward flow continues into the northern part of the lake, completing a clockwise loop that circulates water between Rattlesnake Point and the northernmost part of UKL (fig. 8). A reversal in the wind direction that is sustained for several hours causes the currents in the trench to reverse, resulting in a stall in the circulation pattern. If the wind reversal lasts long enough (at least a day), the current loop between Bare Island and Rattlesnake Point can reverse as well (fig. 9).

All of the ADCP data collected during 2003–06 are described in Gartner and others (2007), but it is useful to describe the basic circulation pattern in the lake in order to provide context for the ADCP data used in calibrating the model. Site ADCP1 was located in the deepest part of the trench (fig. 1). The current speeds are higher in the trench than in the shallower parts of the lake; site ADCP1 was strategically located to capture some of the highest velocities in the lake (fig. 10). The direction of the currents at site ADCP1 is constrained by the bathymetry of the trench to approximately 310 degrees under prevailing wind conditions; during a wind reversal the currents change direction by 180 degrees (fig. 11). The other ADCPs also were in areas that have pronounced prevailing current directions, although not as pronounced as at site ADCP1. Site ADCP7 was located near

Table 3. List of inputs to the hydrodynamic and heat transport model of Upper Klamath Lake, Oregon.

[**How determined:** m indicates a measured quantity; c indicates a calibration parameter; l indicates a value determined from literature; p indicates a physical constant. **Abbreviations:** m, meter; s, second; J, joules; g, gram; °C, degrees Celsius; mb, millibar; W, Watt; kg, kilogram; N, Newton; °K, degrees Kelvin; –, no units]

Symbol	Name	Value	Units	How determined
a	Constant in equation for surface drag coefficient	0.00056	$(m\ s^{-1})^{-0.5}$	c
C_B	Bowen ratio empirical coefficient	0.61	$mb\ °C^{-1}$	[3]l
c_p	Specific heat capacity of water at 20°C	4.186	$J\ g^{-1}\ °C^{-1}$	p
c_μ^0	Constant used to relate turbulent kinetic energy to rate of turbulent kinetic energy dissipation	0.5544	–	[1]l
D_h	Horizontal turbulent diffusivity coefficient	0.01	$m^2\ s^{-1}$	[2]l
g	Gravitational acceleration	9.81	$m\ s^{-2}$	p
H_{SW}	Incoming shortwave radiation	Variable	$W\ m^{-2}$	m
K_h	Horizontal turbulent viscosity coefficient	0.10	$m^2\ s^{-1}$	[2]l
k_e	Extinction coefficient	2.9	m^{-1}	m
L_w	Latent heat of evaporation	2.5×10^6	$J\ kg^{-1}$	p
M	Fraction of the sky covered by clouds	0.23	–	m
p_a	Atmospheric pressure	871.4	mb	m
p_{sl}	Atmospheric pressure at sea level	1,013.25	mb	p
rh	Relative humidity	Variable	–	m
r_{LW}	Fraction of incident longwave radiation reflected at the water surface	0.02	–	c
r_{SW}	Fraction of incident shortwave radiation reflected at the water surface	0.05	–	c
T_a	Air temperature	Variable	°C	m
$\vec{u}_i$	Wind vector at i m above the surface	Variable	$m\ s^{-1}$	m
z_0	Bottom roughness height	0.0005	m	c
α_0	Proportionality constant	0.937×10^{-5}	$°K^{-2}$	[4]l
ε_w	Emmisivity of water	0.97	–	p
κ	von Karman constant	0.41	–	p
ρ_0	Reference of density of water	1,000	$kg\ m^{-3}$	p
ρ_a	Density of air (dry air at 20°C and *Pa*)	1.036	$kg\ m^{-3}$	p
σ	Stefan-Boltzmann constant	5.67×10^{-8}	$W\ m^{-2}\ °K^{-4}$	p

[1]Warner and others (2005).
[2]Bowie and others, 1985 and Lerman (1971).
[3]Bowen (1926).
[4]Martin and McCutcheon (1998), Swinbank (1963), and Wunderlich (1972).

the southern terminus of the trench at the mouth of Howard Bay. Current speeds there were the second highest of the five locations (fig. 10), and current directions were predominantly about 30 degrees east of due north, in alignment with the direction of the trench at that site. Sites ADCP3 and ADCP5 were located in shallower water in the northern third of the lake: site ADCP5 in a shallower section of the trench to the west of Eagle Point, and ADCP3 near the terminus of the trench north of Ball Bay (fig. 1). The current directions at both of these sites are not as tightly constrained by the bathymetry but still show a prevailing direction that indicates currents moving in a clockwise direction around the northern third of the lake (fig. 11). Current speeds at these sites are much lower than in the deeper sections of the trench (fig. 10). Site ADCP6 was located in the broad, shallow flow that moves over the eastern part of the lake; the current direction there was the most variable of all the sites, but it indicates flow primarily to the southeast (fig. 11). Current speeds at site ADCP6 were the lowest of those measured at the five sites (fig. 10).

Error statistics for the three simulations (UW-MDL, UW-MDN, and VW) for the midsummer overlap period between July 26 and August 31 are provided in table 4 and are presented visually for ADCP1 in fig. 12. Error statistics were calculated at each ADCP site for both the depth-averaged speed, which is calculated from all the bins in the water column, and for individual east-west and north-south velocity

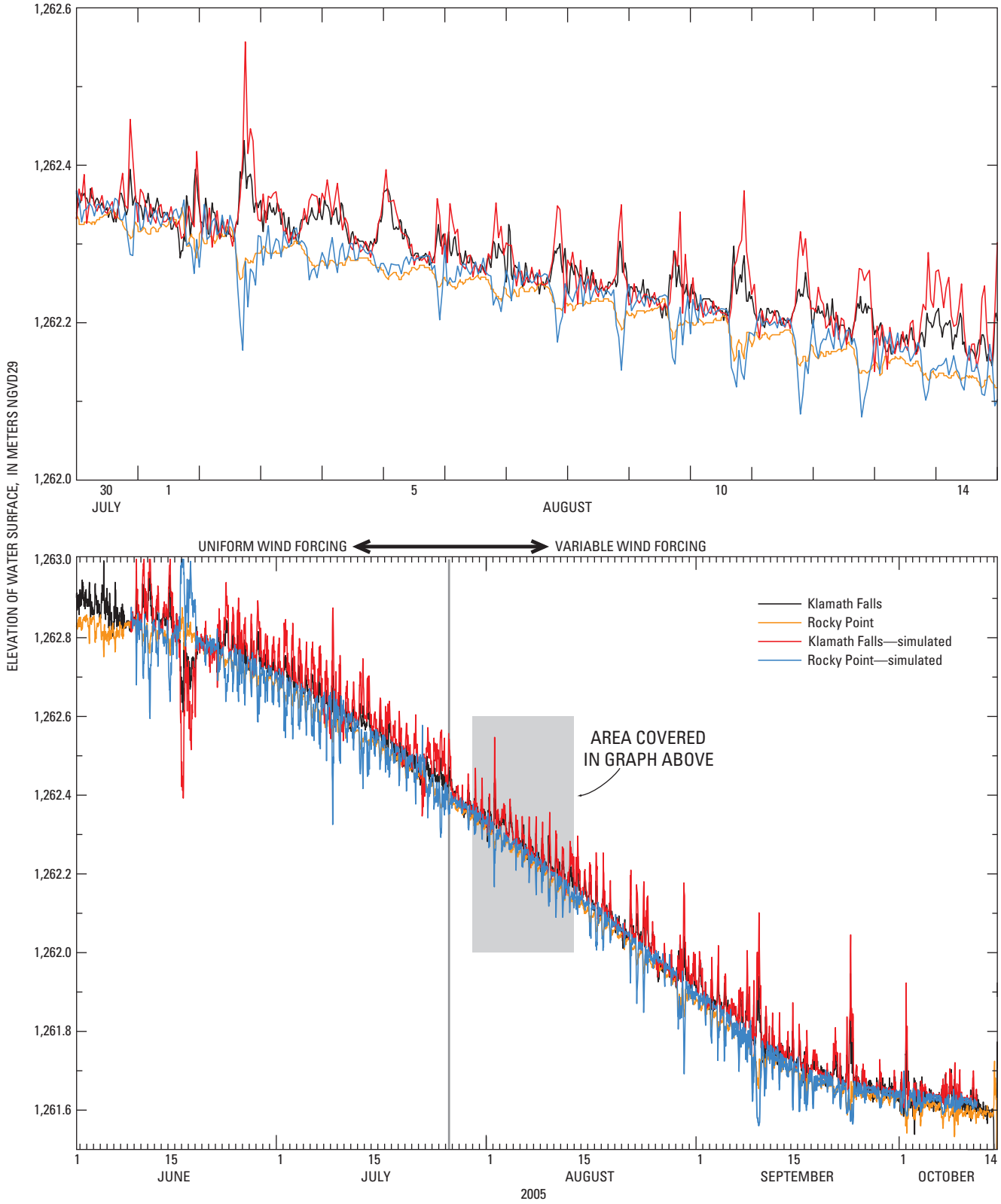

Figure 6. Hourly values of lake elevation at Upper Klamath Lake, Oregon, measured at two gages, 2005.

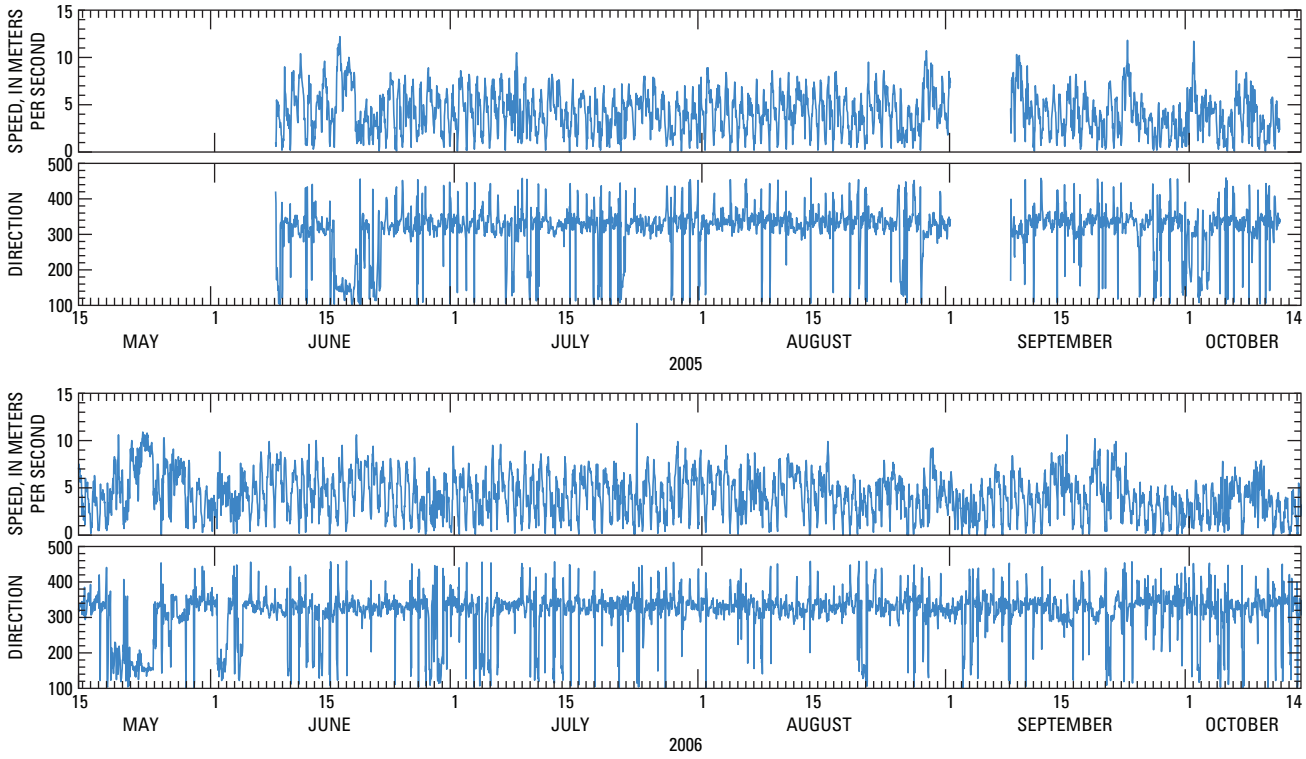

Figure 7. Wind speed and direction at site MDL in Upper Klamath Lake, Oregon. The wind direction ranges from 100 to 460 degrees because 360 degrees have been added to values of wind direction less than 100 degrees to avoid rapid numerical changes when the wind direction moves from east to west of north, and vice versa. The wind direction is referenced clockwise from north, and is the direction from which the wind is blowing.

components at two points in the water column—the bin closest to 1 m from the bottom and the bin closest to 1 m from the surface. The mean error (ME) in the simulated currents at all of the observation sites is provided as a measure of the overall bias of the simulation at each site. Errors are calculated as observed value minus simulated value, so a positive ME indicates simulated values less than observed values. The root mean squared error (RMSE) is provided as a measure of the overall goodness-of-fit of the simulation to the observations. The mean of the half-hourly observations and simulations also is provided for comparison. During the calibration process, emphasis was placed on correctly simulating the highest velocities through the trench, and as a result the ME and RMSE at site ADCP1 are small in comparison to the depth-averaged speed and the individual velocity components at that site (table 4, row 1 and rows 6–9, and fig. 10). In addition, both the ME and RMSE at ADCP1 are smaller for the VW simulation than for either of the uniform wind simulations, particularly in comparison to the UW-MDN simulation, which used only the wind measured in the northern part of the lake.

The second-best fit appears to be at site ADCP6 (table 4, row 4), where velocities are low. Comparison of the individual velocity components table 4, rows 18–21) indicates that, while the speed at this site is captured well by the VW simulation, the direction of the simulated currents is rotated to the west of the observations (fig. 11). At site ADCP6, the VW simulation produces a better result than the UW-MDL simulation, even though site ADCP6 was coincident with the meteorological site at MDL.

The simulated mean current speeds at the remaining sites are biased low in the VW simulation, as indicated by a positive ME, particularly at sites ADCP5 and ADCP7 (table 4, rows 3 and 5) and to a lesser extent at site ADCP3 (table 4, row 2). The ME of the average current speed at sites ADCP5 and ADCP7 is less for the UW-MDL simulation than for the VW simulation (table 4, rows 3 and 5); at site ADCP5 the RMSE also is less for the UW-MDL simulation than for the VW simulation (table 4, row 3). Site ADCP5 is located in the northern part of the lake; yet, if a uniform wind forcing is used, the currents there are better simulated by using winds measured in the central part of the lake than in the northern part of the lake closer to the site. This underscores that fact that success in accurately simulating the currents anywhere in the lake is dependent on having an accurately measured wind over as much of the lake as possible, rather than an accurate wind measured nearby at a single point of interest. In the case that wind data are available at only a single point, site MDL is a better site for collecting wind to force the model because the

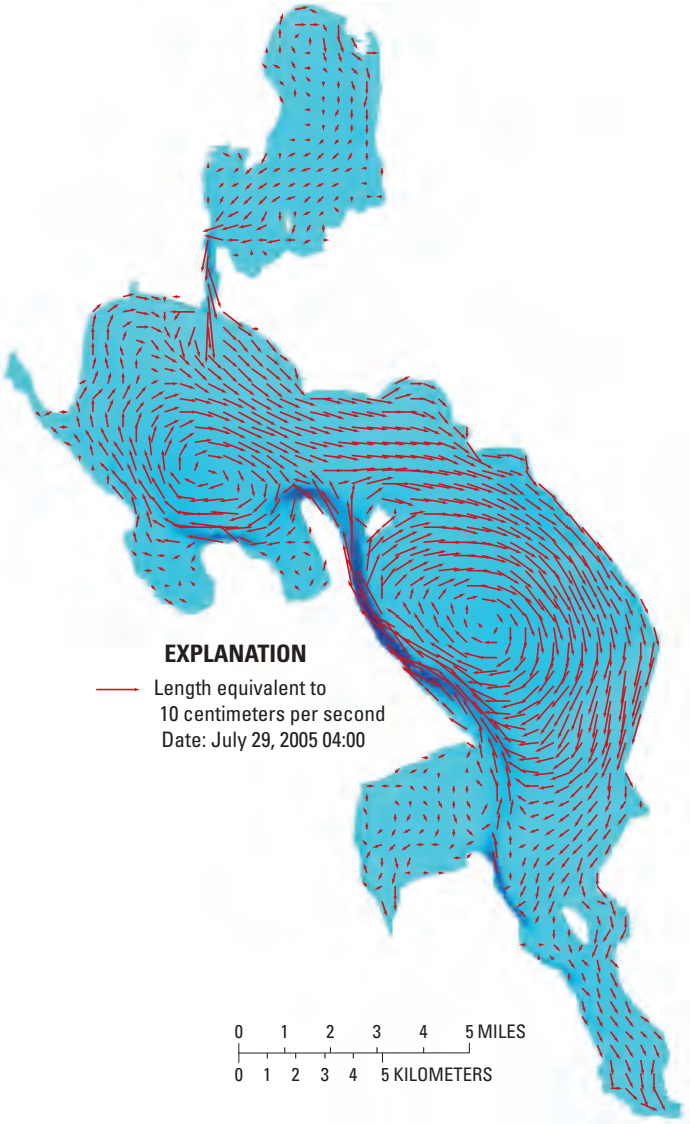

Figure 8. Simulated depth-averaged currents under prevailing (northwest) wind conditions, Upper Klamath Lake, Oregon.

Figure 9. Simulated depth-averaged currents under reversed (southwest) wind conditions, Upper Klamath Lake, Oregon.

wind data collected there probably represents a large surface area in the broad, central part of the lake where much of the momentum transfer from the wind to the water occurs; site MDN is not as good a choice because the wind data collected there represent a smaller surface area of the lake.

The ME statistics for the east-west and north-south velocity components (table 4, rows 6–25) are mixed with regard to whether the VW or the UW-MDL scenario produces the best simulation of the observations. The RMSE statistics, however, show consistent improvement with the VW simulation, with the exception of the near-bottom, north-south velocity component at site ADCP6 (table 4, row 20). Also apparent in the statistics (particularly the RMSE) for the individual components is the fact that the errors are consistently larger at the surface than at the bottom.

At site ADCP3, for example, the simulated north-south component of the surface currents has a tendency to be too large in the early afternoon, whereas the simulated east-west component has a tendency to be too small in the late afternoon (fig. 13 and table 4). The VW simulation reproduces the directional shift between the bottom and the surface better than the UW-MDL simulation (fig. 13).

At sites ADCP1, ADCP6, and ADCP7, the comparison between observed and simulated currents worsens from September 1 to September 8 (fig. 10). Because there is a data gap in the wind observations at site MDL during this time, a likely explanation is that the interpolated wind field is still dependent on observations at site MDL to provide accuracy in the wind forcing over the lake.

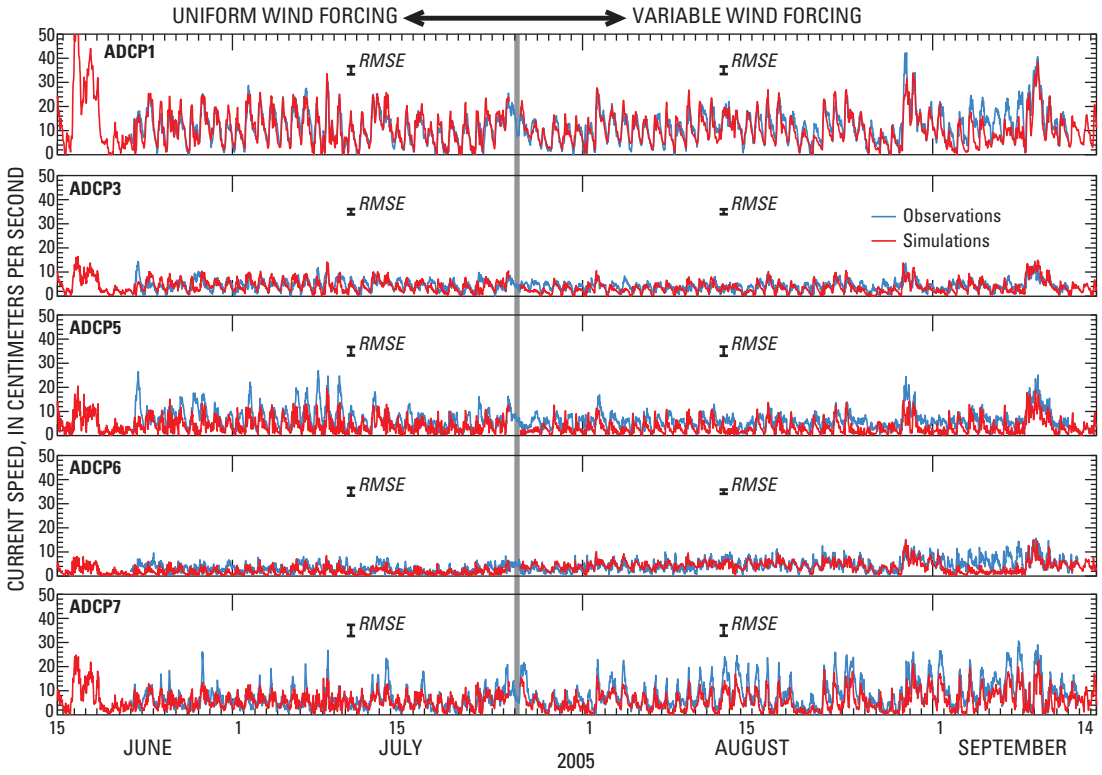

Figure 10. Observed and simulated current speeds at Acoustic Doppler Current Profiler (ADCP) sites in Upper Klamath Lake, Oregon, 2005. The error bar placed on graphs of speed indicates the root mean square error (RMSE) between the observed and simulated currents over the length of the simulation.

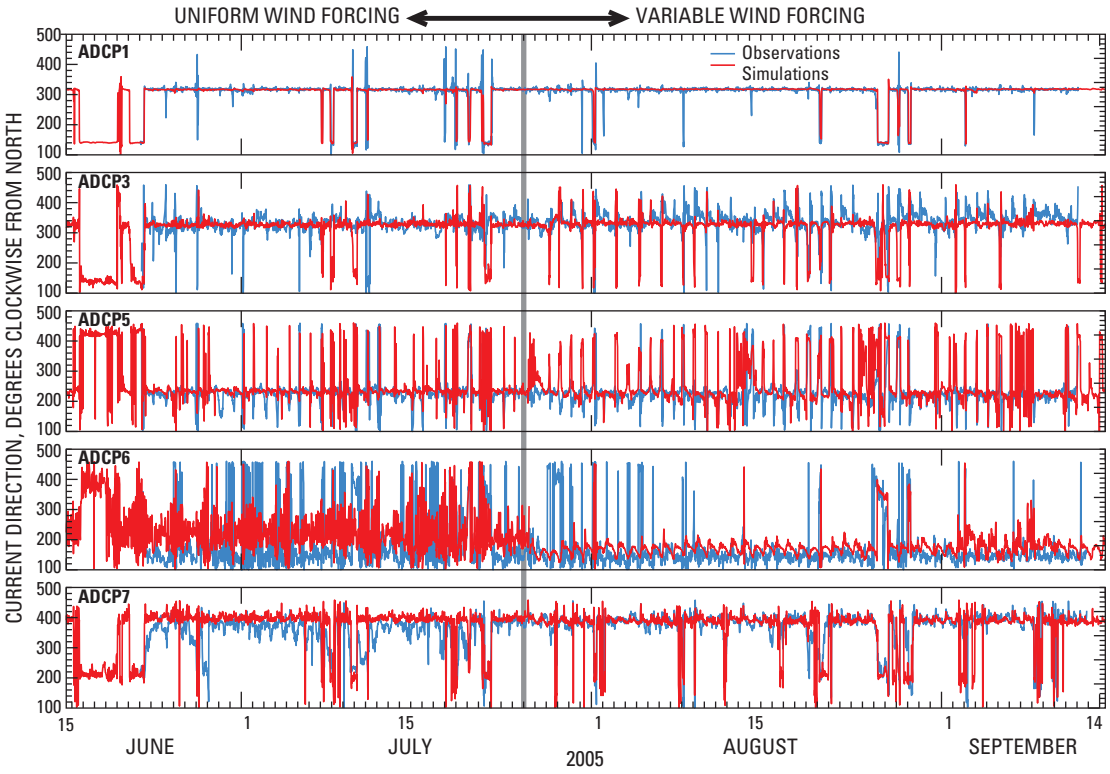

Figure 11. Observed and simulated current direction at Acoustic Doppler Current Profiler (ADCP) sites in Upper Klamath Lake, Oregon, 2005. The current direction ranges from 100 to 460 degrees because 360 degrees have been added to values of current direction less than 100 degrees to avoid rapid changes when the wind direction moves from east to west of north, and vice versa. The current direction is referenced clockwise from north, and is the direction to which the current is moving.

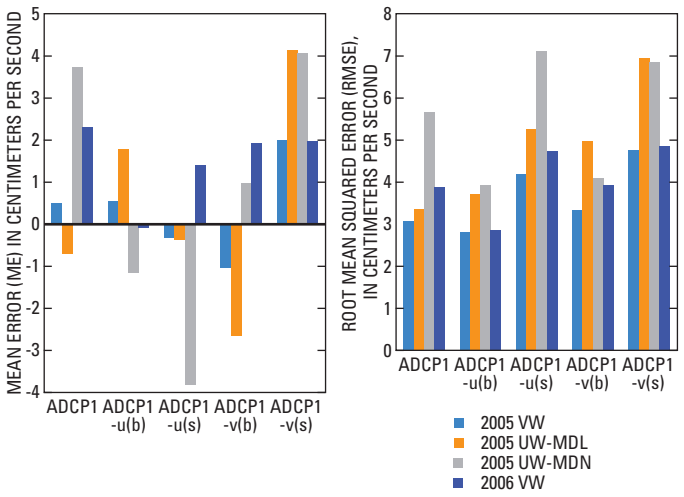

Figure 12. Goodness-of-fit velocity statistics at site ADCP1 in Upper Klamath Lake, Oregon, 2005 and 2006.

The model was validated using 2006 boundary conditions and forcing functions from May 20 to October 15. The values of the two calibration parameters, a and z_0, were the same as established during calibration for the 2005 season. This provided an opportunity to validate the performance of the model over nearly 5 months. The end-of-summer lake elevation in 2006 was lower than that in 2005 and revealed some inaccuracies in the representation of the bathymetry and shoreline in the model, as the simulated gages were without water after mid-September (fig. 14).

The observed and simulated current speed and direction at the two 2006 ADCP sites are shown in fig. 15. The visual comparison suggests that the underestimation of current speeds by the model simulation at site ADCP1 is greater in 2006 than in 2005, and this is confirmed by the ME statistics and the means (table 5, rows 1 and 2). In order to check whether the 2006 errors were larger

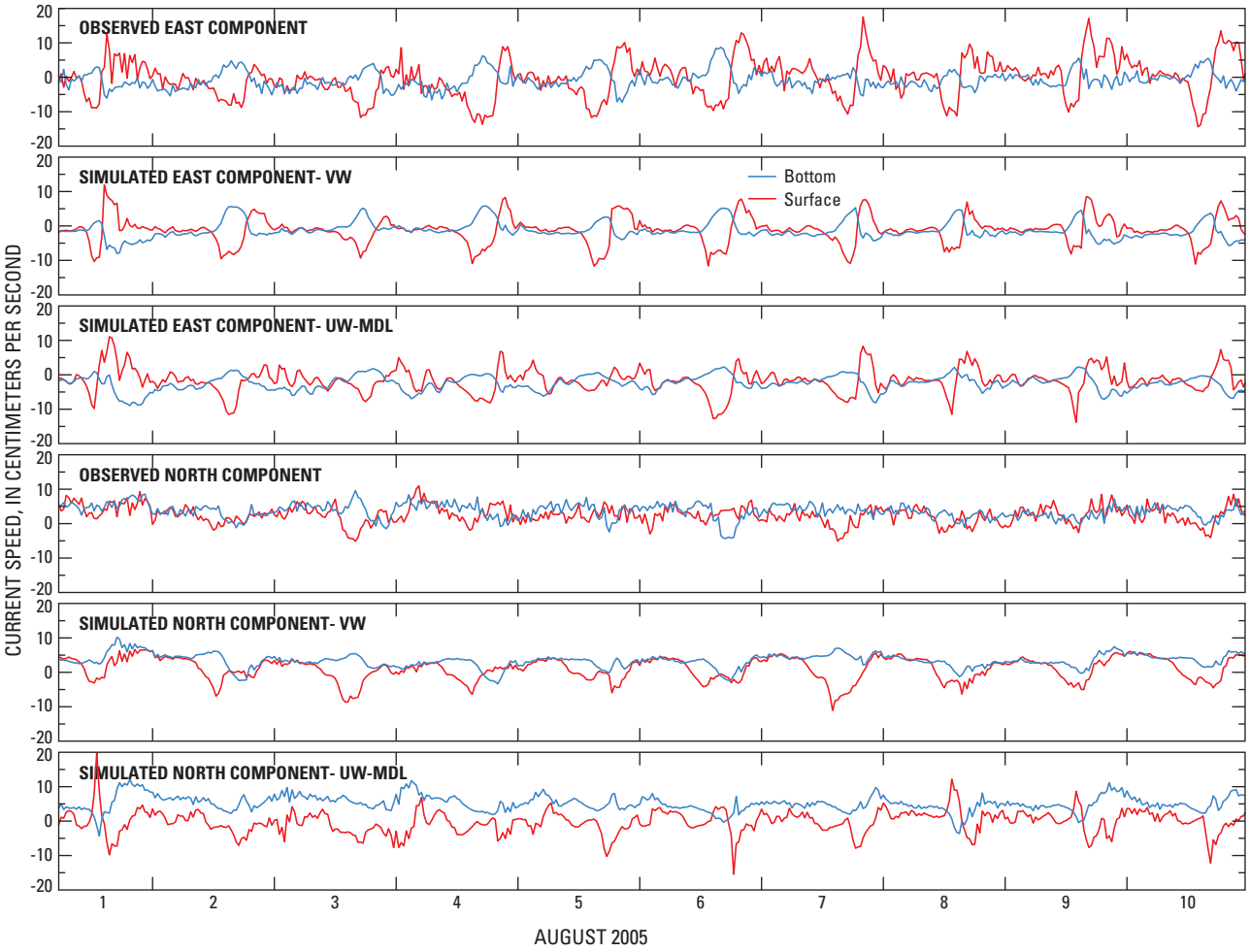

Figure 13. Observed and simulated east-west and north-south current components at site ADCP3 in Upper Klamath Lake, Oregon, 2005.

Table 4. Goodness-of-fit velocity statistics for the UnTRIM model of Upper Klamath Lake, Oregon, 2005.

[Errors are calculated half-hourly as observed value-simulated value. **Site modifier:** -u indicates east/west component of velocity; -v indicates north/south component of velocity; (b) indicates 1 meter from bottom, (s) indicates 1 meter from surface. **Mean and Root Mean Square:** VW indicates that the model was run using spatially variable wind forcing; UW indicates that the model was run using spatially uniform wind forcing as observed at the site indicated (MDN or MDL). **Abbreviations:** cm/s, centimeter per second; °C, degrees Celsius]

Row	Site	Mean of observations (°C)	Mean error (cm/s)			Root mean square error (cm/s)		
			VW	UW-MDL	UW-MDN	VW	UW-MDL	UW-MDN
			Depth-averaged speed					
1	ADCP1	11.23	0.50	-0.73	3.73	3.08	3.35	5.65
2	ADCP3	4.08	.80	-.48	1.10	2.04	2.20	2.41
3	ADCP5	5.81	2.58	1.89	1.95	3.77	3.52	3.80
4	ADCP6	4.44	-.07	2.54	2.08	1.77	3.25	3.14
5	ADCP7	8.38	3.02	1.66	5.01	4.38	4.60	7.11
			Velocity components					
6	ADCP1-u(b)	-6.15	0.54	1.74	-1.15	2.80	3.70	3.93
7	ADCP1-u(s)	-6.05	-.32	-.25	-3.82	4.19	5.23	7.11
8	ADCP1-v(b)	6.44	-1.02	-2.73	.96	3.32	4.98	4.10
9	ADCP1-v(s)	5.96	2.00	4.20	4.06	4.75	7.02	6.84
10	ADCP3-u(b)	-1.03	.29	1.16	.44	2.21	2.66	2.55
11	ADCP3-u(s)	-.40	.79	1.02	.79	4.73	5.34	4.61
12	ADCP3-v(b)	3.87	.63	-.84	1.47	2.15	2.78	2.67
13	ADCP3-v(s)	1.98	1.13	1.82	1.25	3.76	5.37	3.62
14	ADCP5-u(b)	-3.51	-1.84	-.65	-1.34	3.22	3.54	3.49
15	ADCP5-u(s)	-3.74	-1.26	-1.36	-1.85	3.78	4.63	4.45
16	ADCP5-v(b)	-2.30	-.99	-1.49	-.63	2.66	3.14	2.70
17	ADCP5-v(s)	-4.52	-.67	2.16	-.69	3.44	5.04	3.32
18	ADCP6-u(b)	1.50	.57	1.49	2.47	2.19	2.70	3.46
19	ADCP6-u(s)	6.07	5.05	5.82	6.85	8.10	8.62	9.97
20	ADCP6-v(b)	-1.28	3.57	.28	.14	4.44	2.90	2.54
21	ADCP6-v(s)	-8.55	-.48	-3.48	-5.44	5.61	6.96	8.96
22	ADCP7-u(b)	3.74	.80	.40	2.05	2.64	3.32	4.19
23	ADCP7-u(s)	5.52	2.72	.48	3.17	6.31	6.71	8.02
24	ADCP7-v(b)	7.82	2.82	1.63	6.77	4.37	4.82	9.25
25	ADCP7-v(s)	-1.23	-2.74	-3.23	-1.04	6.12	7.03	6.48

because of the longer simulation period in 2006, errors also were calculated over the same period (July 26 through August 31) that was used for the error calculations in 2005. Errors over this shorter period were comparable to those over the longer simulation, which seems to suggest that errors are not growing with the length of the simulation period. Nonetheless, the 2006 errors were larger for the July 26 through August 31 period than for the same period in 2005. For example, the RMSE at site ADCP1 was 3.88 for July 26 to August 31, 2006, as compared to 3.08 for the same period in 2005. It is not obvious why the model underestimates the currents in 2006, but it indicates that the calibration obtained for the 2005 data is not necessarily optimized for multiple years.

The simulation of the currents at the second 2006 ADCP site was less successful. This site, ADCP9, was located in the northern part of the lake, farther from the trench than either site ADCP3 or ADCP5 in 2005. The mean depth-averaged speed at this site during August was 3.42 cm/s (table 5), which was less than the speed at either of the northern sites in 2005 (table 4). The RMSE of 2.49 for the July 26 to August 31 period (table 5, row 3) is comparable to the errors at the northern sites in 2005 (table 4, rows 2 and 3), but a visual examination of the data shows that the simulation does not reproduce well the fluctuations in the observations, particularly on the time scale of several days (fig. 15). Site ADCP9 was located in a place where the currents were particularly complicated but not strong. The mean direction of the currents was toward 280–290 degrees clockwise from north at the surface, rotated about 20 degrees counterclockwise from the bottom (Gartner and others, 2007), so at this site more than at the northern ADCP sites in 2005, the currents directly opposed the prevailing wind direction observed at site MDN, where the strongest winds were approximately westerly, coming from 270–280 degrees clockwise from north (Hoilman and others, 2008). Thus, errors in the wind forcing at the site, as well as inaccuracies in the characterization of surface or bottom friction, will result in more noticeable discrepancies between observations and simulations at this site.

When putting the error statistics into perspective, it is important to understand that although ADCP technology is generally reliable and accurate for measuring water-current profiles, there are some inherent limitations and assumptions associated with those measurements, including two primary assumptions. First, since the instrument determines beam velocity from Doppler (or frequency) shift in the acoustic beams from backscattered signals, it is actually measuring the motion of particles in the water, not the actual water motion, which may be different. Second, the instrument transforms the beam velocities into earth coordinates, which requires the assumption that flow is essentially homogeneous in the four beams. There are error checks to discard obviously bad measurements but the assumption of homogeneous flow may impart some error. Because the four acoustic beams are oriented 20 degrees from vertical, the validity of that assumption is a function of distance from the transducer. Further, the instrument has a limited accuracy for each acoustic measurement. That accuracy (or “single ping”

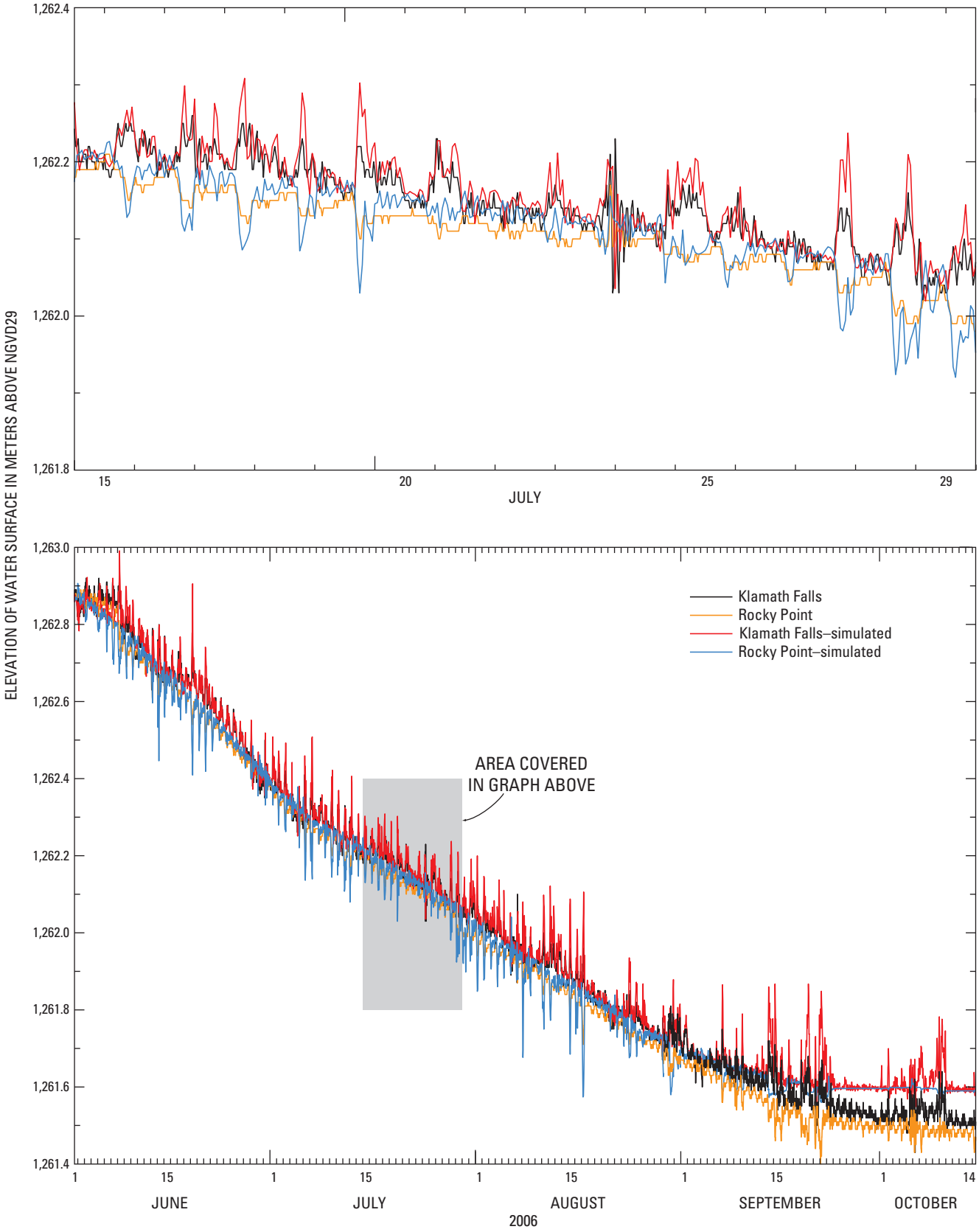

Figure 14. Hourly values of lake elevation at Upper Klamath Lake, Oregon, measured at two gages, 2006.

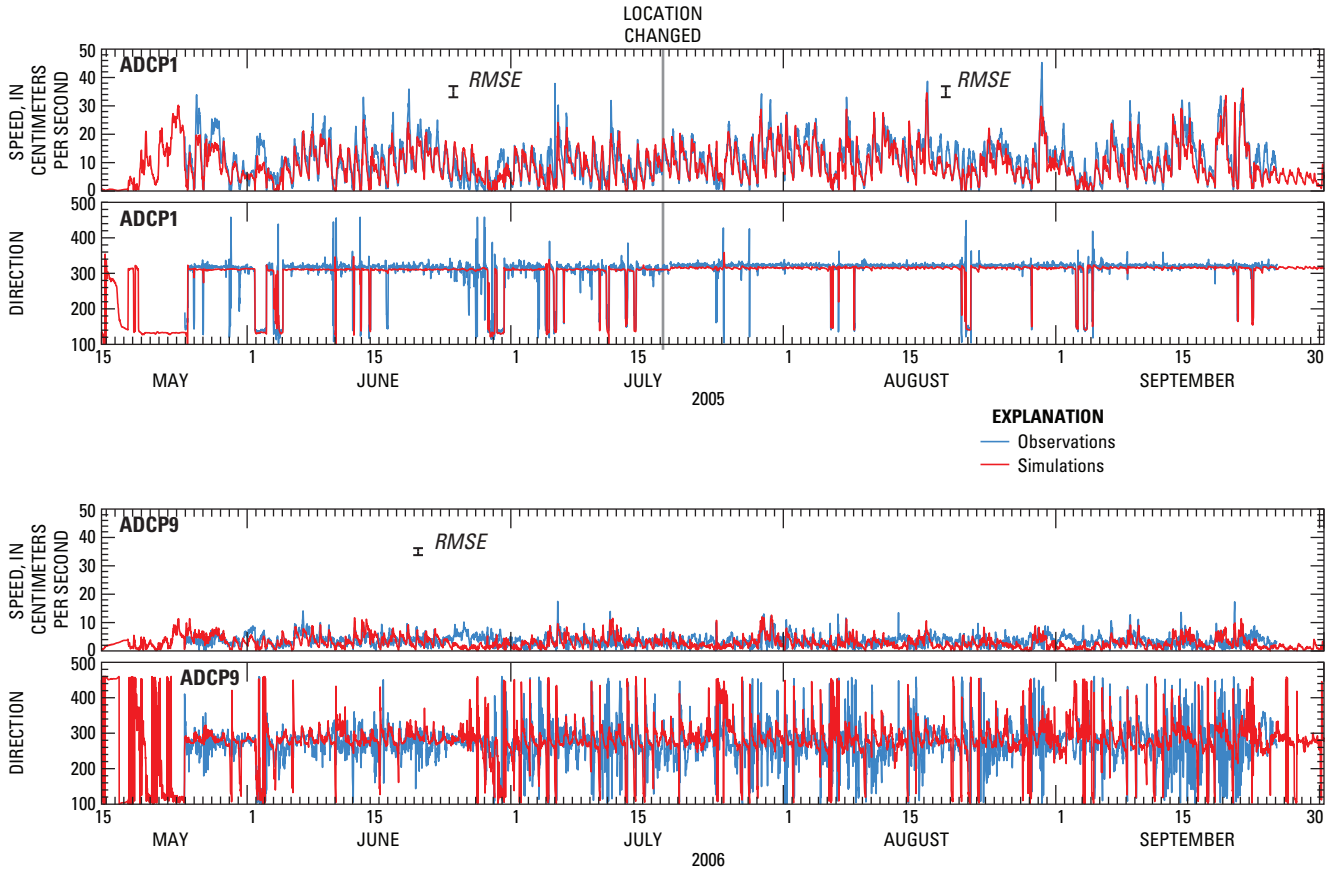

Figure 15. Observed and simulated current speed and direction at two Acoustic Doppler Current Profiler (ADCP) sites in Upper Klamath Lake, Oregon, 2006. The error bar placed on graphs of speed indicates the root mean square error (RMSE) between the observed and simulated currents over the length of the simulation. The current direction ranges from 100 to 460 degrees because 360 degrees have been added to values of current direction less than 100 degrees to avoid rapid numerical changes when the current direction moves from east to west of north, and vice versa. The current direction is referenced clockwise from north and is the direction to which the current is moving.

standard deviation) is typically reduced by averaging multiple pings to a single ensemble average that is then recorded. The (random) standard deviation is reduced by a factor of the square root of the number of pings. In the case of the ADCP measurements in UKL, the ADCP ensemble standard deviation or accuracy was about 0.73 cm/s for the horizontal velocity.

Overall, the calibration of the hydrodynamic model for 2005 and the validation for 2006 was successful. In both years, the biggest discrepancies between the observed and simulated currents occurred near the surface of the water column and indicated difficulty with simulating the friction boundary layer, so the errors in the depth-averaged speed were larger at shallow sites where the boundary layer is a bigger proportion of the water column. The simulation of the highest velocities through the trench was accurate, however, and provides confidence that the overall circulation patterns produced are correct. The validation of the model in 2006 produced currents that were somewhat underestimated in the trench, however, which indicated that even though the currents were accurately simulated at the same location in 2005 by adjusting only two calibration parameters, the model was not necessarily optimized for multiple years.

Table 5. Goodness-of-fit velocity statistics for the UnTRIM model of Upper Klamath Lake, Oregon, 2006.

[Errors are calculated half-hourly as observed value-simulated value. A spatially variable wind was used in the simulation. Full Season at ADCP1a is from May 24 to July 18 when the instrument was moved to a new position; full season at ADCP1b is from July 19 through September 25 at the new position; full season at ADCP9 is May 24 to September 25. Mid-summer is from July 26 to August 31. **Site modifier:** -u indicates east/west component of velocity; -v indicates north/south component of velocity; (b) indicates 1 meter from bottom, (s) indicates 1 m from surface. **Abbreviations:** cm/s, centimeter per second; –, no data]

Row	Site	Mean of observations (cm/s)		Mean error (cm/s)		Root mean square error (cm/s)	
		Full season	Mid-summer	Full season	Mid-summer	Full season	Mid-summer
		Depth-averaged speed					
1	ADCP1a	10.13	–	1.32	–	3.92	–
2	ADCP1b	12.42	12.98	2.17	2.30	3.83	3.88
3	ADCP9	3.65	3.42	.60	0.44	2.49	2.50
		Velocity components					
4	ADCP1a-u(b)	-6.01	–	-0.46	–	3.44	–
5	ADCP1a-u(s)	-5.16	–	-.06	–	5.20	–
6	ADCP1a-v(b)	5.87	–	.80	–	4.08	–
7	ADCP1a-v(s)	5.70	–	2.91	–	6.91	–
8	ADCP1b-u(b)	-6.36	-6.63	-.13	-0.08	2.82	2.84
9	ADCP1b-u(s)	-4.42	-4.84	1.61	1.41	4.92	4.72
10	ADCP1b-v(b)	8.51	8.89	1.81	1.92	3.85	3.92
11	ADCP1b-v(s)	4.65	5.71	1.17	1.96	4.95	4.86
12	ADCP9-u(b)	-3.14	-3.05	-.22	-.43	2.53	2.50
13	ADCP9-u(s)	-2.09	-2.08	-.28	.00	5.97	4.84
14	ADCP9-v(b)	.34	.31	-.80	-.96	2.55	2.50
15	ADCP9-v(s)	-.48	-.61	.62	.46	4.45	4.03

Heat Transport

The heat transport model was calibrated by adjusting one parameter, r_{sw}, the amount of incoming solar radiation reflected at the water surface. Comparisons between the observed and simulated temperature at the shallow sites where there was one continuous monitor, placed 1 m from the bottom, are provided in fig. 16. The goodness-of-fit temperature statistics for the midsummer overlap period of July 26 to August 31 are provided in table 6 for all three simulations and are presented visually for a subset of the sites in fig. 17. The absolute value of the ME of the VW simulation is less than 1°C at all sites and less than the ME of the UW-MDL simulation at most sites. The RMSE of the VW simulation also is less than 1°C at most of the sites, has a maximum value of 1.12, and is less than the RMSE of the UW-MDL simulation at most sites. The ME statistics are both positive (indicating an underestimation of the temperature) and negative (indicating an overestimation of the temperature), but the negative errors are larger, so that there a slight overestimation of the overall temperature around the lake during August, which is the warmest month. Interestingly, the RMSE of the UW-MDN simulation is generally comparable to and sometimes less than the RMSE of the VW simulation, indicating that the correct simulation of the currents is not required for correct simulation of the temperature. This underscores the fact that the temperature at any point in the lake is primarily a function of the meteorological forcing at the surface rather than advection.

After September 4, there is a noticeable increase in the diel range in temperature at some of the sites, which is due in part to the use of a land-based measurement of air temperature (from WMR-MET) to calculate incoming longwave radiation and evaporative heat loss for the boundary condition after the measurement of air temperature from the raft at site MDL became unavailable. The diel range in temperature over land is greater than that over water, primarily because the daily minimum is lower (fig. 18); the use of the measurement made over the water is preferable and generates more realistic results. Rapid drops in air temperature due to weather patterns such as those occurring around June 17, September 22, and October 1 appear to produce a more extreme response in simulated water temperature than is realistic. During these times, cloud cover is likely underestimated in the model by the use of a uniform value, and the incoming longwave radiation is therefore likely underestimated as well. Thus the incorporation of a temporally variable cloud cover, or directly measured longwave radiation, would likely moderate the simulated temperature response of the lake to these weather patterns.

Another important aspect of temperature simulation, in addition to correct simulation of the daily average temperature and temperature range, is the ability to predict the difference between the upper and the lower parts of the water column at those sites where the water is deep enough to stratify, including sites MDT, EPT, and MDN (Hoilman and others, 2008). Comparisons between the observed and simulated temperature records at the deep sites where there was a near-surface and near-bottom monitor in 2005 are provided in fig. 19. The observed and simulated daily maximum and daily minimum range in temperature from top to bottom at sites MDT, EPT, and MDN are shown in fig. 20. In general the VW simulation seems to be able to correctly reproduce those periods following July 26 when there is some temperature stratification that persists through several days; these are most noticeable at site MDT, the deepest site. The UW-MDL simulation does not reproduce those periods of persistent temperature stratification prior to

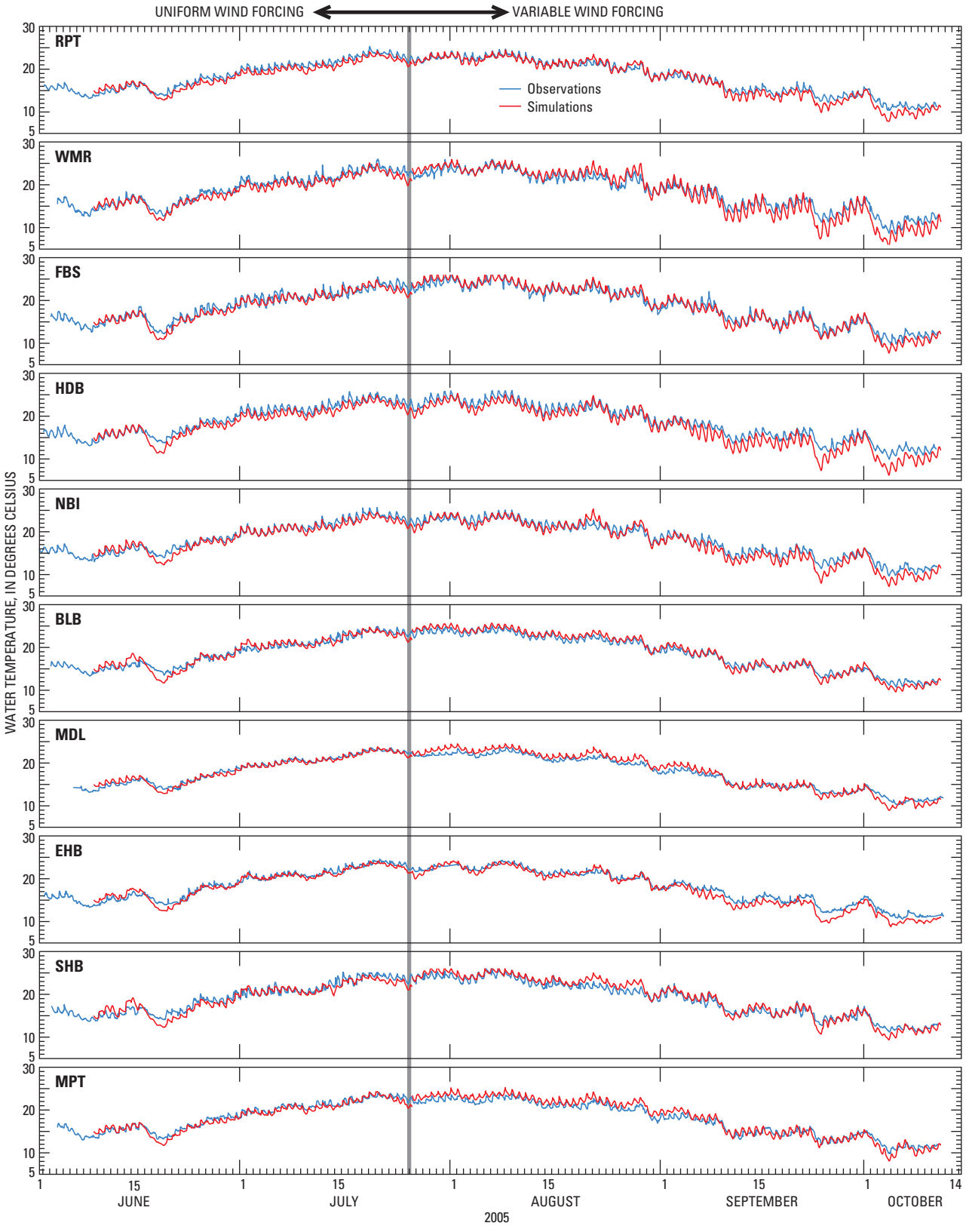

Figure 16. Observed and simulated temperatures at 10 shallow sites in Upper Klamath Lake, Oregon, 2005.

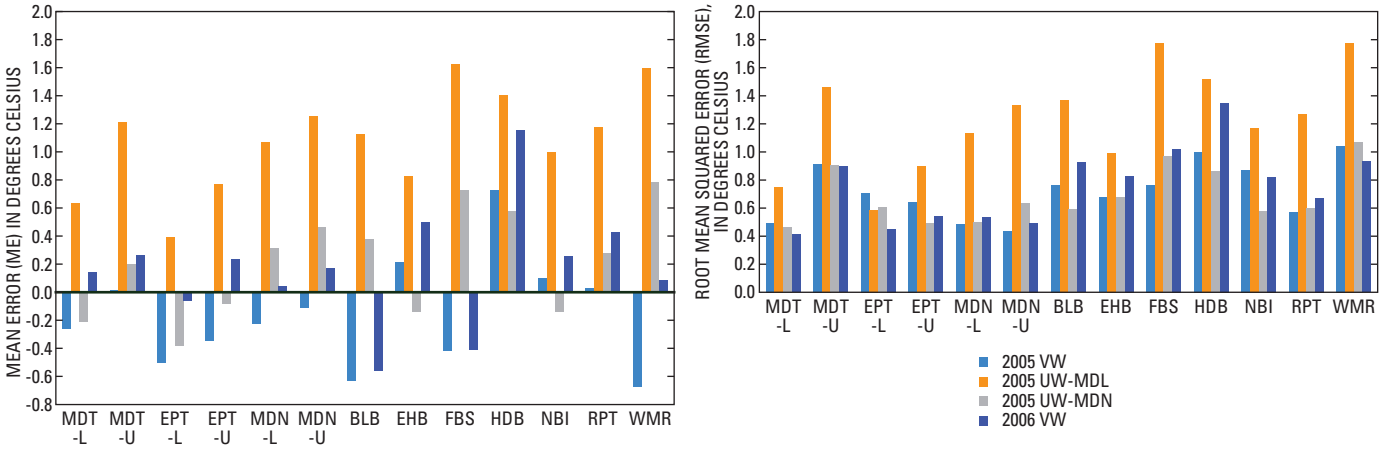

Figure 17. Goodness-of-fit temperature statistics at 13 sites in Upper Klamath Lake, Oregon, 2005 and 2006.

Table 6. Goodness-of-fit temperature statistics for the UnTRIM model of Upper Klamath Lake, Oregon, 2005.

[Errors are calculated hourly as observed value-simulated value. **Site modifier:** -L indicates monitor 1 meter from the bottom, -U indicates monitor 1 meter from the surface. **Site names** in boldface type indicate that temperature was measured at the site during both 2005 and 2006. **Mean and Root Mean Square Error:** VW indicates model run using spatially variable wind forcing; UW indicates model run using spatially uniform wind forcing as observed at the site indicated (MDN or MDL). **Overall mean** was calculated based on sites in boldface type only. **Abbreviations:** °C, degrees Celsius]

Row	Site	Mean of observations (°C)	Mean error (°C)			Root mean square error (°C)		
			VW	UW-MDL	UW-MDN	VW	UW-MDL	UW-MDN
			Sites with two water-quality monitors					
1	**MDT-L**	21.53	-0.26	0.63	-0.21	0.49	0.75	0.47
2	**MDT-U**	22.86	.01	1.21	.20	.92	1.46	.90
3	**EPT-L**	21.42	-.50	.39	-.38	.71	.59	.60
4	**EPT-U**	22.02	-.35	.77	-.09	.64	.90	.49
5	**MDN-L**	21.94	-.23	1.07	.31	.48	1.14	.50
6	**MDN-U**	22.37	-.11	1.26	.46	.43	1.34	.63
			Sites with one water-quality monitor at 1 meter from the bottom					
7	BLB	22.57	-0.63	1.12	0.37	0.77	1.37	0.59
8	**EHB**	21.61	.21	.83	-.14	.67	.99	.68
9	**FBS**	22.78	-.42	1.63	.72	.77	1.78	.97
10	**HDB**	22.35	.73	1.41	.58	1.00	1.52	.86
11	MDL	21.26	-.87	.50	-.31	.99	.67	.62
12	MPT	21.50	-.94	1.05	-.03	1.12	1.27	.83
13	**NBI**	21.80	.10	.99	-.14	.87	1.17	.58
14	**RPT**	21.67	.03	1.18	.28	.57	1.27	.60
15	SHB	22.66	-.85	1.37	.50	1.08	1.52	.84
16	**WMR**	22.18	-.68	1.60	.78	1.04	1.78	1.07
17	**Overall Mean**		-.12	1.08	.20	.72	1.22	.70

July 26. The model correctly reproduces the large diel variation in the near-surface layer while the near-bottom temperature remains more nearly constant during the day; this is true even at site MDN, the shallowest of the three sites, where two continuous monitors were deployed. The ME and RMSE goodness-of-fit statistics at the near-bottom monitors at the deep sites tend to be bigger than the goodness-of-fit statistics at the near-surface monitors at the same sites (table 6, rows 1–6).

The model validation run used observed 2006 meteorology between May 20 and October 15. The value of the calibration parameter, r_{SW}, was the same as that established during calibration for the 2005 season. The observed and simulated temperature records at the four deep sites where there was a near-surface and near-bottom continuous temperature monitor in 2006 are shown in fig. 21. The observed and simulated temperature at the eight shallow sites where there was one continuous monitor, placed 1 m from the bottom, are shown in fig. 22. In addition, in 2006 five continuous monitors were placed in nearshore locations (within 100 m of the shoreline), and the observed and simulated temperatures at these sites are shown in fig. 23. Error statistics were calculated over the entire 149-day simulation, and over July 26 to August 31 in order to compare to the results from the 2005 calibration (table 7). The ME was bigger over the longer period at some sites and smaller at others, but the overall ME was smaller over the entire simulation. The overall RMSE grew slightly from 0.75 to 0.88 from the 36-day simulation to the 149-day simulation (table 7, row 22). As in 2005, the largest errors were not at the deepest sites, where a monitor was located 1 m from the bottom and 1 m from the surface (table 7, rows 1–8; fig. 22). The top-to-bottom range in temperature at the deeper sites was generally well-simulated over the entire 149-day simulation (fig. 24).

At sites where temperature was collected in both 2005 and 2006, the RMSE was comparable over July 26 to August 31 (rows 1–10, 13,14, and 16 in table 6, and rows 1–6, 9–12, 14, 15, and 17 in table 7; fig. 17). The average of the RMSE over July 26 to August 31 at sites where temperature was collected in both 2005 and 2006 was 0.72 in 2005 and 0.75 in 2006. The ME for both the month of August and the entire simulation indicates that the model underestimated the temperatures, as there are more and larger positive errors than negative. Closer consideration shows that underestimation of temperature was more common at shallow and nearshore sites. The ME was greater than 1 at several sites (table 7)—all of these except site HDB were nearshore sites that were added in 2006 (fig. 23). The measured temperatures at the nearshore sites were generally higher than measured temperatures at the other sites (table 7). This may indicate that sediments play a role at these very shallow sites by absorbing incoming shortwave radiation that is transmitted through the entire water column and transferring some of the heat back to the water column. In the model, shortwave radiation that is not absorbed within the water column does not contribute heat to the water column. At some nearshore sites, most notably GBE and WDW, the simulated temperature shows greater diel swings than the observations (fig. 23); this may be an indication that the depth at these sites was not accurately portrayed in the model grid. At these very shallow nearshore sites, small errors in the bathymetry make a large proportional error in the depth of the water column.

Table 7. Goodness-of-fit temperature statistics for the UnTRIM model of Upper Klamath Lake, Oregon, 2006.

[Errors are calculated hourly as observed value-simulated value. **Site modifier:** -L indicates monitor 1 meter from the bottom; -U indicates monitor 1 meter from the surface. A spatially variable wind was used in the simulation. **Site names** in boldface type indicate that temperature was measured at the site during both 2005 and 2006. Full Season is from May 20 to September 25. Mid-summer is from July 26 to August 31. **Overall mean** is calculated based on sites in boldface type only. **Abbreviations:** °C, degrees Celsius]

Row	Site	Mean of observations (°C)		Mean error (°C)		Root mean square error (°C)	
		Full season	Mid-summer	Full season	Mid-summer	Full season	Mid-summer
	Sites with two water-quality monitors						
1	**MDT-L**	18.00	20.34	-0.16	0.14	0.59	0.41
2	**MDT-U**	19.15	21.53	-.11	.26	1.02	.90
3	**EPT-L**	17.81	20.18	-.29	-.06	.71	.45
4	**EPT-U**	18.45	21.05	-.08	.23	.67	.54
5	**MDN-L**	18.19	20.57	-.21	.04	.71	.53
6	**MDN-U**	18.54	20.95	-.14	.17	.67	.49
7	SET-L	18.16	20.35	.23	.52	.71	.68
8	SET-U	18.91	21.04	.37	.61	.78	.80
	Sites with one water-quality monitor at 1 meter from the bottom						
9	EBB	17.97	20.30	-0.65	-0.56	1.10	0.92
10	**EHB**	18.31	20.52	.13	.50	.85	.83
11	**FBS**	18.42	20.94	-.79	-.41	1.39	1.02
12	**HDB**	18.94	21.28	.61	1.16	1.21	1.35
13	MRM	18.06	20.49	-.59	-.18	1.01	.73
14	**RPT**	18.14	20.30	.00	.25	.76	.67
15	**NBI**	18.36	20.49	.13	.43	.91	.82
16	**WMR**	18.59	21.04	-.05	.08	1.07	.93
	Nearshore sites with one water-quality monitor at mid water column						
17	GBE	19.78	21.64	1.12	0.69	2.22	1.47
18	HPK	19.42	21.15	1.36	1.50	1.72	1.86
19	SHL	20.00	21.60	.86	1.09	1.23	1.31
20	WDW	19.51	21.51	.57	.13	1.66	1.21
21	SSR	20.49	22.30	.89	1.25	1.42	1.44
22	**Overall Mean**			-0.08	0.23	0.88	0.75

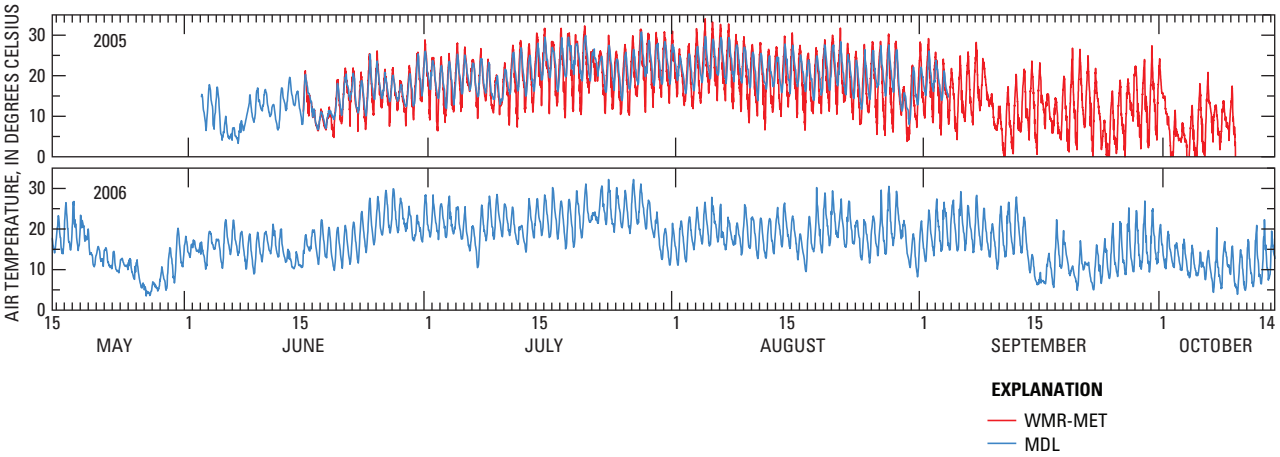

Figure 18. Air temperature at site MDL in 2005 and 2006, and air temperature at site WMR-MET in 2005, Upper Klamath Lake, Oregon.

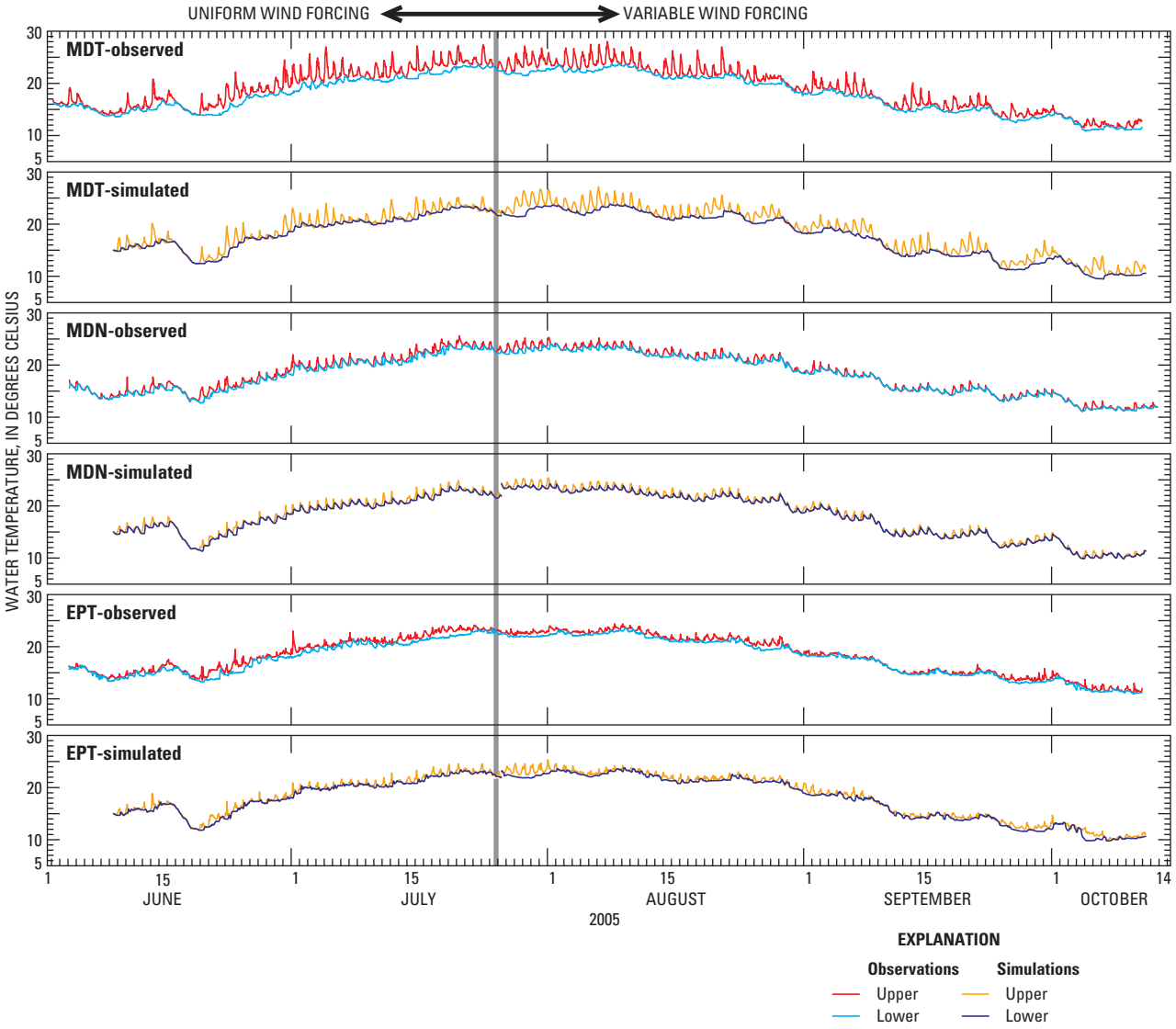

Figure 19. Observed and simulated temperatures at three deep sites in Upper Klamath Lake, Oregon, 2005.

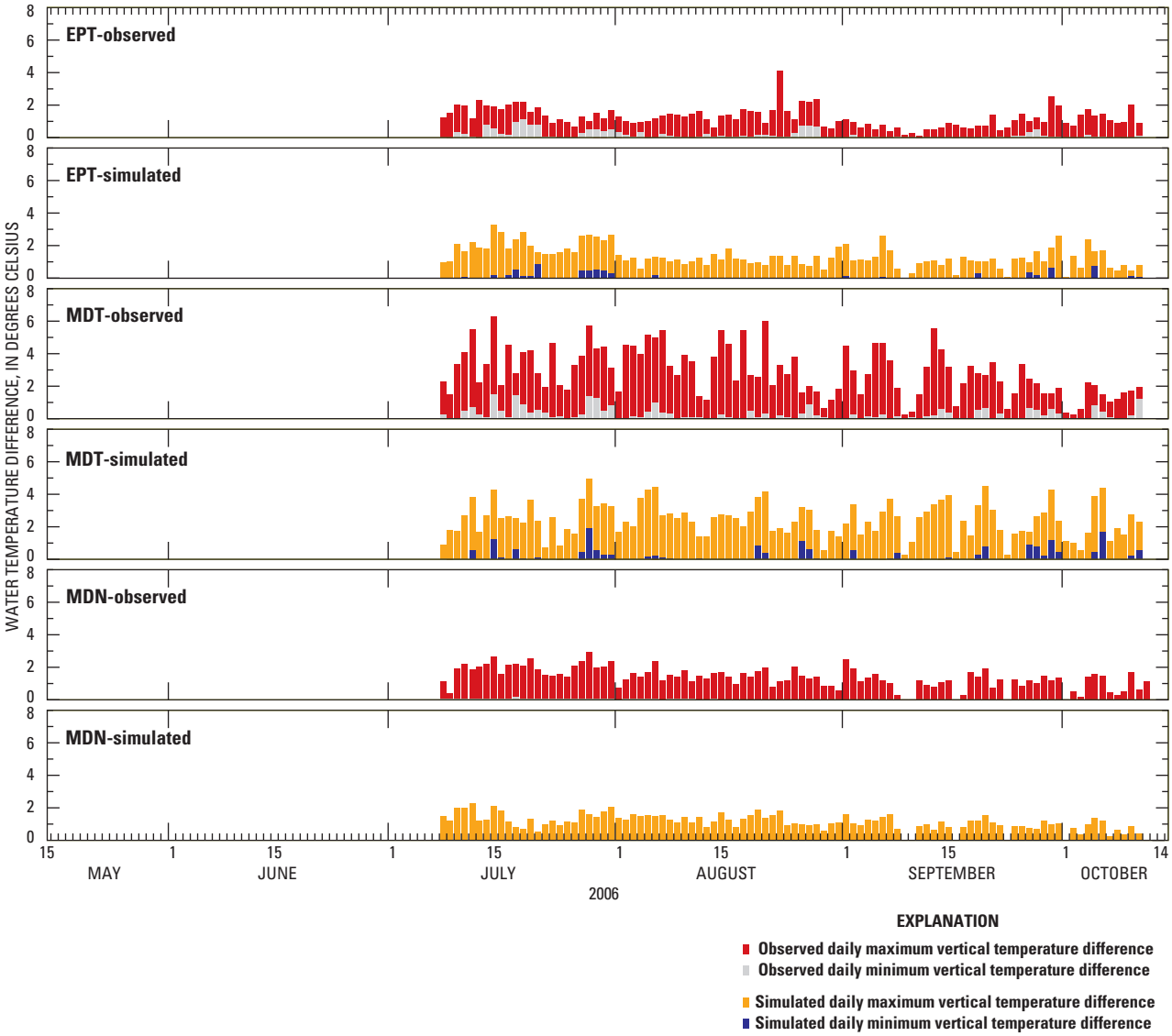

Figure 20. Daily maximum and minimum difference in temperature between near-surface and near-bottom of the water column at three deep sites in Upper Klamath Lake, Oregon, 2005.

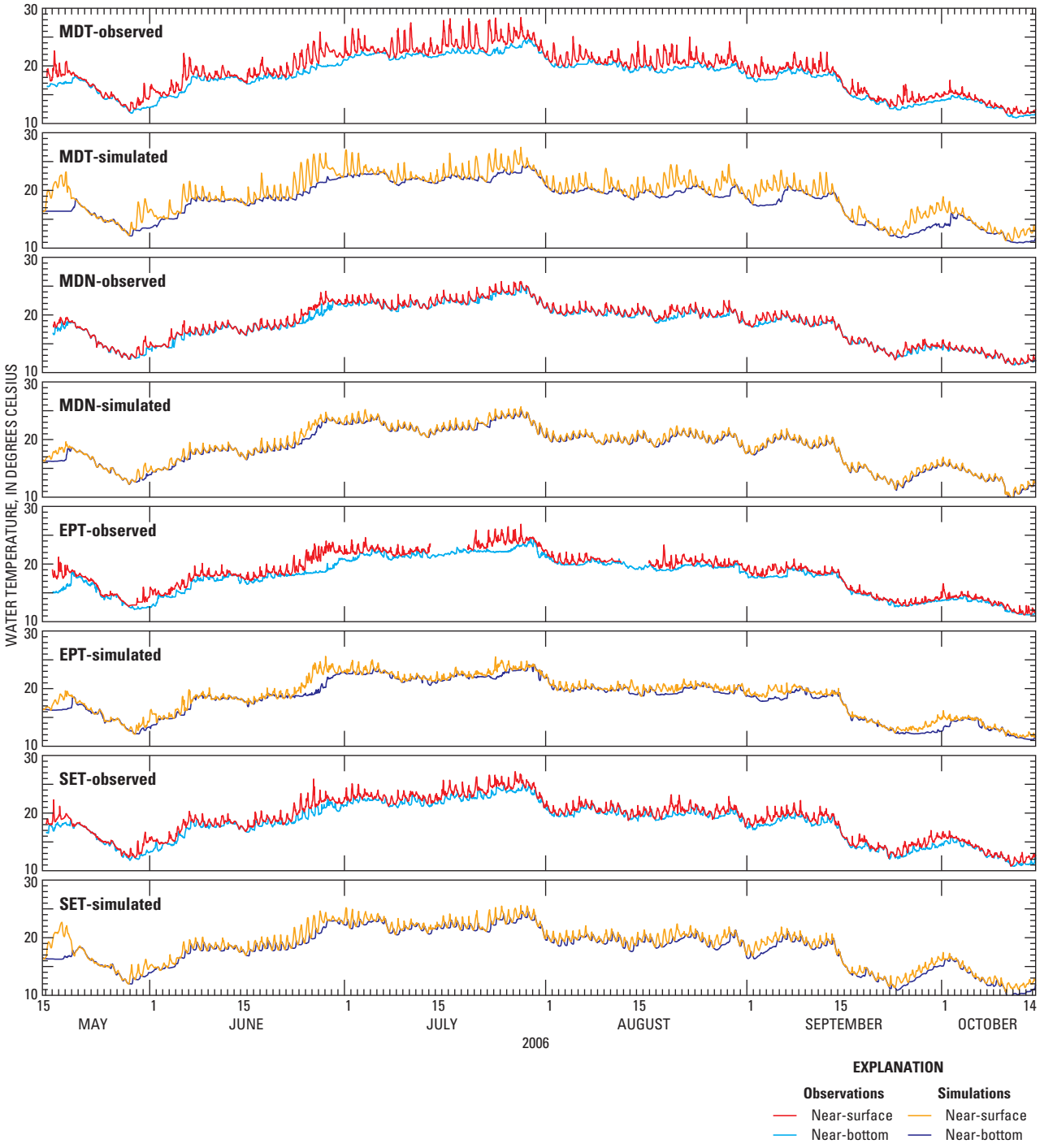

Figure 21. Observed and simulated temperatures at four deep sites in Upper Klamath Lake, Oregon, 2006.

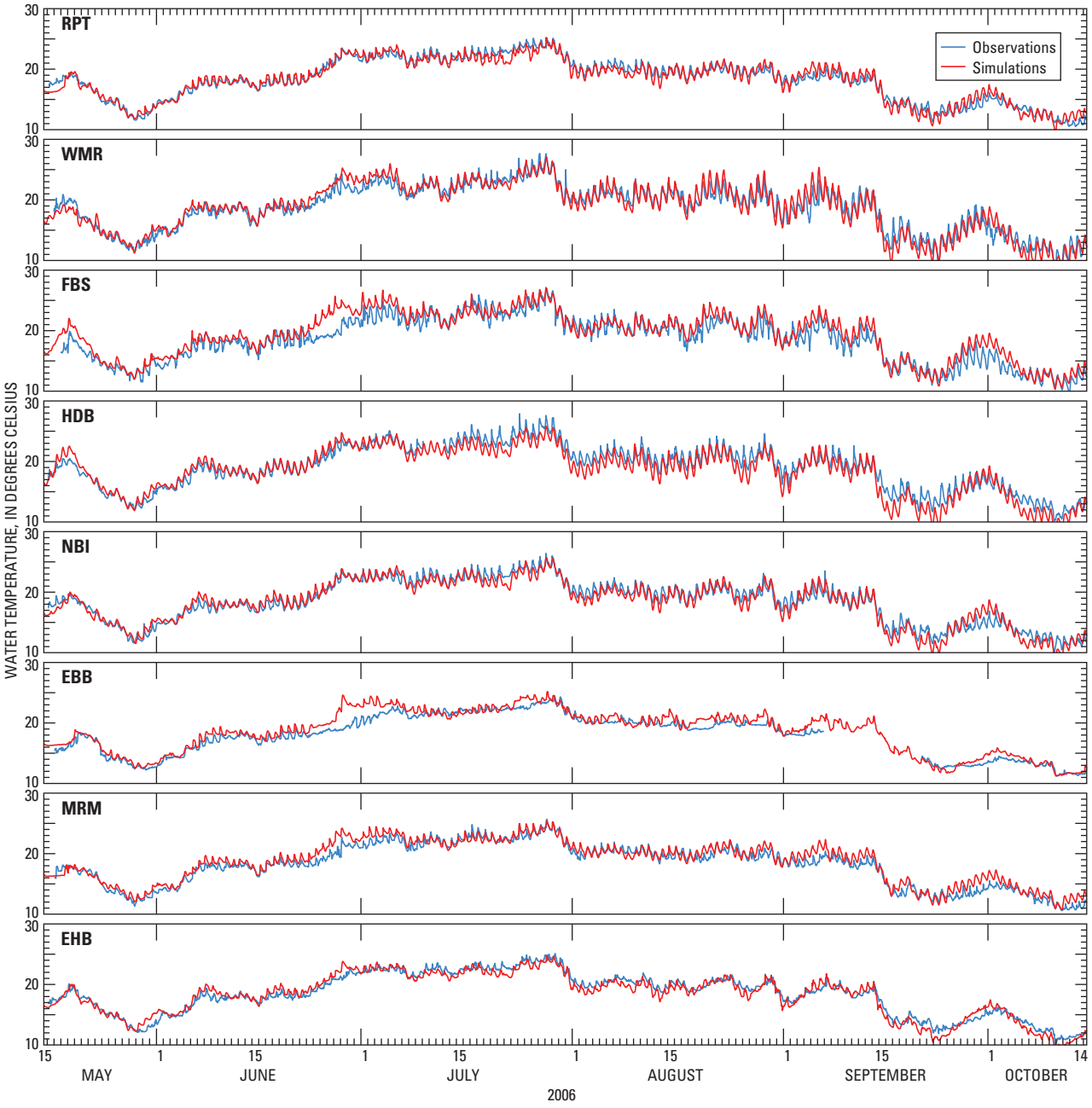

Figure 22. Observed and simulated temperatures at eight shallow sites in Upper Klamath Lake, Oregon, 2006.

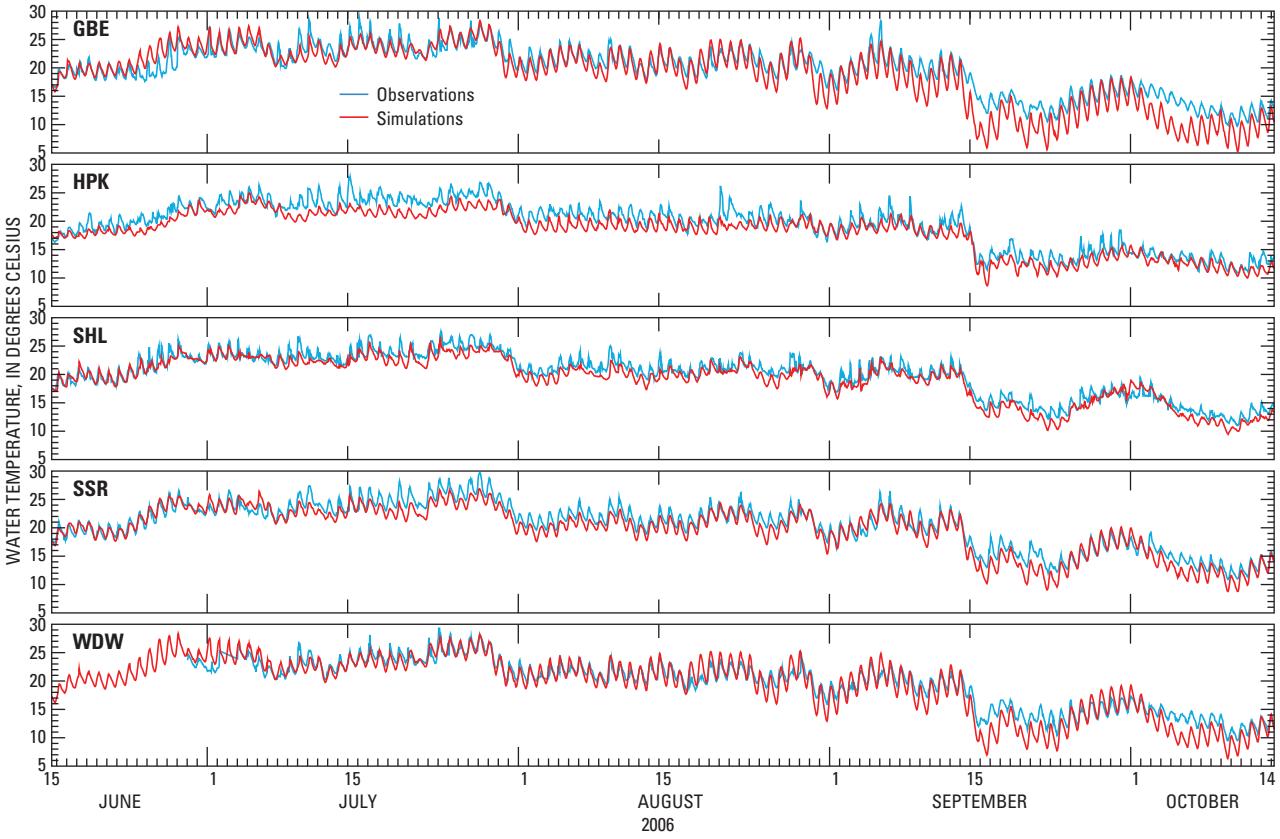

Figure 23. Observed and simulated temperatures at five nearshore sites in Upper Klamath Lake, Oregon, 2006.

Overall, the calibration of the model with 2005 temperature data and the validation with 2006 temperature data was satisfactory and adequate for the purpose of simulating the weekly to seasonal variations in temperature. The temperature is used in density calculations within the model and therefore determines the vertical mixing characteristics of the water column. The simulation of temperature captures both the daily thermal stability and those periods of time when the water column stratifies in deeper parts of the lake for several days at a time. Even though the lake is shallow, there has been discussion about the role that temporary stratification plays in water quality (Kann and Welch, 2005; Wood and others, 2006). Buoyant cyanobacteria like AFA are particularly suited to taking advantage of mild thermal stability to position colonies within the photic zone. In addition, as discussed further below, the tendency for the water column to stratify in the trench may provide a mechanism, particularly during a rapid bloom decline, for concentrating rising AFA colonies in the central part of the lake.

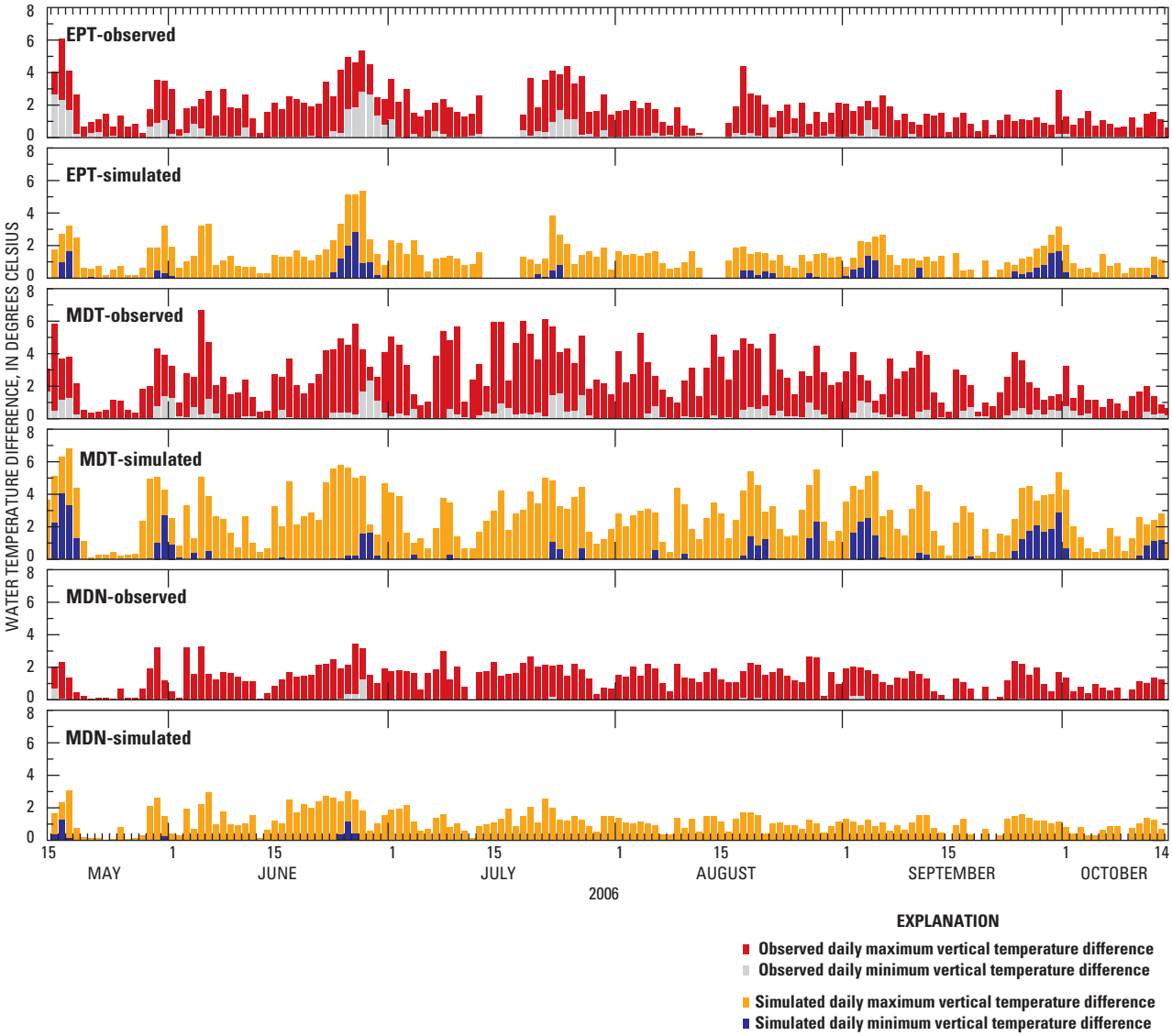

Figure 24. Daily maximum and minimum difference in temperature between near-surface and near-bottom of the water column at three deep sites in Upper Klamath Lake, Oregon, 2006.

Implications for Water Quality

Because severe water-quality problems in UKL are detrimental to the survival of endangered suckers, the hydrodynamic model is particularly useful insofar as it can provide insight into the processes that control water quality. The simulations of hydrodynamics and heat transport in 2005 and 2006 result in the following observations that have important implications for water quality: first, that water moving northward through the trench to the west of Bare Island is routed both to the north and to the south of the lake, and second, that the water originating from deeper in the trench is routed preferentially toward the north, while the water from nearer the surface is routed preferentially toward the south.

These observations were illustrated and quantified by using model simulations of conservative tracers that were designed to demonstrate how water from the trench is transported to the rest of the lake. First, the polygons in the numerical grid east of Eagle Ridge and south of Bare Island that were deeper than 4.5 m were identified (fig. 25). Within those polygons, and within layers deeper than 4.5 m, the concentration of tracer T1 was set to 1 (arbitrary units) at every time step, and within those layers shallower than 4.5 m the concentration of tracer T1 was set to 0 at every time step. Within the same polygons, and within layers deeper than 4.5 m, the concentration of tracer T2 was set to 0 at every time step, and within layers shallower than 4.5 m the concentration of tracer T2 was set to 1 at every time step. Within polygons outside of those identified, the initial concentrations of T1 and T2 were set to 0. Thus, the concentration of T1 and T2 at any point in the grid is a measure of the fraction of water at that point that originated in the trench at depths deeper than 4.5 m and shallower than 4.5 m, respectively. Assigning the concentrations of two distinct tracers in this way allowed tracking of the surface water of the trench separately from the deeper water. The tracer experiments began on August 1, 2005, and used the calibrated hydrodynamic and heat-transport model described above. The concentrations in the trench were assigned continuously, rather than as an initial condition at a single point in time, in order to observe the continuous transport of water through the trench and out into the lake for several days; as a result the total mass of each tracer increases throughout the simulation. For that reason, the simulations are most interesting over the first few days and were stopped after 10 days.

"Snapshots" of the concentration of tracers T1 and T2 in the surface layer of the grid at the end of day 5 are shown in figure 26. The snapshots show that water that exits the trench at the west of Bare Island (fig. 1) flows both to the east around the island and to the west into the northern part of the lake. The bifurcation of the flow at Eagle Point results in the development of two different circulation patterns, the longer

Figure 25. The location of polygons in the numerical grid where the depth was greater than 4.5 meters and where tracer concentrations were defined for numerical experiments.

of which carries water around the northern end of the lake and down the eastern shoreline, then turns around north of Buck Island. This circulation pattern is responsible for the direct influence of the water exiting the trench on water quality in the northern part of the lake. A second, shorter circulation pattern carries water around the north and east sides of Bare Island and turns around north of Howard Bay. Previous numerical experiments with this model have shown that the relative strengths of these two circulation patterns varies with the strength of the wind forcing, such that a stronger prevailing wind is more effective at pushing water into the northern part of the lake and enhances the larger pattern at the expense of the smaller (Wood and Cheng, 2006).

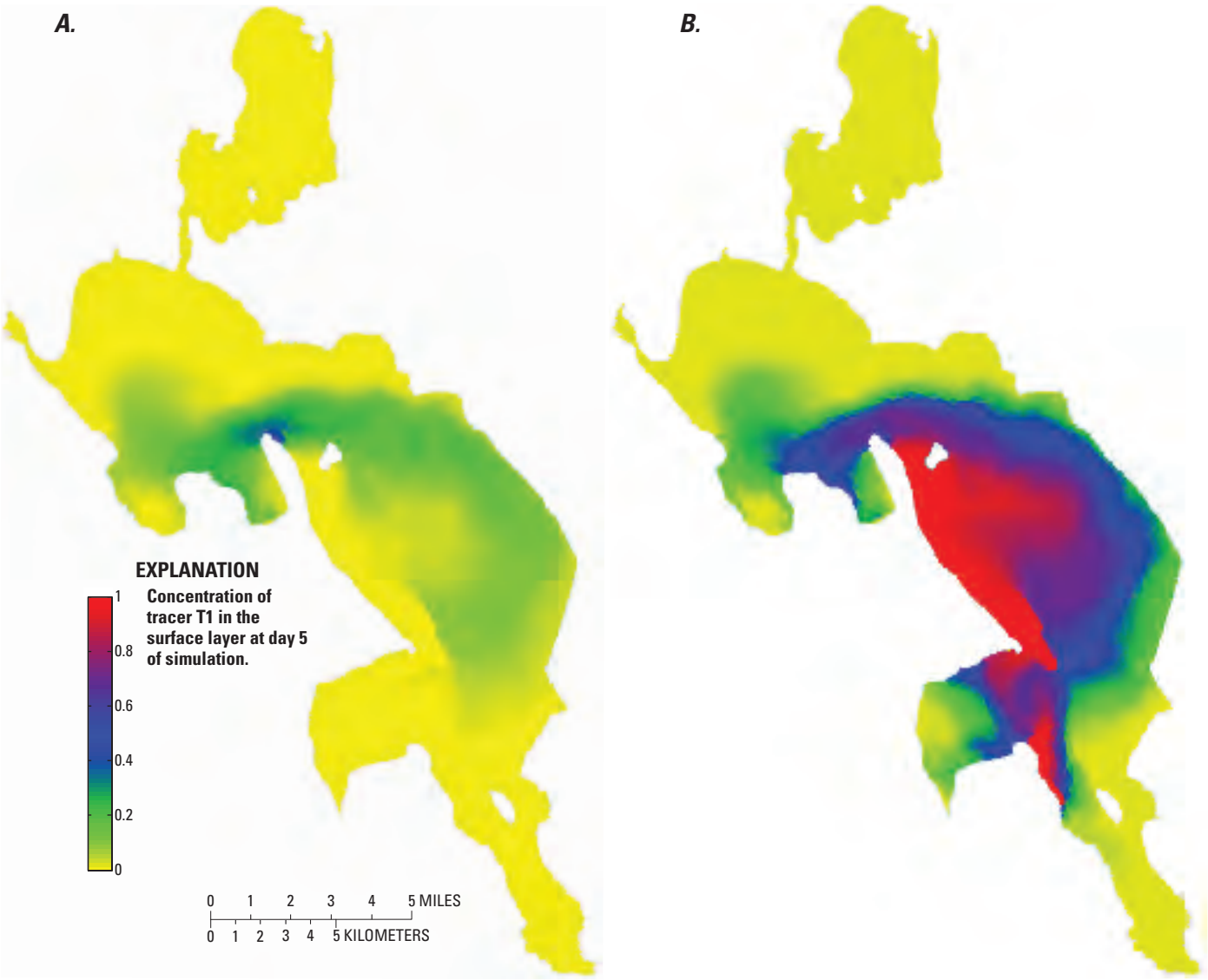

Figure 26. Concentration of tracers (*A*) T1 and (*B*) T2 in the surface layer of Upper Klamath Lake, Oregon, at day 5 of numerical experiments starting on August 1, 2005.

Consideration of the sum of the concentration of the two tracers together allows some quantification of the first observation provided above. The sum of concentrations of tracers T1 and T2 shows that water leaving the trench at the beginning of the simulation is detected at site MDN, centrally located in the northern part of the lake, in about 3 days, and the fraction of the water at site MDN that can be traced back to the trench increases rapidly over 7 days to a total of about 60 percent (fig. 27*A*). The concentrations were simulated in the middle of the water column, but there is little top-to-bottom difference in the simulated tracer concentration at either site MDN or MDL. At site MDL, located in the central part of the lake, the influence of the trench can be detected sooner, within about 1 day, and within 3 days the trench accounts for about 80 percent of the water at site MDL. Thus, it appears that the influence of the trench at site MDL through the shorter circulation pattern is both quicker and quantitatively larger than at site MDN. Note that these fractions of trench water and the travel time from the trench apply specifically to the wind conditions that were measured during the period of the simulation, from August 1 to 10, 2005, when the winds were weak to moderate and with no major reversals in direction; relative fractions of trench water and travel times would be expected to change with different wind conditions (Wood and Cheng, 2006). Although the relative strength of the shorter and longer circulation loops varies with wind conditions, the observation that water moving northward through the trench to the west of Bare Island is routed both to the north and to the south of the lake is robust under conditions of prevailing winds.

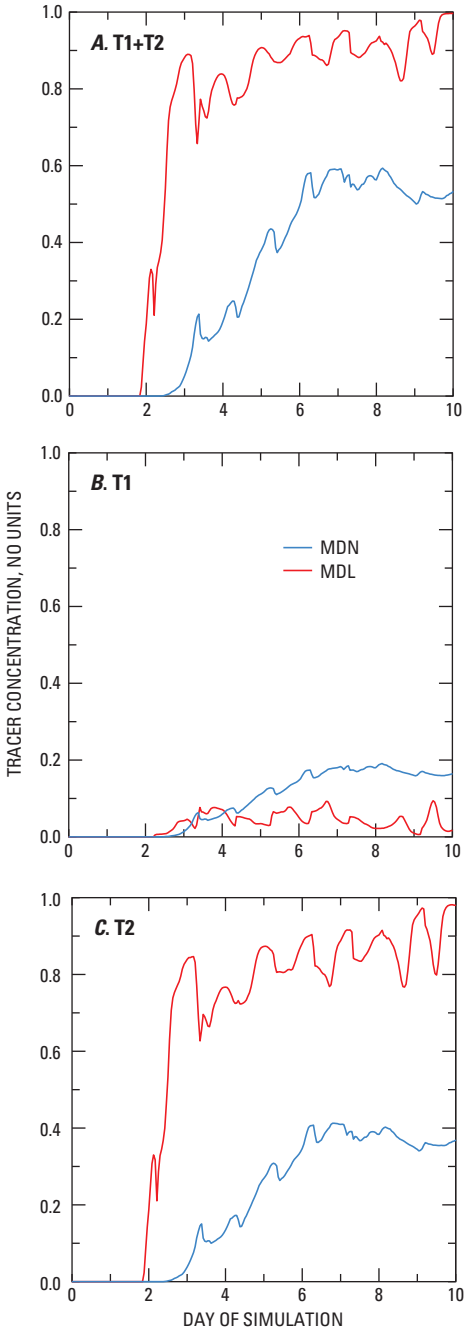

Figure 27. Time series of the simulated concentration of tracers T1 and T2 during 10 days of numerical experiments starting on August 1, 2005, at sites MDN and MDL in Upper Klamath Lake, Oregon. The total fraction of trench water at each site is represented by the sum of (*A*) T1 and T2, the fraction of water originating from depths greater than 4.5 m in the trench is represented by (*B*) T1, and the fraction of water originating from depths less than 4.5 m in the trench is represented by (*C*) T2.

The second observation, that the water originating from deeper in the trench is routed preferentially toward the north, while the water from nearer the surface is routed preferentially toward the south, is quantified by considering the difference in the time series of tracers T1 and T2 at the two sites. When the flow through the trench west of Bare Island splits into two different pathways, more of the surface water flows to the east around the north side of Bare Island, and more of the bottom water flows to the west into the northern part of the lake. Thus, while the overall influence of the trench at site MDN is less than that at site MDL, the influence of water from below 4.5 m is less at site MDL (fluctuating between about 0 and 10 percent during days 5–10 of the simulation) than at site MDN (fluctuating between about 10 and 20 percent during days 5–10 of the simulation; fig. 27*B*). Similarly, the influence of water from above 4.5 m is less at site MDN (fluctuating between about 30 and 40 percent during days 5–10 of the simulation) than at site MDL (fluctuating between about 90 and 100 percent during days 5–10 of the simulation; fig. 27*C*).

The trench plays a significant role in the overall oxygen budget of UKL, a conclusion supported by at least two separate datasets. First, light and dark bottle experiments have shown that the trench (site MDT) is characterized by net oxygen consumption, whereas much of the rest of the lake is characterized by net oxygen production (fig. 28, Appendix A). The data shown in figure 28 were collected between May and September of 2006; the methods used are discussed in Hoilman and others (2008). Second, oxygen isotopes of the dissolved oxygen in the lake are consistent with respiratory processes dominating in the trench and with domination by photosynthetic production away from the trench (S.R. Silva, U.S. Geological Survey, unpub. data, 2007). In addition, dissolved oxygen measurements from continuous monitors show that the lowest dissolved oxygen events in the northern part of the lake are not restricted to that part of the lake, but consistently are concurrent with very low dissolved oxygen concentrations in the trench as well (Wood and others 2006, Hoilman and others, 2008). Of particular interest is the influence the trench has on dissolved oxygen concentrations in the prime adult sucker habitat in the northern part of the lake, to the north and west of Eagle Point (Wood and others, 2006).

Observations from continuous monitors in 2005 show that the low dissolved oxygen concentrations that accompanied the annual bloom decline at the end of July 2005 were more severe in the northern part of the lake, as measured at site MDN, and were closer to the concentrations (particularly the near-bottom concentrations) detected in the trench at site MDT, than the concentrations in the southern part of the lake, as measured at site MDL (fig. 29). This is consistent with the numerical tracer experiments that demonstrate a greater influence of the near-bottom water in the trench at site MDN than at site MDL and less influence of the surface water.

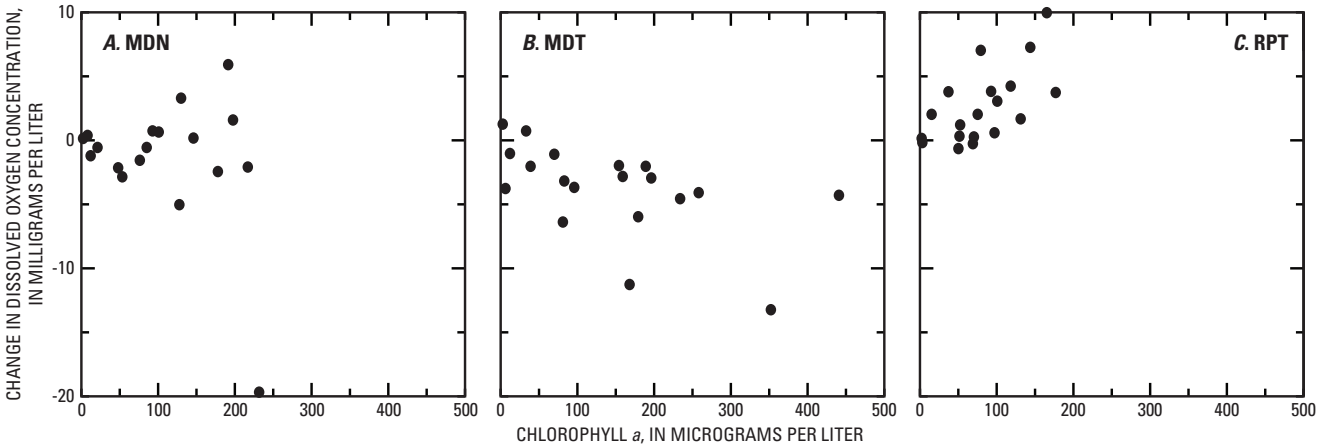

Figure 28. The 24-hour change in dissolved oxygen concentration that would result from the oxygen production and consumption rates measured in light and dark bottle incubations at sites (*A*) MDN, (*B*) MDT, and (*C*) RPT, in Upper Klamath Lake, Oregon, between June and October, 2006, as a function of the chlorophyll *a* concentration measured at the same site on the same date. The 24-hour change in dissolved oxygen concentration was calculated at each site as described in Appendix A.

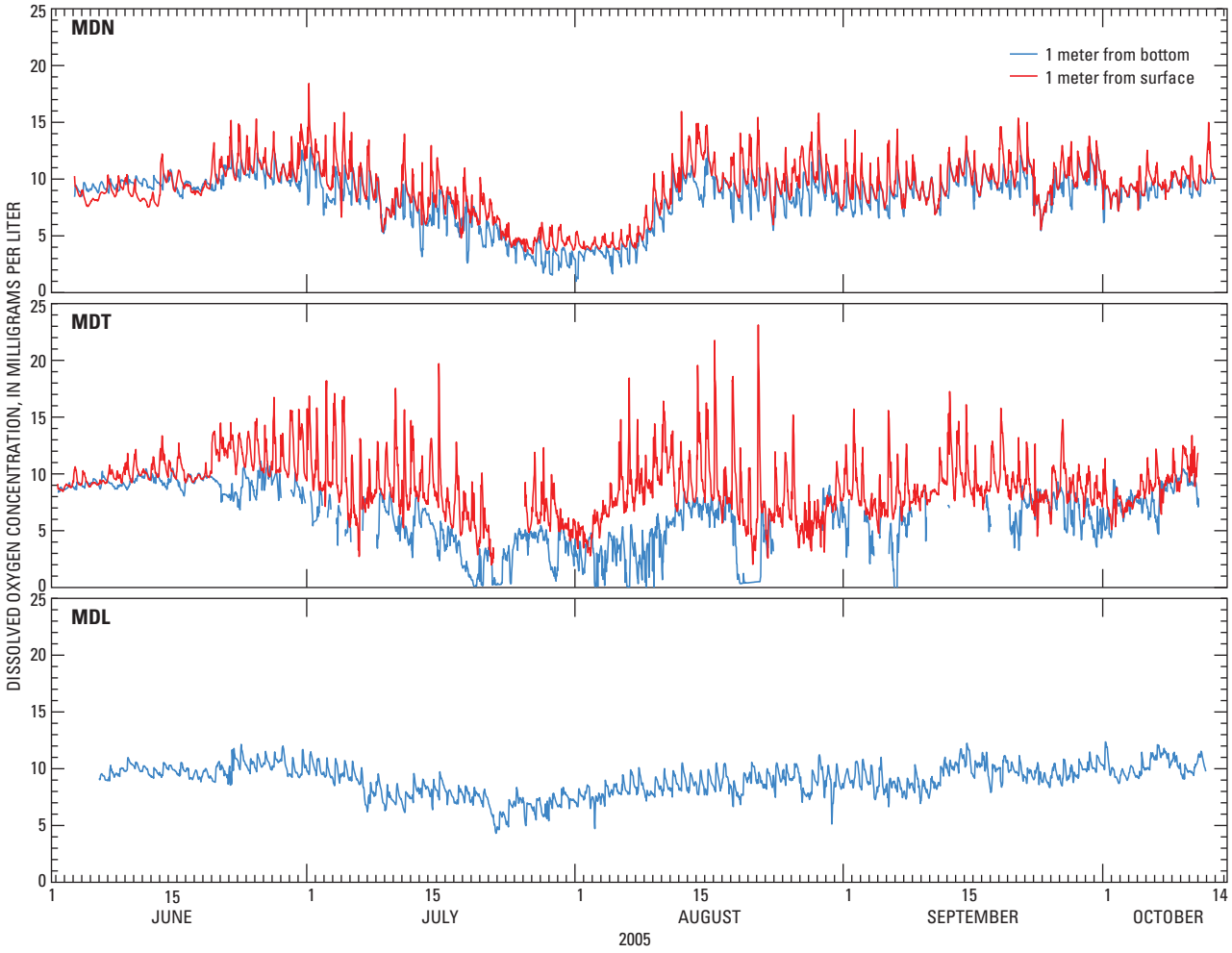

Figure 29. Time series of dissolved oxygen concentration data collected at sites MDN, MDT, and MDL in Upper Klamath Lake, Oregon, 2005.

The implications are twofold. First, the near-bottom water has a lower dissolved oxygen concentration than the near-surface water. Dissolved oxygen is not a conservative quantity, however, and given that water at site MDT has several days of travel time to reach either site MDN or site MDL, the differing influence of water from the bottom of the trench on these sites does not fully explain why such different concentrations were measured by the continuous monitors at these sites. Another possibility is that as water passes through the trench, the surface and bottom of the water column develop different capacities for replacement of the oxygen consumed in the trench once the water exits, as discussed below.

Vertical velocities measured by the current profiler at site ADCP1 in 2005 showed that at this site, but not at others, there was a clear distinction between the upper water column, where the AFA population was dominated by rising colonies, and the lower water column, where sinking colonies dominated the population (fig. 30; Gartner and others, 2007). The velocities measured by the ADCP are not water velocities, but rather the velocities of particles suspended in the water column. Vertical water velocities are expected to be one to two orders of magnitude lower than the vertical velocities measured by the ADCP. This suggests that under certain circumstances the effect of the two different circulation patterns is to concentrate rising colonies in the area between Bare Island and Howard Bay, and toward the western shoreline, and to send water relatively depleted of colonies (because they settled out in the trench), or dominated by sinking colonies, into the northern part of the lake. This may imply a greater capacity for photosynthetic production, on a per volume basis, in the central part of the lake between Bare Island and Howard Bay than in the northern part of the lake. Photosynthetic production of oxygen is a dominant term in the oxygen budget and dominates high respiratory and other consumptive demands over much of the lake. In the trench the opposite is true—consumption dominates production. If the water exiting the trench to the west around Eagle Point loses much of its capacity for photosynthetic production for at least a period of several days, while water column oxygen demands remain high, then the dissolved oxygen in the northern part of the lake, in the upper lobe of the larger clockwise circulation pattern, will be replenished more slowly than in the central part of the lake. This would be consistent with the bottle incubation experiments that showed that site RPT (like site MDL, located in the southern part of the lake) was consistently a site of net production of dissolved oxygen, whereas the results at site MDN were variable (fig. 28). Further development and testing of this hypothesis, both with numerical modeling and field work designed to better understand the physiology of the AFA blooms, is needed.

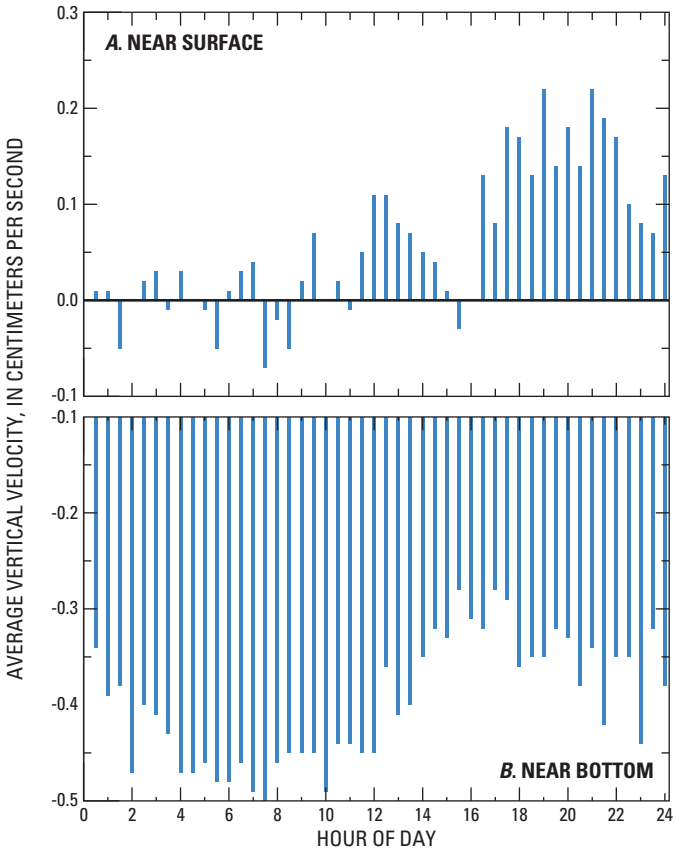

Figure 30. Average hourly vertical velocities at site ADCP1 (*A*) near surface and (*B*) near bottom, as measured by an Acoustic Doppler Current Profiler (ADCP), Upper Klamath Lake, Oregon. Velocities were averaged between June 21 and September 12, 2005.

Acknowledgments

The authors thank Jerad Bales, Annett Sullivan, and Chauncey Anderson for their detailed and thoughtful reviews of the manuscript, which greatly improved the report. Discussions with Michael MacWilliams and Kutay Celebioglu also were very helpful.

Summary

Upper Klamath Lake (UKL) is a hypereutrophic lake that experiences annual blooms of the buoyant cyanobacterium *Aphanizomenon flos aquae*. The severe water-quality conditions associated with these annual blooms (high pH, supersaturated to undersaturated dissolved oxygen, high un-ionized ammonia) are detrimental to the survival of two species of endangered suckers in the lake. As part of an ongoing and multipronged effort to understand the ecosystem of the lake, the U.S. Geological Survey and the Bureau of Reclamation entered into a cooperative agreement to develop a three-dimensional numerical model of the hydrodynamics and heat transport in the lake.

The model is built on the UnTRIM computational core. The important features of this model include a semi-implicit finite difference solution method for the governing equations, flexibility in the use of the hydrostatic assumption, the use of a mass-conserving scheme to solve the constituent transport equation that also ensures that the solution is bounded by the initial and boundary conditions, and the use of a flux limiter in the solution of the transport equation to preserve accuracy while relaxing the stability constraint on the size of the polygons in the numerical grid. UnTRIM solves the governing equations on an unstructured orthogonal grid. The advantage of this type of grid is that it allows the size of the polygons that make up the grid to vary over the domain according to the requirements of the bathymetry and geometry, and allows for a shoreline-fitting boundary. The solution schemes used to solve the governing equations within the model provide a robust, stable, and computationally efficient platform on which to develop the UKL model.

Source and sink terms to calculate surface heat fluxes were added to the UnTRIM computational core. These include incoming shortwave radiation, atmospheric longwave radiation, reflected longwave radiation, evaporative cooling, and conduction. Two additional enhancements were made to the computational core. The first was a submodel designed to estimate a spatially variable surface wind based on mass-conserving interpolation. The second was a two-equation turbulence closure model designed to calculate spatially and temporally varying vertical diffusivities as a function of turbulent kinetic energy and its rate of dissipation.

The hydrodynamic model was calibrated for June through September 2005 by using two parameters to adjust surface and bottom shear stress. Two different spatially uniform surface winds were used to run the model from either June or July through August—one measured in the northern part of the lake and one measured in the central part of the lake. The model also was run using a spatially variable surface wind from August through September. The spatially variable surface wind was generated from the variable-wind submodel using wind data collected at two sites on the lake and four around the shoreline. Simulations resulting from all three surface winds could be compared during the midsummer overlap period. Datasets that were used to evaluate model simulations during the calibration process included surface elevation determined by 3 gages around the lake, currents measured by Acoustic Doppler Current Profilers (ADCPs) at 5 sites in the lake, and temperature measured at 14 sites by continuous monitors.

The model predicted wind-driven circulation patterns in the lake that reproduced the prevailing currents measured by ADCPs—a clockwise circulation consisting of broad, shallow flow with the wind (to the south-southeast) on the eastern side of the lake, and a narrow band of flow opposing the wind (to the north-northwest) through the deep trench along the western shoreline and passing to the west of Bare Island. The model simulations interpolate currents between the ADCP measurements sites; they reveal that under prevailing wind conditions there are two predominant modes to this circulation. The first is a smaller gyre that circulates water between Bare Island and Rattlesnake Point; the second is a larger gyre that circulates water between Rattlesnake Point and the northernmost part of UKL.

In order to evaluate the performance of the model, the mean error (ME) and root mean squared error (RMSE) of the hourly measured and simulated currents and temperature were calculated. In the process of model calibration with data collected during June to September of 2005, emphasis was placed on correctly simulating the highest velocities through the trench. The ME and RMSE of the VW simulation (calculated over 37 days between July 26 and August 31) in the depth-averaged speed at site ADCP1 (located in the middle of the trench) were small (0.50 and 3.08 centimeters per second (cm/s), respectively) in comparison to the mean of the depth-averaged speed at that site over the same period (11.23 cm/s). The simulated depth-averaged speed at two sites that were located in the northern part of the lake where velocities were lower were biased low, as indicated by a larger, positive ME of 0.80 cm/s at site ADCP3 (mean depth-averaged speed 4.09 cm/s) and 2.58 cm/s at site ADCP5 (mean depth-averaged speed 5.81 cm/s). Consideration of the velocity components near the surface and near the bottom showed that the goodness-of-fit errors were higher near the surface than near the bottom, indicating that the model may have difficulty in correctly simulating the surface boundary layer, particularly in those areas of the lake where the depth-averaged currents oppose the prevailing wind stress. The use of a spatially variable wind forcing that was interpolated between two meteorological sites on the lake and four on the shoreline generally resulted in improved error statistics. The improvement obtained by using the spatially variable

surface wind was particularly evident upon closer inspection of the individual velocity components at a site in the northern part of the lake. At this site (ADCP3), the spatially variable surface wind correctly simulated the diel phase shift between the bottom and surface currents, whereas the uniform surface wind did not. In the process of comparing results among the spatially variable surface wind simulation and the two uniform surface wind simulations, it was demonstrated that, if a uniform wind must be used, the measurement should be made in the central part of the lake rather than in the northern part. In interpreting any of these results it is useful to remember that there is some inherent accuracy limitation to the ADCP measurements, and that accuracy may be a function of distance from the ADCP (in other words, near-bottom measurements may be somewhat more accurate than near-surface measurements).

The calibration of the heat transport was accomplished by adjusting one calibration parameter that specified the amount of incoming shortwave radiation reflected at the water surface. The error statistics indicated a small, high bias in the simulated temperatures over the lake, as the ME calculated between July 26 and August 31 at all the sites was more often negative than positive, although it was less than 1 degree Celsius (°C) at all sites, ranging from –0.94 to 0.73°C when a spatially variable surface wind was used. The RMSE was less than 1°C at all but one site and ranged from 0.40 to 1.12°C when a spatially variable surface wind was used. The model accurately reproduced thermal stability in the water column on a daily basis, and also correctly identified those periods when the stratification was maintained for several days.

The model validation simulations spanned 123 days between May 15 and October 15, 2006. Those simulations used a spatially variable surface wind and the same calibration parameters as established for 2005. Fewer ADCP velocity records were available to verify the model in 2006 (two sites), but one of these was site ADCP1, a site located in the deep trench where an ADCP also was deployed in 2005. This provided the opportunity to directly compare the performance of the model at this site for a comparable period, roughly the month of August, in both years. The ME and RMSE of the depth-averaged speed at this site, where the mean depth-averaged speed was 12.98 cm/s in 2006, were 2.30 and 3.88 cm/s, compared to 0.50 and 3.08 in 2005, so the model did not perform as well in 2006. The larger positive ME indicates that the velocities in the trench were underestimated; model calibration may not be optimized for multiple years. A second ADCP site in 2006 was located in an area of very low velocities (mean depth-averaged speed 3.42 cm/s) in the northern part of the lake. This site was farther from the trench and the main circulation gyre than the two sites where ADCPs were placed in the northern part of the lake in 2005; the accuracy of water currents simulated at this site was poor. The error statistics showed that most of the error was in the surface currents, as might be expected because the measured velocities at this site largely opposed the prevailing wind stress.

The results of the hydrodynamic and heat transport model for water quality in the lake indicate first, that water moving northward through the trench to the west of Bare Island is routed both to the north and to the south of the lake, and second, that the water originating from deeper in the trench is routed preferentially toward the north, while the water from nearer the surface is routed preferentially toward the south. Numerical tracer experiments were used to illustrate and quantify these observations. These tracer experiments are specific to the wind conditions, which were weak to moderate, during the dates of the simulation—from August 1 to 10, 2005. The experiments showed that 10 percent or less of the water passing through site MDL, in the southern part of the lake, originated from depths greater than 4.5 meters in the trench within the previous 5 days, whereas as much as 20 percent of the water at site MDN, in the northern part of the lake, originated from there. Similarly, the amount of water passing through site MDL that originated from depths shallower than 4.5 meters in the trench was between 90 and 100 percent, whereas only about 40 percent of the water passing through site MDN originated from there. These percentages were obtained for the specific conditions of early August 2005 and therefore may not be appropriate for other conditions. However, the more qualitative observation that surface water is circulated very effectively from the trench through the central part of the lake between Bare Island and Rattlesnake Point is robust and generally applicable, as is the observation that much less of the surface water but most of the deeper water in the trench moves instead toward the northern part of the lake. This means that during severe low dissolved oxygen events, most of the deeper water with a very low dissolved oxygen concentration moves into the prime adult sucker habitat in the northern part of the lake.

Given that dissolved oxygen is not conservative and that travel times are several days, this does not entirely explain why dissolved oxygen concentrations tend to be much lower and closer to concentrations in the trench during these events in the northern part of the lake than in the central part of the lake. Some difference in the capacity to replenish dissolved oxygen concentration between surface and deep water also is implied. Vertical velocities collected at site ADCP1 suggest that the trench is deep enough to effectively separate rising and sinking *Aphanizomenon flos aquae* (AFA) colonies. In conjunction with the two circulation gyres, this may provide a mechanism to concentrate healthier, rising AFA colonies in the central part of the lake, while at the same time causing the northern part of the lake to become relatively depleted of AFA colonies capable of photosynthetic oxygen production. This hypothesis could help explain why the water-quality conditions associated with rapid AFA bloom declines are more severe in the northern part of the lake, but further testing of this idea is required.

References Cited

Adams, B., Swigle, B., and Shively, R., 2003, Movements and behavior of radio-tagged adult Lost River and shortnose suckers with respect to water quality in Upper Klamath Lake: U.S. Geological Survey Draft Annual Report of research to the U.S. Bureau of Reclamation, Mid-Pacific Region, Klamath Area Office, Klamath Falls, Oregon.

Bowen, I.S., 1926, The ratio of heat losses by conduction and by evaporation from any water surface: Physics Review, v. 27, p. 779–787.

Bowie, G.L., Mills, W.B., Porcella, D.B., Campbell, C.L., Pagenkopf, J.R., Rupp, G.L., Johnson, K.M., Chan, P.W.H., Gherini, S.A., and Chamberlin, C.E., 1985, Rates, constants, and kinetics formulations in surface water quality modeling (Second edition): U.S. Environmental Protection Agency, EPA/600/3–85/040, 455 p.

Bradbury, J.P., Colman, S.M., and Dean, W.E., 2004, Limnological and climatic environments at Upper Klamath Lake, Oregon during the past 45,000 years: Journal of Paleolimnology, v. 31, no. 2, p. 167–188.

Bradbury, J.P., Colman, S.M., and Reynolds, R.L., 2004, The history of recent limnologic changes and human impact on Upper Klamath Lake, Oregon: Journal of Paleolimnology, v. 31, p. 151–165.

Bureau of Reclamation, 2008, Pacific Northwest Cooperative Agricultural Weather Network, accessed April 17, 2008, at http://www.usbr.gov/pn/agrimet/wxdata.html

Casulli, Vincenzo, 1990, Semi-implicit finite-difference methods for the two-dimensional shallow water equations: Journal of Computational Physics, v. 86, p. 56–74.

Casulli, Vincenzo, 1999a, A semi-implicit finite difference method for non-hydrostatic, free-surface flows: International Journal for Numerical Methods in Fluids, v. 30, p. 425–440.

Casulli, Vincenzo, 1999b, A semi-implicit numerical method for non-hydrostatic free surface flows on unstructured grid, *in* Proceedings of the International Workshop on Numerical Modelling of Hydrodynamic Systems, Zaragoza, Spain, 1999: Zaragoza, Spain, University of Zaragoza, p. 175–193.

Casulli, Vincenzo, and Cattani, E., 1994, Stability, accuracy and efficiency of a semi-implicit method for three-dimensional shallow water flow: Computers & Mathematics with Applications, v. 27, p. 99–112.

Casulli, Vincenzo, and Cheng, R.T., 1992, Semi-implicit finite difference methods for three-dimensional shallow water flow: International Journal for Numerical Methods in Fluids, v. 15, p. 629–648.

Casulli, Vincenzo, and Walters, R.A., 2000, An unstructured grid, three-dimensional model based on the shallow water equations: International Journal for Numerical Methods in Fluids, v. 32, p. 331–348.

Casulli, Vincenzo, and Zanolli, P., 1998, A three-dimensional semi-implicit algorithm for environmental flows on unstructured grids, *in* Baines, M.J., Proceedings of the Conference On Numerical Methods for Fluid Dynamics, Oxford, England, 1998: Oxford, England, University of Oxford, p. 57-70.

Casulli, Vincenzo, and Zanolli, P., 2002, Semi-implicit numerical modeling of nonhydrostatic free-surface flows for environmental problems: Mathematical and Computer Modelling, v. 36, p. 1131–1149.

Casulli, Vincenzo, and Zanolli, P., 2005, High resolution methods for multidimensional advection–diffusion problems in free-surface hydrodynamics: Ocean Modelling, v. 10, p. 137–151.

Celebioglu, T.K., and Piasecki, M., 2006a, Comparison of turbulence models with use of UnTRIM in the Delaware Bay, *in* Proceedings of the Ninth International Conference on Estuarine and Coastal Modeling, Charleston, S.C., 2005: American Society of Civil Engineers, p. 105–122.

Celebioglu, T.K., and Piasecki, M., 2006b, Simulation of salinity and suspended sediment dynamics in Delaware Bay by comparing turbulence closure models, *in* Proceedings of the 7th International Conference on Hydroscience and Engineering (ICHE–2006), Philadelphia, Pennsylvania, 2006: Philadelphia, Drexel University, accessed April 30, 2008, at http://idea.library.drexel.edu/handle/1860/1482

Cheng, R.T., Gartner, J.W., and Wood, T.M., 2005, Modeling and validation of wind-driven circulation in Upper Klamath Lake, Oregon, *in* Walton, Raymond, ed., Proceedings of the 2005 World Water and Environmental Resources Congress: Anchorage, Alaska, Environmental and Water Resources Institute of American Society of Civil Engineers, accessed April 30, 2008, at http://scitation.aip.org/getabs/servlet/GetabsServlet?prog=normal&id=ASCECP00017304079200426000001&idtype=cvips&gifs=Yes

Colman, S.M., Bradbury, J.P., McGeehin, J.P., Holmes, C.W., Edginton, David, and Sarna-Wojcicki, A.M., 2004, Chronology of sediment deposition in Upper Klamath Lake, Oregon: Journal of Paleolimnology, v. 31, p. 139–149.

Colman, S.M., Bradbury, J.P., and Rosenbaum, J.G., 2004, Paleolimnology and paleoclimate studies in Upper Klamath Lake: Journal of Paleolimnology, v. 31, p. 129–138.

Dingman, S.L., 2002, Physical hydrology: Upper Saddle River, N.J., Prentice Hall, 646 p.

Eilers, J.M., Kann, Jacob, Cornett, J., Moser, K., and St. Amand, A., 2004, Paleolimnological evidence of change in a shallow, hypereutrophic lake: Upper Klamath Lake, Oregon, USA: Hydrobiologia, v. 520, p. 7–18.

Eilers, J.M., Kann, Jacob, Cornett, J., Moser, K., St. Amand, A., and Gubala, C., 2001, Recent paleolimnology of Upper Klamath Lake, Oregon: Roseburg, Oregon, J.C. Headwaters, Inc., Report submitted to the Bureau of Reclamation, 44 p.

Fisher, L.H., and Wood, T.M., 2004, Effect of water-column pH on sediment-phosphorus release rates in Upper Klamath Lake, Oregon, 2001: U.S. Geological Survey Water-Resources Investigations Report 03–4271, 25 p.

Garratt, J.R., 1977, Review of drag coefficients over oceans and continents: American Meteorological Society Monthly Weather Review, v. 105, p. 915–929.

Gartner, J.W., Wellman, R.E., Wood, T.M., and Cheng, R.T., 2007, Water velocity and suspended solids measurements by in-situ instruments in Upper Klamath Lake, Oregon: U.S. Geological Survey Open-File Report 2007–1279, 136 p. plus data files.

Gill, A.E., 1982, Atmosphere–ocean dynamics, International Geophysics Series, v. 30: New York, Academic Press, 662 p.

Golub, G.H., and van Loan, C.F., 1996, Matrix computations (3rd ed.): Baltimore, Johns Hopkins University Press, 728 p.

Herrett, T.A., Hess, G.W., Stewart, M.A., Ruppert, G.P., and Courts, M.L., 2006, Water resources data for Oregon, water year 2005: U.S. Geological Survey Water-Data Report OR–05–1, 942 p., accessed March 6, 2008, at http://pubs.usgs.gov/wdr/2005/wdr-or-05/

Hoilman, G.R., Lindenberg, M.K., and Wood, T.M., 2008, Water-quality conditions in Upper Klamath and Agency Lakes, Oregon, 2005: U.S. Geological Survey Scientific Investigations Report 2008–5026, 44 p., accessed April 30, 2008, at http://pubs.usgs.gov/sir/2008/5026/

Hubbard, L.H., 1970, Water budget of Upper Klamath Lake southwestern Oregon: U.S. Geological Survey Hydrologic Investigations Atlas HA–351.

Janssen, K.D., 2006, Daily energy-budget and Penman evaporation from Upper Klamath Lake, Oregon: Portland, Oregon, Portland State University, M.S. thesis.

Kann, Jacob, 1998, Ecology and water quality dynamics of a shallow hypereutrophic lake dominated by cyanobacteria (*Aphanizomenon flos aquae*): Chapel Hill, University of North Carolina, Ph.D. dissertation, 110 p.

Kann, Jacob, and Walker, W.W., 1999, Nutrient and hydrologic loading to Upper Klamath Lake, Oregon, 1991–1998: Klamath Falls, Oregon, Report to Klamath Tribes Natural Resources Department [variously paged].

Kann, Jacob, and Welch, E.B., 2005, Wind control on water quality in shallow, hypereutrophic Upper Klamath Lake, Oregon: Lake and Reservoir Management, v. 21, no. 2, p. 149–158.

Kantha, L.H., and Clayson, C.A., 1994, An improved mixed layer model for geophysical applications: Journal of Geophysical Research, v. 99, p. 25235–25266.

Lerman, Abraham, 1971, Time to chemical steady-states in lakes and oceans: Advances in Chemistry Series, v.106 , p. 30–76.

Lippert, C., and Sellerhoff, F., 2006, Efficient generation of orthogonal unstructured grids: Proceedings of the Seventh International Conference on Hydroscience and Engineering, Philadelphia, Pa., 2006: Philadelphia, Drexel University, accessed April 18, 2008, at http://idea.library.drexel.edu/handle/1860/1472

Ludwig, F.L., Livingston, J.M., and Endlich, R.M., 1991, Use of mass conservation and critical dividing streamline concepts for efficient objective analysis of winds in complex terrain: Journal of Applied Meteorology, v. 30, p. 1490–1499.

Martin, J.L., and McCutcheon, S.C., 1999, Hydrodynamics and transport for water quality modeling: Boca Raton, Florida, CRC Press, 794 p.

McCutcheon, S.C., 1989, Water quality modeling, *in* French, R.H., ed., Volume I, Transport and surface exchange in rivers: Boca Raton, Florida, CRC Press, 334 p.

Miller, W.E., and Tash, J.C., 1967, Interim report Upper Klamath Lake studies: Corvallis, Oregon, Federal Water Pollution Control Administration, Eutrophication Research Branch, Pacific Northwest Water Laboratory [variously paged].

Oregon Climate Service, 2008, Zone 3—Climate data archives, accessed September 17, 2007, at http://www.ocs.oregonstate.edu/page_links/climate_data_zones/monthly_airport/nmez3.html

Perkins, D., Kann, Jacob, and Scoppettone, G.G., 2000, The role of poor water quality and fish kills in the decline of endangered Lost River and shortnose suckers in Upper Klamath Lake: U.S. Geological Survey, Biological Resources Division Report submitted to U.S. Bureau of Reclamation, Klamath Falls Project Office, Klamath Falls, Oregon, Contract 4–AA–29–12160, 39 p.

Phinney, H.K., and Peek, C.A., 1960, Klamath Lake, an instance of natural enrichment, *in* Transactions of the Seminar on Algae and Metropolitan Wastes: Cincinnati, Ohio, U.S. Public Health Service, 6 p.

Rodi, Wolfgang, 1993, Turbulence models and their application in hydraulics: Rotterdam, A.A. Balkema publishers, International Association for Hydraulic Research Monograph Series, 116 p.

Roe, P.L., 1986, Characteristic-based schemes for the Euler equations: Annual Review of Fluid Mechanics, v. 18, p. 337–365.

Scheffer, Marten, 1998, Ecology of shallow lakes: London, Chapman and Hall, 357 p.

Schlichting, Hermann, 1955, Boundary-layer theory: New York, McGraw-Hill, 535 p.

Smith, S.D., and Banke, E.G., 1975, Variation of the sea surface drag coefficient with wind speed: Quarterly Journal of the Royal Meteorological Society, v. 101, p. 665–673.

Swinbank, W.C., 1963, Longwave radiation from clear skies: Quarterly Journal of the Royal Meteorological Society, v. 89, p. 339–348.

Umlauf, Lars, and Burchard, H., 2003, A generic length-scale equation for geophysical turbulence models: Journal of Marine Research, v. 61, p. 235–265.

U.S. Fish and Wildlife Service, 2001, Biological/Conference opinion regarding the effects of operation of the Bureau of Reclamation's Klamath Project on the endangered Lost River sucker, endangered shortnose sucker, threatened bald eagle, and proposed critical habitat for the Lost River/shortnose suckers: Klamath Falls, Oregon, U.S. Fish and Wildlife Service, 188 p.

U.S Geological Survey, 2007, Water-resources data for the United States, water year 2006: U.S. Geological Survey Water-Data Report WDR–US–2006, accessed March 6, 2008, at http://wdr.water.usgs.gov/wy2006/search.jsp

Walker, W.W., 2001, Development of a phosphorus TMDL for Upper Klamath Lake, Oregon: Concord, Massachusetts, Report prepared for Oregon Department of Environmental Quality, 80 p.

Warner, J.C., Sherwood, C.R., Arango, H.G., and Signell, R.P., 2005, Performance of four turbulence closure models implemented using a generic length scale method: Ocean Modeling, v. 8, p. 81–113.

Wood, T.M., and Cheng, R.T., 2006, Use of UnTRIM to investigate dissolved oxygen transport in Upper Klamath Lake, Oregon: Proceedings of the Seventh International Conference on Hydroscience and Engineering, Philadelphia, Pa., 2006: Philadelphia, Drexel University, accessed April 18, 2008, at http://idea.library.drexel.edu/handle/1860/1424

Wood, T.M., Hoilman, G.R., and Lindenberg, M.K., 2006, Water-quality conditions in Upper Klamath Lake, Oregon 2002–04: U.S. Geological Survey Scientific Investigations Report 2006–5209, 52 p.

Wu, J., 1969, Wind stress and surface roughness at air–sea interface: Journal of Geophysical Research, v. 74, p. 444–455.

Wuest, Alfred, and Lorke, Andreas, 2003, Small-scale hydrodynamics in lakes: Annual Review of Fluid Mechanics, v. 35, p. 373–412.

Wunderlich, W.O., 1972, Heat and mass transfer between a water surface and the atmosphere, TN Report 14: Norris, Tennessee, Tennessee Valley Authority Water Resources Research Engineering Laboratory.

Appendix A. Calculation of the Rate of Change in Dissolved Oxygen Over 24 Hours from Light/Dark Bottle Incubations and the Extinction Coefficient

An estimate of the potential change in dissolved oxygen over a 24-hour period (ΔDO) was made from the measured oxygen production and consumption rates in the light and dark bottles at two levels in the water column and the measured extinction coefficient as follows. The gross production G in mg L^{-1} hr^{-1} was assumed to have the same exponential dependence with depth as light radiation. Then, in analogy with equation (21), the gross production at any depth in the water column G_z as a function of the gross production at the water surface G_0 is given by

$$G_z = G_0 e^{-k_e z} \quad . \tag{A1}$$

Solving for G_0 in terms of the value obtained from 0.5 m depth yields

$$G_0 = G_{0.5} e^{0.5 k_e} \quad . \tag{A2}$$

The gross production integrated over a water column of depth D is given by

$$\bar{G} = G_0 \int_0^D e^{-k_e z} dz = \frac{G_0}{10^{-3} k_e} \left(1 - e^{-k_e D}\right) \ , \tag{A3}$$

where 10^{-3} is a proportionality constant. The units of $\bar{G}$ are mg m^{-2} hr^{-1}.

Measured respiration rates (R) were very similar at both depths, and are therefore assumed to be constant throughout the water column for this calculation. Then the respiration integrated over the water column is given by

$$\bar{R} = \frac{RD}{10^{-3}} \quad . \tag{A4}$$

where 10^{-3} is a proportionality constant and the units of $\bar{R}$ are mg m^{-2} hr^{-1}. The final simplification is to assume that the gross production rate is constant at $\bar{G}$ for 12 hours of daylight in every 24 hours and zero for the remaining 12 hours, and the respiration rate is constant for a full 24 hours. Then the estimated change in dissolved oxygen over a 24-hour period, expressed in terms of a concentration (mg L^{-1}), is

$$\Delta DO = (12\bar{G} + 24\bar{R}) \frac{10^{-3}}{D} = \frac{12 G_0}{k_e D} \left(1 - e^{-k_e D}\right) + 24R \quad . \tag{A5}$$

This page intentionally left blank.

Manuscript approved for publication, May 5, 2008
Prepared by the USGS Publishing Network
Bill Gibbs
Ellen Hardy
Jackie Olson
Bobbie Jo Richey
Linda Rogers
Sharon Wahlstrom
For more information concerning the research in this report, contact the
Director, Oregon Water Science Center
U.S. Geological Survey
2130 SW 5th Avenue
Portland, Oregon 97201
http://oregon.usgs.gov/